WHEEL-SOIL INTERACTION MODELLING FOR ROVER SIMULATION AND ANALYSIS

Ali Azimi

Department of Mechanical Engineering

McGill University, Montréal

December 2013

A Thesis submitted to the Faculty of Graduate Studies and Research in partial fulfilment of the requirements for the degree of Doctor of Philosophy

Abstract

Appropriate modelling of the interaction between wheel and terrain is a key element in simulating wheeled mobile robots and analyzing their functionality on soft terrain. In this thesis, two modelling approaches, with their implementation in a multi-body dynamics environment and their experimental validation, are introduced.

The first approach is based on well-established semi-empirical terramechanics models. The multi-pass effect is considered in the implementation by storing terrain deformation and changes in hardening of soil under the wheel. A high-resolution height-field (HF) is used to model the terrain surface, with relevant information stored in the HF vertices. A novel framework is developed for implementation of this model in a multi-body dynamics environment. For every wheel in contact with soft soil, unilateral contact constraints are added to the solver in the normal direction. Terramechanics forces in the tangent plane and the resistant moment are formulated as set-valued functions associated with kinematic constraints on their complementary variables. The new formulation leads to the dynamics representation in the form of a linear complementarity problem. The properties of these constraints are set based on the soil reactions determined from the semi-empirical terramechanics model, at every time-step of the simulation. With this approach, fast and stable simulation is achieved.

In the second approach, normal and shear stress distributions in the contact area are determined using continuum mechanics with a computationally efficient technique compared

to finite element modelling. The author proposes a velocity field in the vicinity of the contact area motivated by the physical nature of the problem. Using this field, the incremental changes to the stress field are determined by resorting to classical elasto-plasticity theory and an appropriate constitutive relation for soil. As opposed to finite element approaches, which model the soil in contact with the wheel as a high-resolution mesh, our approach focuses on the wheel-soil contact patch only. This localized representation provides the basis for fast wheel-soil interaction modelling. By combining this approach with a height-field as terrain representation, elasto-plastic soil deformation and changes in the hardening state of soil are directly captured. In addition, because of the elasto-plastic representation for soil, energy dissipation during soil compaction is directly captured. The dynamic slip-sinkage behaviour of the wheel and the semi-elliptical shape of the normal stress distribution under the wheel are natural outcomes of the proposed model. The results obtained from the proposed approach are compared with experimental data available in the literature, which show good agreement between the model and experiments under various ranges of wheel slippage and loading conditions.

Moreover, an extensive set of experiments was conducted using a version of the Juno rover (Juno II), owned by the Canadian Space Agency (CSA). The analysis of the results shows good agreement between the experimental rover behaviour and the simulation runs using both models developed.

Résumé

Afin de simuler et d'analyser les mouvements de robots mobiles sur terrain déformable, il est essentiel de correctement modéliser les interactions entre les roues du véhicule et le terrain. Dans cette thèse, deux approches de modélisation seront présentées et analysées, avec leurs mises en œuvre dans un environnement de simulation en temps réel.

La première approche est basée sur un modèle semi-empiriques de mécanique des sols. L'effet du passage répété d'un véhicule sur le terrain est pris en compte par le stockage de la déformation du terrain et du durcissement du sol sous les roues. Un champ de hauteur (Height Field) à haute résolution est utilisé pour modéliser la surface du terrain; les informations nécessaires sont stockées dans les sommets du champ de hauteur. Une approche originale est développée pour la mise en œuvre dans l'engin de simulation. Pour chaque roue en contact avec le sol mou, une contrainte de contact unilatéral est ajouté au solveur pour la direction normal au mouvement. Les forces dans le plan tangent, issus de la mécanique des sols, et la résistance au moment sont traités comme des fonctions multivaluées associées à des contraintes cinématique pour les variables complémentaires. Cette nouvelle formulation conduit à une représentation dynamique sous forme d'un problème de complémentarité linéaire. Les propriétés des contraintes sont définies en fonction des réactions du sol, calculées par le modle semi-empirique à chaque pas de simulation. Avec cette approche, une simulation rapide et stable est obtenue.

RÉSUMÉ

Dans la seconde approche, la répartition des contraintes normales et de cisaillement dans la zone de contact est déterminée en utilisant la mécanique des milieux continus avec une technique de calcul efficace par rapport à la modélisation par éléments finis. Nous proposons l'utilisation d'un champ de vitesses au voisinage de la zone de contact, dans une approche motivée par la nature physique du problème. Avec ce champ de vitesse, les changements progressifs du champ de contraintes sont calculées en recourant à la théorie d'élasto-plasticité classique et à une relation de comportement appropriée pour les sols. Contrairement aux approches par éléments finis, qui modélisent le sol en contact avec la roue comme un maillage haute résolution, notre approche est axée uniquement sur l'aire de contact roue-sol. En combinant cette approche avec un champ de hauteur comme représentation du terrain, la déformation élasto-plastique du sol et les changements dans le durcissement du sol sont directement pris en compte. En outre, en raison de la représentation élasto-plastique du sol, la dissipation d'énergie au cours du compactage du sol est aussi directement prise en compte. Le comportement dynamique de compaction et de glissement de la roue et la forme semi-elliptique de la répartition des contraintes normales sous la roue sont les résultats naturels du modèle proposé. Les résultats obtenus par cet approche sont comparés à des données disponibles dans des études expérimentales, et montre un bon accord avec la théorie pour un large domaine de valeur de glissement et de charge.

En outre, un vaste ensemble d'expériences ont été menées en utilisant une version du rover Juno (Juno II) de l'Agence spatiale canadienne (ASC). L'analyse des résultats montre un bon accord entre le comportement expérimental des rovers et des simulations utilisant les deux modèles développés.

Claims of Originality

- (i) A new framework is developed in the thesis for efficient implementation of semiempirical terramechanics models in a multibody dynamics simulation environment. This approach is based on deregularization of the terramechanics relations by using kinematic constraints with set-valued force characteristics. As a result, efficient and real-time simulation of rovers moving on soft soil is achieved. As opposed to other implementations of these semi-empirical terramechanics models in the literature, which require simplification of these models in order to achieve close to real-time performance, no simplification is required when the implementation of the proposed approach in the multi-body dynamics simulation environment *Vortex* is used. Furthermore, the developed formulation is modular in that various semi-empirical wheel-soil interaction models can be used. The model was partly reported in (Azimi et al., 2010, 2011a).
- (ii) In addition to using semi-empirical models, a novel approach is developed in this thesis for modelling the interaction between wheels and soil. This approach uses elasto-plasticity theory to determine the stress field in the contact area. An important element in our model lies in assuming a plausible velocity field for soil particles, which in turn, eliminates the need of using finite element analysis for determining soil reactions. This novel approach was reported by Azimi et al. (2011c, 2013b).

CLAIMS OF ORIGINALITY

- (iii) In the thesis, the terrain is modelled as rough and deformable. In order to capture an important feature referred to as multipass effect, changes in the hardening properties of soil and the amount of deformation imposed by the wheel are maintained by developing an extended height-field data structure. Both modelling approaches are also implemented in *Vortex*, then used for 3D dynamic simulation of full-scale rovers. This approach is outlined in (Azimi et al., 2012).
- (iv) Experimental investigations were also conducted with the Juno II rover. The experimental outcomes are compared with the results obtained from the developed models, which shows their correctness. The results were presented in (Azimi et al., 2013a).

Acknowledgements

I would like to thank my research supervisors Professor József Kövecses and Professor Jorge Angeles for their guidance during the research and their help during writing the thesis and many other documents.

I would also like to thank Daniel Holz, my colleague at CM-Labs Simulations Inc., for his contributions in technical discussions and for his help in *Vortex* implementation of the models developed in the thesis. I express my gratitude to my other colleagues at CM-Labs: Dr. Guy Prémont for preparing the French abstract; Dr. Marek Teichmann, Michel Carignan, Martin Courchesne, and Robert Weldon for their help in the project and for believing in me.

My friends, Professor Mahdi Taiebat and Professor Shojaa Ramezani, patiently answered all my questions regarding Continuum Mechanics and Elaso-Plasticity Theory. I would like to thank them for their great help.

I would also like to thank Bahareh Ghotbi, Francisco González, and Martin Hirschkorn, my colleagues at McGill University, for their help during the experimental work. I also thank the other people involved in the experiments with the Juno II rover.

I would like to acknowledge the financial support of the Natural Sciences and Engineering Research Council of Canada (NSERC), the Canadian Space Agency (CSA), and the McGill Engineering Doctoral Award program.

ACKNOWLEDGEMENTS

Finally, I would like to express my special gratitude to my wife Hoda, and to my parents for their unconditional love, patience and encouragement.

TABLE OF CONTENTS

TABLE OF CONTENTS

2.5. Summary and Conclusions
CHAPTER 3. An Alternative Model Based on Elasto-Plasticity Theory 59
3.1. Introduction
3.2. Soil Reaction Estimation Using Elasto-Plasticity 60
3.2.1. Computation of the Stress-increment Tensor 6
3.2.2. Determination of the Stress Tensor in the Contact Area 65
3.2.3. Elastic Rebound Computation
3.3. Simulation Results and Further Analysis
3.3.1. Steady-state Motion
3.3.2. Non-steady Motion and Variable Slippage
3.3.3. Analyzing the Slip-sinkage Phenomenon
3.3.4. Discussion on the Proposed Velocity Field and Its Parameter Selection 85
3.4. Validation with Experimental Results
3.5. Integration In the Multi-body System
3.6. Execution Time of the Proposed Algorithms
3.7. Further Discussion and Comparison with Semi-empirical Models 98
CHAPTER 4. Experimental Investigation and Rover Simulation
4.1. Introduction
4.2. Description of the Rover and its Model
4.3. Determining Rover Properties
4.4. Drawbar Pull Experiments on Soft Soil
4.4.1. Comparison with a Semi-empirical Terramechanics Model 110
4.4.2. Comparison with the Elasto-plasticity Model
4.5. Motion on an Irregular Surface
CHAPTER 5. Conclusions and Recommendations for Future Work
5.1. Thesis Contributions
5.2. Recommendations for Future Work
BIBLIOGRAPHY
APPENDIX A. Drucker-Prager Model with Cap Hardening
A.1. Basic Elements of an Elasto-plastic Model
A.2. Elasto-plastic Strain Decomposition and the Elastic Law
A.3. Yield Criterion and Yield Surface
A.4. Plastic Flow Rule and the Hardening Law
APPENDIX B. Computation of the Elastic and Plastic Parts of the Strain-increment
Tensor

1.1	Geometry of rigid wheel and soil contact, with soil reaction forces and moment in dashed red lines
2.1	Schematic of a stationary wheel on a flat horizontal surface and the normal stress distribution developed on the soil (shear stress is not shown). Stress distribution is assumed symmetric, which results in zero drawbar pull. This form of stress distribution occurs when the wheel has only moved downwards with no rotation
2.2	Normal stress distribution under a rigid wheel moving on an uncompacted soil as proposed by (a) the Bekker model, and (b) the WRI model, in which $\lambda=0$ is equivalent to the Wong and Reece (1967a) model 24
2.3	Schematic of wheel and soil contact in the planar case with the equivalent soil reactions. <i>A</i> is the contact point and <i>z</i> is the sinkage, which are obtained by intersecting a line representing the untouched soil surface and the circle, which represents the wheel
2.4	Change of shear stress versus j_d as suggested in Eq. (2.8). τ_{max} , which is equivalent to $c + \sigma(\theta) \tan \phi$, is set to 10 kPa in this figure and K_d is set to 0.025 m
2.5	Shear displacement in the contact area computed from Eq. (1.5) for a wheel with radius and width of 0.15 m and a sinkage of 0.04 m, with soil properties reported in Table 2.1, and assuming zero exit angle. The results are displayed for slip ratios of -0.05 , -0.15 , -0.2 , and -0.3 32
2.6	Shear stress distribution for a wheel with radius and width of 0.15 m and a sinkage of 0.04 m, with soil properties reported in Table 2.1, using the Wong and Reece (1967a) model with zero exit angle. The results are displayed for the slip ratios of -0.05 , -0.15 , -0.2 , and -0.3 , while the computed F_t values are 40.6 N, 5.1 N, -12.5 N, and -41.9 N, respectively
2.7	Forces acting on the soil wedge

2.8	Schematic illustration of determination of bulldozing force via integration over the submerged portion of the wheel sidewall	41
2.9	Illustration of contact points between a rolling cylindrical wheel and a	71
2.9		43
2.10	Schematic of height-field/wheel interaction and the approximating least-	
	squares plane	50
2.11	Schematic of unloading/reloading model of Wong used to find normal	
		52
2.12	Determining the exit angle in the Bekker model from the elastic rebound.	
	p_{max} is the normal stress at point A	55
2.13	Schematic of normal stress distribution under a rigid wheel moving over	
	the track of another wheel, using the Wong and Reece (1967a) and Ishigami	
	et al. (2007) models	56
3.1	The r - θ directions in which the soil-particle velocity is decomposed	63
3.2	Mesh points in a 2D case for a cylindrical wheel. Solid circles are active	
	mesh points	69
3.3	Von Mises stress distribution under the plate in the penetration test with	
	a plate width of 0.1 m	74
3.4	Average pressure developed under the plates vs. plate sinkage using Abaqus	
	Explicit	74
3.5	Comparison of the calculated drawbar pull for 20% slip ratio under the	
	action of different vertical loads	76
3.6	Comparison of the calculated resistance force for 20% slip ratio under the	
	action of different vertical loads	76
3.7	Comparison of the resulting sinkage for 20% slip ratio under the action	
	of different vertical loads	77
3.8	Normal stress distribution for 20% slip ratio under $F_z = 165 \text{ N} \dots \dots$	77
3.9	Shear stress distribution for 20% slip ratio under $F_z = 165 \text{ N} \dots \dots$	78
3.10	Normal and shear stress distributions for 20% slip ratio under $F_z = 165 \text{ N}$	
	using Algorithm 1 with consideration of elastic rebound of soil	79
3.11	Command forward and angular velocities to the wheel	80
3.12	Vertical position of wheel centre versus time as predicted by our novel	
	approach in modelling wheel-soil interaction	81
3.13	Wheel traction and rolling resistance as predicted by our novel approach	
	in modelling wheel-soil interaction	81
3.14	Vertical position of wheel centre vs. time as predicted by the modified	
	Bekker and WR models (Azimi et al., 2011a)	82

3.15	and WR models explained in Chapter 2	. 8	32
3.16	Wheel traction and rolling resistance as predicted by the proposed model with different mesh points on the wheel. (a) 180 mesh points; and (b) 360		
	mesh points	. 8	3
3.17	Normal stress under a rigid wheel versus local sinkage ζ (see Fig. 1.1 for a definition of ζ) at various slip ratios under $F_z = 165$ N, while the elastic rebound is considered	0	0.4
3.18	Normal and shear stress distributions for various slip ratios under $F_z =$. 0	34
5.10	165 N using Algorithm 1, where the elastic rebound is considered	. 8	35
3.19	Trajectories of a soil particle when a wide rigid wheel with a diameter of 0.3 m moves over it at various slip ratios, as predicted by the proposed velocity field. Wheel and soil properties are the same as those used in this section: (a) Soil particle is initially at the soil surface; and (b) soil particle is initially 10 mm below the soil surface	. 8	37
3.20	Schematic of assumed and actual velocity vectors of soil particle near the beginning of contact when the entry angle (θ_1) is relatively large	. 8	88
3.21	Velocity field of soil particles under a rigid wheel moving with 30% slip ratio: (a) the horizontal; and (b) the vertical velocity components. The unit of color bars is m/s (Courtesy of Karl Iagnemma from MIT)	. 8	39
3.22	Colour plots of the proposed velocity field for soil particles under a rigid wheel moving with 30% slip ratio: (a) the horizontal; and (b) the vertical velocity components. The unit of color bars is m/s	. 9	00
3.23	Vertical position of wheel centre vs. time under an 80-N vertical load on the wheel centre and different slip ratios, as predicted by our model	. 9)1
3.24	Variation of wheel sinkage vs. slip ratio under an 80-N vertical load on the wheel centre		2
3.25	Variation of developed drawbar pull vs. slip ratio under an 80-N vertical load on the wheel centre		
3.26	Variation of applied torque on the wheel vs. slip ratio under 80-N vertical load on the wheel centre)3
3.27	Comparison of wheel sinkage computed from the plasticity model with experimental data reported in Fig. 18 of Ding et al. (2011a), under a 35-N, 80-N, and 150-N vertical load acting on the wheel centre. A rigid wheel with 10-mm grousers was used in the experiments.		
3.28	Comparison of the drawbar pull computed from the plasticity model with experimental data reported in Fig. 18 of Ding et al. (2011a), under a 35-N,	0	14
	80-N, and 150-N vertical load on the wheel centre	. 9	4

3.29	Comparison of the driving torque computed from the plasticity model with experimental data reported in Fig. 18 of Ding et al. (2011a), under a 35-N, 80-N, and 150-N vertical load acting on the wheel centre 95
3.30	Plane-strain FE simulation of a rigid cylinder on a soil with Abaqus/Explicit.
3.30	The cylinder moves with 20% slip ratio
3.31	Sojourner rover simulation in Vortex using the elasto-plasticity model. The rover moves on a height-field and the soil deformation and the hard-
3.32	ening parameter are stored in the height-field vertices
3.33	Normal and shear stress distributions obtained from the elasto-plasticity model when the wheel is moving with 10% slip. The result correspond to $t = 6.495$ s and $v_z = 0$
4.1	Pictures of the Juno rover, captured during experiments
4.2	Juno II rover
4.3	Images from the simulation of Juno rover in <i>Vortex</i>
4.4	Simulated Juno rover in <i>Vortex</i> at different tilting configurations
4.5	Illustration of the rover model with its joints. Totally, eight revolute joints, three universal joints, three spherical joints, and one prismatic joint
	are used in the multibody model of the rover
4.6	Juno II on the configurable metallic incline
4.7	Measured current of both motors (left and right sides) versus average speed of the motors for the rover moving on horizontal flat concrete floor.
	The error-bars show the variation in the measured current
4.8	Average motors speed versus the duty cycle for the rover moving on horizontal flat concrete floor
4.9	Comparing the motor torques obtained from the simulation and the torque determined from experiments using current measurements with the deter-
	mined K_{mt} of 0.251: (a) left motor; (b) right motor
4.10	The descender and the load cell used in the drawbar pull tests
4.11	The rover attached to the load cell after a drawbar pull test
4.12	Schematic illustration of the drawbar pull experiments
4.13	Measured tension in the rope over time. Sampling frequency of the load
	cell was 3 Hz

4.14	Measured motor current over time during the drawbar pull test. Sampling frequency was 20 Hz	.114
4.15	Measured motor speed over time during the drawbar pull test. Sampling	
1.10	frequency was 20 Hz.	.115
4.16	Measured rover position over time during the drawbar pull test. Sampling	
	frequency of the total station was 2 Hz	. 115
4.17	The drawbar pull versus slip ratio for different values of K_d	.117
4.18	Comparing the drawbar pull obtained from experiments with the values obtained from simulation using the approach of Chapter 2 and the WRI	
	model	.118
4.19	Comparing the driving torque of the left side motor obtained from experiments with the values obtained from simulation using the approach of	
	Chapter 2 and the WRI model	.119
4.20	Comparing the driving torque of the right side motor obtained from ex-	
	periments with the values obtained from simulation using the approach	
	of Chapter 2 and the WRI model	.119
4.21	The rover with the added mass to its main frame	. 120
4.22	Comparing the drawbar pull obtained from experiments with the values	
	obtained from simulation using the the approach of Chapter 2 and the	
	WRI model. The rover was heavier, as shown in Fig. 4.21	. 121
4.23	Comparing the driving torque of the left side motor obtained from ex-	
	periments with the values obtained from simulation using the approach	
	of Chapter 2 and the WRI model. The rover was heavier, as shown in	
	Fig. 4.21	. 121
4.24	Comparing the driving torque of the right side motor obtained from ex-	
	periments with the values obtained from simulation using the approach	
	of Chapter 2 and the WRI model. The rover was heavier, as shown in	
	Fig. 4.21	
4.25		
	obtained from simulation using the elasto-plasticity model	. 123
4.26	Comparing the driving torque of the left side motor obtained from experi-	
	ments with the values obtained from simulation using the elasto-plasticity	
	model	. 124
4.27	Comparing the driving torque of the right side motor obtained from ex-	
	periments with the values obtained from simulation using the elasto-	
	plasticity model	. 124
4.28	Comparing the drawbar pull obtained from experiments with the values	
	obtained from simulation using the elasto-plasticity model. The rover	
	was heavier, as shown in Fig. 4.21	. 125

4.29	Comparing the driving torque of the left side motor obtained from experiments with the values obtained from simulation using the elasto-plasticity model. The rover was heavier, as shown in Fig. 4.21	126
4.30	Comparing the driving torque of the right side motor obtained from experiments with the values obtained from simulation using the elastoplasticity model. The rover was heavier, as shown in Fig. 4.21	
4.31	LIDAR scan of the test area	128
4.32	Location of the rover on the terrain before starting the experiment	128
4.33	The height-field terrain prepared using the LIDAR scan data, with the initial location of the rover	129
4.34	The angular velocity of the left motor obtained from the experiment and the filtered value used in the simulation	130
4.35	The angular velocity of the right motor obtained from the experiment and the filtered value used in the simulation	130
4.36	The global position of the reflector, attached to the rover. The experimental results are compared with the values obtained from simulation using the semi-empirical model	131
4.37	The energy expenditure of the left side motor. The experimental results are compared with the values obtained from simulation using the semi-empirical model	132
4.38	The energy expenditure of the right side motor. The experimental results are compared with the values obtained from simulation using the semi-empirical model	
4.39	The driving torque of the left side motor. The experimental results are compared with the values obtained from simulation using the semi-empirical model	
4.40	The driving torque of the right side motor. The experimental results are compared with the values obtained from simulation using the semi-empirical model	122
4.41	The global position of the reflector, attached to the rover. The experimental results are compared with the values obtained from simulation using the elasto-plasticity model.	
4.42	The energy expenditure of the left side motor. The experimental results are compared with the values obtained from simulation using the elasto-	
4.43	plasticity model	
	plusticity intouci	150

4.44	The driving torque of the left side motor. The experimental results are compared with the values obtained from simulation using the elastoplasticity model	37
4.45	The driving torque of the right side motor. The experimental results are compared with the values obtained from simulation using the elastoplasticity model	
A.1	Mathematical model for the uniaxial tension experiment (adapted with	5 1
	modification from (de Souza Neto et al., 2008))	
A.2	Yield surface in the p - q plane (adapted from (SIMULIA, 2010)) 15	56
A.3	A typical hardening relation between $\varepsilon_{\text{vol}}^p$ and p_b (adopted with modifica-	
	tion from (SIMULIA, 2010))	59
A.4	Evolution of the yield surface in the p - q plane with changes in p_b . Increasing p_b results in expansion in the yield surface, and hence, hardening, while reduction in p_b leads to a smaller yield surface and soil	
	softening	59

LIST OF TABLES

2.1	Parameters of the semi-empirical model, taken from Ishigami et al. (2007)		
3.1	Material properties for the elasto-plastic constitutive relation		
3.2	The hardening pattern used in the elasto-plastic constitutive relation 73		
3.3	Parameters of the Bekker and WR models used for comparison 73		
3.4	Parameters of the proposed velocity field		
3.5	Parameters of the proposed velocity field used in the experimental validation 91		
4.1	Parameters of the WRI model with multipass used in simulation runs with		
	Juno II rover		
4.2	Material properties for the elasto-plastic constitutive relation		
4.3	Parameters of the proposed velocity field used in the elasto-plasticity		
	model		

CHAPTER 1

Introduction

1.1 Motivation

Mobile robotic systems represent key elements for planetary exploration as well as earthly applications. Such robots have to operate on various different types of unstructured terrain, among which soft deformable soil is of particular interest. In order to investigate the effect of deformable soil on the performance of rovers, appropriate models are required to represent the interaction between wheel and terrain. In this context, soil reactions are required in response to the wheel movement. In these models, high fidelity could be needed, while the computational efficiency is a key element in the application of the models.

1.2 Scope and Objectives of the Thesis

Depending on the application, different modelling techniques can be used for studying wheel and soil interaction. The scope of this thesis is to develop wheel-soil interaction models for simulation and analysis of rovers in a multi-body simulation environment, which can be used, for example, in the design, control, or operation planning of rovers. For this purpose, parametric models with modest computational cost are of interest. For earthly-based applications, however, an entirely empirical technique can also be used, with

a look-up table. As empirical techniques cannot be extrapolated beyond the conditions for which they were developed, they are not discussed in this thesis.

A semi-empirical technique that allows for the parametric analysis of wheel-soil interaction was proposed by Bekker (1956). This model and its extension proposed by Wong and Reece (1967a) are widely used, as they have been experimentally validated and are computationally efficient. The latter is referred to as the Wong-Reece (WR) model in this thesis. These two models have a broad range of application in characterizing vehicles on soft terrain. Both models have significant applications in mobile robotics as well. For example, in the AESCO Soft Soil Tyre Model (AS2TM) (AESCO, 2005), the Bekker model is used. Furthermore, Iagnemma (2001), Iagnemma and Dubowsky (2004), Shibly et al. (2005), Ishigami et al. (2007, 2009), Hutangkabodee et al. (2008), and Senatore and Sandu (2011) used the WR model in their wheel-soil interaction studies. In addition, Wong and Asnani (2008) compared the performance of several wheels of lunar vehicles by means of the NWVPM software package (Wong, 2010), in which normal stress distribution under the wheel is obtained using the Bekker model. A simplified version of the WR model was used by Iagnemma et al. (2004) to identify cohesion and internal friction angle of soil for real-time applications of rovers operating on soft soil. Terrain parameter identification was also done by Ray (2009), using the WR model. This WR model was also used by Ojeda et al. (2006) for wheel-slip detection and positioning error compensation.

A framework is developed in Chapter 2 for the implementation of these semi-empirical models in a multi-body dynamics simulation environment. In this thesis, the implementations are based on *Vortex*¹, an advanced multi-body dynamics simulation environment developed by CM-Labs Simulations Inc. As discussed in Chapter 2, the framework can be used to accommodate various types of terramechanics models.

¹http://www.vxsim.com/

In addition to semi-empirical models, other models, based on continuum mechanics, can be employed. In this regard, soft soil is modelled as a continuum, in which wheelsoil contact can be analyzed by considering an appropriate constitutive relation for soil and using detailed finite element discretization to calculate stress distribution and soil deformation in the contact area, as reported in (Chiroux et al., 2005; Fervers, 2004; Xia, 2011). In yet another class of methods, dry soil is modelled as cohesionless granular material, with wheel-soil contact analyzed with the discrete element method (DEM) (Wong, 2010). One of the issues with DEM in wheel-soil interaction modelling is the need to consider a large number of particles, which results in an extremely high computing time, even with supercomputers (Wong, 2010). For wheel-soil interaction, Finite Element Analysis (FEA) is computationally less demanding than DEM. However, FEA is still inappropriate for a multibody dynamics simulation environment, because of its high computational cost.

An efficient novel approach, based on elasto-plasticity theory, is introduced in Chapter 3 of this thesis for wheel-soil interaction. This approach will be shown to extend the application domain of the above-mentioned semi-empirical models, while being compatible with dynamics formulations and multibody simulation environments. In this context, instead of resorting to FEA to find soil reactions on the rigid wheel, an assumed velocity field in the contact region is used. A rather simple, still plausible velocity field is assumed that can lead to acceptable results, comparable to those obtained with the Bekker and WR models and experimental data.

1.3 Literature Review and Background Material

1.3.1 Traditional Semi-empirical Models in the Longitudinal Direction

In order to predict motion resistance of a rigid wheel on soil, Bekker (1956, 1969) assumed that the normal stress distribution under the wheel can be obtained from the average pressure under a flat plate when pushed into the soil. Bekker surmised that the relation between this average pressure and plate sinkage can be represented for homogeneous terrain

as

$$p = \left(\frac{k_c}{b} + k_\phi\right) z^n \tag{1.1}$$

where p is pressure, b the plate width used in the penetration test, k_c the pressure-sinkage parameter due to the cohesive effects, k_{ϕ} the pressure-sinkage parameter due to the frictional effects, z the sinkage of the flat plate, and $n \in \mathbb{R}^+$ is an exponent of deformation (Wong, 2008). It is noteworthy that k_{ϕ} and k_c have dimensions dependent on the value of n, which is a shortcoming of the model.

What is known as the *bevameter* (Bekker, 1969; Wong, 2008) is one of the best-known techniques for measuring the terrain response to loading relevant to vehicle-mobility studies. It can be employed to find the pressure-sinkage relationship using a set of plate-penetration tests, as well as performing a set of shear tests to derive the shear stress-displacement relationship. In the penetration test, a plate of suitable size is used to emulate the contact area of the wheel. As mentioned by Wong (2008), the parameters k_c , k_{ϕ} , and n can also be obtained using circular plates in the penetration test.

The shear stress-displacement relationship, obtained from the shear tests, can be expressed as indicated below for most of the homogeneous soils (Wong, 2008):

$$\tau = (c + p \tan \phi)[1 - \exp(-j_d/K_d)]$$
 (1.2)

where τ is the shear stress, j_d is the shear displacement, with units of length, c and ϕ are the cohesion stress and the angle of internal friction of the terrain, respectively, and K_d is referred to as the *shear deformation modulus*, with units of length. Equation (1.2), proposed by Janosi and Hanamoto (1961), is a simplified form of a relation suggested by Bekker (1956).

In order to predict the soil reaction on a rigid wheel, Bekker (1956) assumed that the radial terrain reaction at all points on the contact surface is equal to that under a plate penetrated to the same depth. Therefore, the normal stress distribution under a rigid wheel

on homogeneous terrain can be obtained from Eq. (1.1) as (Bekker, 1956; Wong, 2008):

$$\sigma_n(\theta) = \left(\frac{k_c}{b} + k_\phi\right) \zeta^n(\theta) \tag{1.3}$$

where b is either the wheel width or the smaller dimension of the wheel/terrain contact patch (Wong, 2010), ζ is the vertical sinkage at any point on the contact surface, as illustrated in Fig. 1.1, and angle θ describes the location of any point in the contact patch, as shown in the same figure.

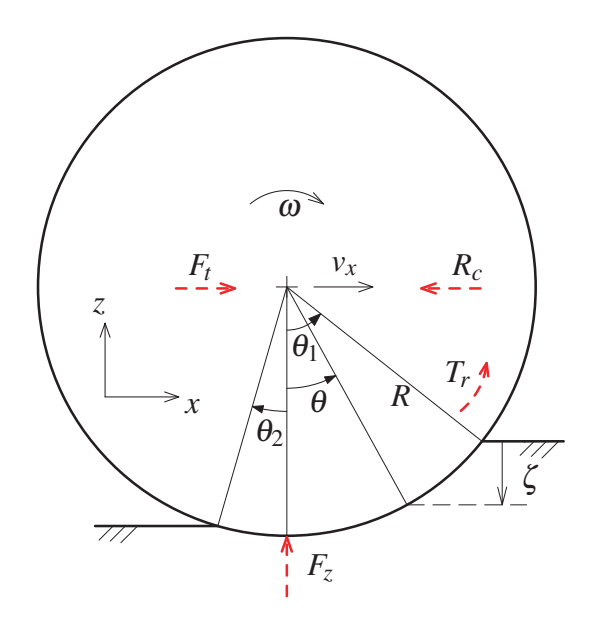


FIGURE 1.1. Geometry of rigid wheel and soil contact, with soil reaction forces and moment in dashed red lines.

By knowing the normal stress distribution σ_n in the contact area, the shear stress distribution τ is expressed using Eq. (1.2) as

$$\tau(\theta) = (c + \sigma_n(\theta) \tan \phi) \left[1 - \exp\left(-\frac{j_d(\theta)}{K_d}\right) \right]$$
 (1.4)

Different relations for the shear displacement j_d have been proposed in the literature. The relation proposed by Wong and Reece (1967a) for a driven wheel has been the most widely adopted:

$$j_d(\theta) = R[(\theta_1 - \theta) - (1 - i_s)(\sin \theta_1 - \sin \theta)] \tag{1.5}$$

CHAPTER 1. INTRODUCTION

where θ is defined in Fig. 1.1, θ_1 is an angle indicating the initial contact with soil, R is the wheel radius, and i_s is the wheel slip ratio, defined as

$$i_s = \frac{R\omega - v_x}{R\omega} \tag{1.6}$$

where ω is the angular velocity of the wheel and v_x is the horizontal component of the velocity of the wheel centre, for a wheel in planar motion. It should be mentioned that Eq. (1.5) is obtained by integrating the slip velocity in the contact region from the initial point of contact with soil, identified by the angle θ_1 , to the current angle θ and assuming a constant slip ratio (Wong and Reece, 1967a).

When the normal and shear stress distributions around the wheel are known, the soil reactions, including motion resistance R_c , traction force F_t , resisting moment T_r , and terrain vertical reaction force F_z can be obtained as

$$R_c = Rb \int_{\theta_2}^{\theta_1} \sigma_n(\theta) \sin \theta \, d\theta \tag{1.7}$$

$$F_t = Rb \int_{\theta_2}^{\theta_1} \tau(\theta) \cos \theta \, d\theta \tag{1.8}$$

$$T_r = R^2 b \int_{\theta_2}^{\theta_1} \tau(\theta) d\theta \tag{1.9}$$

$$F_z = Rb \int_{\theta_2}^{\theta_1} [\tau(\theta)\sin\theta + \sigma_n(\theta)\cos\theta] d\theta$$
 (1.10)

and $F_t - R_c$ is what is known as the *drawbar pull* of the wheel.

By neglecting the effect of shear stress on F_z and assuming small wheel sinkage, Bekker (1956, 1969) estimated motion resistance R_c as

$$R_c = \frac{(3F_z)^{\nu_1}}{(3-n)^{\nu_1}(n+1)(k_c+bk_\phi)^{\nu_2}(2R)^{\nu_3}}$$
(1.11)

where $v_1 = (2n+2)/(2n+1)$, $v_2 = 1/(2n+1)$, and $v_3 = (n+1)/(2n+1)$. In addition, the wheel sinkage can be estimated as (Bekker, 1956, 1969)

$$z = \left(\frac{3F_z}{(3-n)(k_c + bk_{\phi})\sqrt{2R}}\right)^{2v_2}$$
 (1.12)

REMARK 1. It should be noted that, some quantities with dimensions are raised to powers in Eqs. (1.11) and (1.12), because Eq. (1.1) was used to develop them.

Onafeko and Reece (1967) mentioned that the pressure-sinkage relationship expressed in Eq. (1.1) is unsatisfactory, since the dimension of soil parameters k_c and k_{ϕ} are dependent on n. This brings about further problems in relations developed based on Eq. (1.1), for example Eqs. (1.11) and (1.12). Therefore, the pressure-sinkage relation, Eq. (1.1), should be replaced by

$$p = (k_1 + k_2 b) \left(\frac{z}{h}\right)^n \tag{1.13}$$

As mentioned by Onafeko and Reece (1967), Eq. (1.13) may take the form below for very compact soils:

$$p = (k_c'c + k_\phi'\gamma_s b) \left(\frac{z}{b}\right)^n \tag{1.14}$$

where k'_c , k'_ϕ , and n are new dimensionless pressure-sinkage parameters, and γ_s is the specific weight of the terrain. Furthermore, Onafeko and Reece (1967) indicated that K_d in Eq. (1.2) is usually dependent on both the contact pressure and plate width used in the bevameter test. The dependency of K_d on contact pressure is also mentioned by Wong (2008).

Wong (1967) studied the soil behaviour beneath rigid wheels for compact, dry sand and for frictionless clay. Wong observed that a rigid wheel displaces the compact soil partly laterally and partly longitudinally. In addition, he mentioned that there are usually two flow zones in the longitudinal plane, one forward, one backward.

CHAPTER 1. INTRODUCTION

Wong and Reece (1967a) referred to some experimental studies on sand in which they showed that the radial stress distribution is slip-dependent, and the maximum radial stress does not occur at the bottom-dead-centre, as would be expected from the plate sinkage analogy. They proposed the empirical relation given below for estimating angle θ_M as the location of the point of the maximum radial stress in the contact patch:

$$\theta_M = (c_1 + c_2 i_s)\theta_1 \tag{1.15}$$

where c_1 and c_2 are dimensionless constants. Wong and Reece (1967a) proposed the relations below for normal stress distribution:

$$\sigma_{n}(\theta) = \begin{cases} (k_{1} + k_{2}b) \left(\frac{R}{b}\right)^{n} \left[\cos \theta - \cos \theta_{1}\right]^{n}, & \theta_{M} \leq \theta < \theta_{1} \\ (k_{1} + k_{2}b) \left(\frac{R}{b}\right)^{n} \left[\cos \left(\theta_{1} - \frac{\theta - \theta_{2}}{\theta_{M} - \theta_{2}}(\theta_{1} - \theta_{M})\right) - \cos \theta_{1}\right]^{n}, & \theta_{2} \leq \theta < \theta_{M} \end{cases}$$

$$(1.16)$$

where θ_2 represents the exit angle, illustrated in Fig. 1.1. In addition, shear stress distribution was obtained using Eq. (1.2), in which the shear displacement j_d is determined from Eq. (1.5). Soil reactions can then be obtained from Eqs. (1.7)–(1.10), by assuming $\theta_2 = 0$. It should be noted that non-zero values for θ_2 have been used in the literature, as discussed in Subsection 1.3.2.

REMARK 2. It should be mentioned that the three forms of pressure-sinkage relations, Eqs. (1.1), (1.13), and (1.14), are frequently used in the literature to obtain the normal stress under a wheel. For that, either the model of Bekker, expressed in Eq. (1.3), or the model of Wong and Reece (1967a), given in Eq. (1.16), is used.

Wong and Reece (1967b) also studied the behaviour of towed rigid wheels on sand. Similar to their approach for analyzing driven rigid wheels (Wong and Reece, 1967a), where the authors estimated the position of maximum normal stress, Wong and Reece (1967b) first estimated the position of what they called a transition point. This is the point

on the wheel periphery at which shear stress changes direction. This point lies at the junction of two soil failure zones beneath a towed wheel, as concluded from experiments (Wong and Reece, 1967b). Since at this point shear stress is zero, the normal stress becomes a principal stress at the transition point on a towed rigid wheel; it is the major principal stress. By assuming that (*i*) soil failure only occurs in the direction of wheel motion, and (*ii*) soil is incompressible, the transition point can be determined using the relation (Wong and Reece, 1967b)

$$\tan\left(\frac{\pi}{4} - \frac{\phi}{2}\right) = \frac{\cos\theta_t - 1/(1 - i_s)}{\sin\theta_t} \tag{1.17}$$

where θ_t is the angle representing the position of the transition point. Equation (1.17) may result in two solutions for θ_t in the acceptable range of $\theta_t \in [0, \theta_1)$; however, as discussed by Wong and Reece (1967b), the transition point always takes the smaller value.

Furthermore, the maximum radial stress would be expected to act at the transition point, as suggested by classical soil mechanics (Wong and Reece, 1967b). In addition, the position of maximum radial stress was observed to be very close to the transition point in the experiments (Wong and Reece, 1967b). The normal stress distribution for towed wheels is then calculated similar to driven wheels, and can be expressed using Eq. (1.16) upon using θ_t for θ_M as

$$\sigma_{n}(\theta) = \begin{cases} (k_{1} + k_{2}b) \left(\frac{R}{b}\right)^{n} \left[\cos \theta - \cos \theta_{1}\right]^{n}, & \theta_{t} \leq \theta < \theta_{1} \\ (k_{1} + k_{2}b) \left(\frac{R}{b}\right)^{n} \left[\cos \left(\theta_{1} - \frac{\theta - \theta_{2}}{\theta_{t} - \theta_{2}}(\theta_{1} - \theta_{t})\right) - \cos \theta_{1}\right]^{n}, & \theta_{2} \leq \theta < \theta_{t} \end{cases}$$

$$(1.18)$$

Shear stress distribution is also obtained using Eq. (1.4), while the shear deformation j_d in the front region, $\theta \in [\theta_t, \theta_1]$, should be determined by (Wong and Reece, 1967b)

$$j_d = R \left[(\theta_1 - \theta) \frac{(1 - i_s)(\sin \theta_1 - \sin \theta_t)}{\theta_1 - \theta_t} - (1 - i_s)(\sin \theta_1 - \sin \theta) \right]$$
(1.19)

In addition, in the rear region, $\theta \in [\theta_2, \theta_t]$, j_d is obtained from Eq. (1.5).

CHAPTER 1. INTRODUCTION

As an alternative to the Wong and Reece (1967b) approach, Gee-Clough (1976) also studied free-rolling, towed, rigid wheels. In this approach, instead of local sinkage $\zeta(\theta)$, the cumulative normal displacement $N(\theta)$, with units of length, was used to find the radial (normal) stress

$$\sigma_n(\theta) = \left(\frac{k_c}{b} + k_\phi\right) [N(\theta)]^n \tag{1.20}$$

where $N(\theta)$ can be calculated as (Gee-Clough, 1976)

$$N(\theta) = R(1 - i_s)(\cos \theta - \cos \theta_1) \tag{1.21}$$

Substituting Eq. (1.21) in Eq. (1.20) leads to

$$\sigma_n(\theta) = \left(\frac{k_c}{b} + k_\phi\right) \zeta^n(\theta) (1 - i_s)^n \tag{1.22}$$

By comparing Eq. (1.22) with Eq. (1.3), the difference between the Bekker and the Gee-Clough (1976) approaches lies in the term $(1-i_s)^n$. Furthermore, the latter is proposed for towed wheels, only.

1.3.2 Recent Developments Pertinent to Rover Simulation

Some of the recent improvements on semi-empirical Bekker models related to rover simulation are discussed below. It should be noted that the research work associated with using these models in a multi-body dynamics environment and dealing with rough terrain is discussed in Subsection 1.3.3.

• Effect of Grousers:

The effect of grousers has been investigated with various methods. A simple and common approach, as in (Jia et al., 2012), consists in using a larger wheel radius—the original radius plus the grouser height. Another approach, however, is to consider individual bulldozing forces on the grousers (Trease et al., 2011). In the thesis, grousers

are not explicitly included; a larger-wheel-radius approach can be used to approximate their effect.

• Computation of the exit angle θ_2 :

In the Bekker model, as mentioned above, the exit angle is assumed zero. However, a non-zero exit angle can be determined by considering ground flexibility and obtaining soil rebound, as reported in (AESCO, 2005). This is discussed in more detail in Section 2.4.5. In addition, Ishigami et al. (2007) used the Wong and Reece (1967a) model with a non-zero exit angle. In their approach, the non-zero exit angle is assumed by means of a *visually* identified parameter, which relates the exit angle θ_2 to the entrance angle θ_1 .

• Slip-sinkage behaviour:

Ding et al. (2010a) conducted a set of experiments on a *lunar soil simulant* to study the slip-sinkage behaviour and the extra sinkage caused by grousers. They used the Ishigami et al. (2007) model as a base-line and suggested that the exponent in the pressure sinkage relation should be a linear function of the slip-ratio. With this modification, a good match between theory and experimental slip-sinkage was reported. However, no theoretical analysis was provided. The dynamic slip-sinkage is captured in our novel elasto-plastic model, introduced in Chapter 3, in a different way, without any particular assumption, as discussed in more detail in Subsection 3.3.3.

• Small and Lightweight Rovers:

Meirion-Griffith (2012) extended the pressure-sinkage relation of Bekker to include wheel diameter with application to lightweight rovers with small wheels. In that approach, rigid cylinders are used in the pressure-sinkage experiments, instead of flat plates. As a result, the pressure-sinkage relation is dependent on the wheel diameter. Soil behaviour can be modelled using critical state soil mechanics, in which the overall density of the soil mass dominates the behaviour of soil under shear deformation (Wood, 1990). Basically, under a constant normal stress, for dense soil, the shear

stress increases with the shear strain and then decreases, and may reach a constant value; whereas, in soft soil, the shear stress does not show this behaviour. This aspect of soil behaviour has been discussed by Senatore and Iagnemma (2011) and its importance has been explained especially for lightweight mobile robots. They also proposed a relation on considering the density effect on the shear response. However, as mentioned by Senatore and Iagnemma (2011), this relation requires further investigation. It should be noted that the framework proposed in Chapter 2 for the implementation of the semi-empirical terramechanics models can accommodate this relation for obtaining the shear stress distribution.

1.3.3 Review of Semi-empirical Models in Multi-body Environments

The wheel-soil interaction model AS^2TM (AESCO, 2005) was used by Bauer et al. (2005, 2008) with the SimMechanics toolbox of Matlab. The experimental validation of AS^2TM was reported by Bauer et al. (2005), while the application of the tool developed in assisting the design and optimization of rover mobility systems is discussed in (Bauer et al., 2005) and (Bauer et al., 2008).

AS²TM is a wheel-soil interaction model that is developed based on the work of Schmid (1995). This model is available as a Matlab/Simulink S-Function, and uses the basic concepts introduced by Bekker. The pressure-sinkage relation follows the Bekker model, and the shear stress is developed using the Janosi-Hanamoto relation. Certain features like tire flexibility and grousers effect are incorporated in this model according to AESCO (2005).

Ishigami et al. (2007) extended the semi-empirical model of Wong and Reece (1967a) and investigated the effect of lateral forces introduced during the steering manoeuvres of rovers. This terramechanics model was used with a multibody model of an articulated four-wheel rover to simulate the motion of the rover on soft soil. In this work, soil reactions are added as external forces to the wheels, and the rover is assumed to move on a flat

surface. This work was extended by Ding et al. (2010b) for operation on rough terrain, in which the interaction area between the wheel and the rough terrain is simplified as a plane. The terramechanics model was also extended by including the slip-sinkage model of Ding et al. (2010a). However, the terrain reactions on the wheel are again included as external forces and moments on each wheel. In addition, in order to speed up the simulation, the terramechanics relations are simplified. In Chapter 2 of this thesis, an approach is developed to avoid direct application of terrain reactions as external forces and moments. The disadvantages of using external forces/moments are discussed in Chapter 2.

In the work reported by Schäfer et al. (2010), the multibody simulation package Simpack is used for the simulation of rovers. In their work, the soft soil surface is represented by a height-field. In order to find soil reactions, the penetration depth of a wheel into each contacting node of the terrain surface is determined. At each contacting node, the pressure is obtained from the Bekker relation, Eq. (1.1), while the shear stress is determined from a basic Mohr-Coulomb friction model. In their approach, the displaced soil is distributed around the moving wheel. There is, however, no discussion about computational efficiency of their approach. Furthermore, this approach is not modular, in the sense that using other terramechanics relations, e.g., the Wong and Reece (1967a) model or the model of Ishigami et al. (2007), is not trivial. Our approach, however, enables faster than real-time simulation of rovers, with the ability to use a variety of semi-empirical terramechanics models.

Trease et al. (2011) used MSC-Adams for developing a multibody dynamics simulation platform, which uses terramechanics relations regarding wheel-soil interaction, and is used for the simulation of the Spirit and Opportunity rovers. They used the semi-empirical model of Ishigami et al. (2007) with a different lateral force model and incorporated the slip-sinkage model of Ding et al. (2010a).

A volumetric contact model for the interaction of wheel and soil was developed by Petersen (2012). Using the Bekker pressure-sinkage relation and the geometry of the contact, the model implicitly considers the energy dissipation during motion, coming from the rolling resistance, while being computationally efficient. This model is used with the MapleSim simulation toolbox to develop simulation of the Juno rover. Even though the Bekker pressure-sinkage relation is used in the development of this model, the semi-empirical terramechanics models are not explicitly included in the model. Therefore, the extension of the model to include the Wong and Reece (1967a) model or the slip-sinkage model of Ding et al. (2010a), requires further research.

1.3.4 Other Pertinent Approaches

An alternative to semi-empirical models is to use continuum mechanics-based models. In this family of models, the soil is represented with elastic, visco-elastic, elasto-plastic, or elastic-visco plastic constitutive relations. In order to determine the stress field and soil deformation, spatial discretization techniques such as finite element method (FEM) are frequently used.

Early attempts in the use of finite element analysis (FEA) for studying wheel-soil interaction have been reported by Perumpral et al. (1971), Yong and Fattah (1976), and Yong et al. (1978). By the advances made in FEA and the computational capacity of computers, this approach was pursued by others. Liu and Wong (1996) and Liu et al. (2000) modelled elasto-plastic soil response by the use of critical state soil mechanics. Other examples in using FEA for interaction analysis between wheel or tire and soil can be found in the work reported by Schmid (1995), Fervers (2004), Chiroux et al. (2005), Hambleton and Drescher (2008, 2009), and Xia (2011).

As an alternative approach, Karafiath (1971) and Karafiath and Nowatzki (1978) assumed that the soil under a moving wheel is in the state of failure. Using this assumption, they surmised that the failure in the soil mass can be represented by the simple Mohr-Coulomb failure criterion, in which the strength of soil is defined by the internal friction angle and the cohesion of soil. By neglecting the inertial effects, the slip lines of failure were determined, which then led to the stress field. This approach, however, requires

the soil to be modelled as a rigid-plastic material (Yong and Fattah, 1976), and cannot be extended for other plastic soil representations.

In addition, Wanjii et al. (1997) represented the soil under a rigid wheel with a viscoelastic three-element Maxwell model to determine normal stress distribution in the contact area. Using the assumptions of Bekker, normal stress is determined from pure vertical deformation of soil under the wheel; normal stress is assumed independent of the shear stress. The shear stress is then determined using the Janosi and Hanamoto (1961) relation. This approach differs from the Bekker model in that the normal stress is determined by means of a visco-elastic model, whereas in the Bekker model, the normal stress is independent of velocity. This approach, however, does not capture plastic soil deformation and the slip-sinkage phenomenon.

In the approach developed in Chapter 3 (Azimi et al., 2013b, 2011c), a high-fidelity elasto-plastic representation is used for the soil mass, in which plastic soil deformation and soil hardening/softening are captured. In addition, by assuming a plausible velocity-field in the contact area, the stress field is determined without resorting to FEA.

1.4 Thesis Outline

Implementation of semi-empirical terramechanics models in a multibody dynamics environment is the focus of Chapter 2. In this chapter, the scope of semi-empirical models and their limitations when used with dynamic multibody systems are explained first. The implementation details and the developed framework are then discussed. A key concept in this part relates to the *deregularization* of the terramechanics models, which in turn leads to wheel-soil interaction models in the form of linear complementarity problems (LCPs). Soil compaction and hardening, which results in the multi-pass effect, are also included in the model.

A novel approach based on elasto-plasticity theory is developed in Chapter 3 for analyzing the interaction between a rigid wheel and soft soil. The developed model is explained

CHAPTER 1. INTRODUCTION

step-by-step through various algorithms included in Chapter 3. Simulation results obtained from the new technique are compared against semi-empirical terramechanics models as well as available experimental data. Additional illustrative examples are also provided to show the behaviour of the new model in a dynamic operation with variable slippage. Furthermore, discussion on the dynamic slip-sinkage effect, which is captured in the new approach, is included.

In Chapter 4, the wheel-soil interaction models developed in the thesis are used for 3D simulation of the *Juno II* rover using *Vortex*. In addition, experimental results obtained based on an extensive set of tests are compared with the results of the simulation. The Juno II rover was developed by Neptec and Ontario Drive Gear (ODG) for the Canadian Space Agency (Visscher and Reid, 2012).

Chapter 5 summarizes the contributions of the work and includes suggestions for future research work.

CHAPTER 2

Semi-empirical Models in a Multi-body Dynamics Environment

2.1 Introduction

In this chapter, the implementation of semi-empirical models in a multibody dynamics environment is discussed. It should be mentioned that the scope of this chapter is not to develop new terramechanics models, but to develop and explain a framework for efficient implementation of these models. Here, the most widely used semi-empirical terramechanics models are explained and used. As explained in detail in this chapter, these models are revised to make them compatible with multi-body dynamics environments.

The thesis focuses mainly on the wheel motion in the longitudinal direction. The forces acting in the lateral direction, however, are also included and discussed later in this chapter. The lateral direction is added so that the motion of rovers on uneven terrain and during steering manoeuvres can also be simulated and analyzed.

As explained below, all the semi-empirical models for the longitudinal direction, which are discussed in this thesis, are originated from the analogy made by Bekker in relating the normal stress under the wheel to the average pressure under a flat plate penetrating

soil. Therefore, these models are referred to as the family of Bekker models, or the semiempirical Bekker models, in this thesis.

In Section 2.2, CM-Labs' *Vortex*¹, the multibody software package employed, is briefly described. A review of pertinent semi-empirical models for the longitudinal direction was included in Section 1.3.1. The scope and limitations of these models when used with multibody systems is discussed in Section 2.3. The detailed implementation of semi-empirical models is explained in Section 2.4. In this section, operations on flat terrain are first discussed, followed by an extension of the model to motion on rough deformable terrain with multipass effect in Section 2.4.5.

In the semi-empirical Bekker models, the soil reactions can be obtained from Eqs. (1.7)—(1.10), when wheel sinkage and slip ratio are known, which are readily obtained from wheel position and velocity. These reactions can directly be added to the wheel as external forces and moments. However, there are some issues with this approach. To explain these issues, the assumptions made in the semi-empirical Bekker models are reviewed, followed by their limitations when used in the context of multibody dynamic systems.

Part of the work discussed in this chapter was published in (Azimi et al., 2010, 2011a, 2012).

2.2 Brief Description of Vortex

Vortex is a simulation environment for complex multibody systems. It includes advanced graphical capabilities and is optimized for fast, real-time simulation. The basic elements of a multibody model are *rigid bodies* and *constraints*, the former being referred to as *parts* in Vortex. Several different types of constraints are available in Vortex, in order to impose kinematic restrictions between parts. The kinematic constraints apply restrictions on the relative position or velocity of the bodies by applying internal forces/moments. Vortex can limit the maximum possible internal forces/moments that can be applied by the

¹http://www.vxsim.com/

kinematic constraint. When the required internal force/moment of the constraint goes beyond the maximum limit or capacity of the kinematic constraint, the constraint will not be able to maintain the kinematic restriction.

In Vortex, the parts can contain what is known as *collision geometries*. Collision geometries can be simple shapes, such as cubes, cylinders, and spheres, as well as more complicated ones, such as height-fields and polyhedra. Contacts are detected between any pair of bodies with defined collision geometries; if the latter overlap, the overlapping volume is reduced to a contact patch and normal direction. This patch is then further reduced to several contact points at the extremities of the patch. A unilateral constraint is then created at each contact point.

Moreover, Vortex can model viscous or dry friction using what is called the *box model*, where the friction bounds along the axes that span the contact plane are explicitly specified. Alternatively, the maximum force may be defined as a function of the normal force. Vortex uses a linear complementarity problem (LCP) solver for the forward dynamics problem.

2.3 Scope and Limitations of Semi-empirical Bekker Models in Connection with Multibody Systems

The semi-empirical Bekker models, reviewed in Section 1.3.1, were developed under certain assumptions, where a *cylindrical* wheel is assumed to move on a *flat* and *horizontal* soil surface under *steady-state* conditions. In this context, given the vertical load on the wheel centre and the slip ratio, these models make it possible to determine the wheel sinkage, drawbar pull, and driving torque. Some of the shortcomings and limitations of these models, resulting from the above assumptions, are listed below.

L1: If the semi-empirical Bekker models are directly used for dynamics simulation, the vertical component of the wheel-centre velocity v_z does not contribute to the calculated soil reaction. Therefore, the soil reaction force in the *z*-direction (F_z)

is only a function of sinkage *z* and slip ratio, which, in turn, means that the energy loss due to dynamic motion in the *z*-direction cannot be accounted for with these semi-empirical models. Simulation of a wheel/terrain interaction directly with the Bekker or WR model results in an artificial oscillatory response in the vertical direction. A remedy to this problem is to add a nonlinear damping term, as discussed in this chapter. It should be mentioned that the model proposed in Chapter 3, based on elasto-plasticity theory, addresses this limitation by capturing the energy loss due to the plastic deformation of the terrain.

L2: The other issue comes from the use of the slip ratio. Consider the simulation of a single wheel driven by a torque. When the wheel is stopped on a horizontal flat terrain, and no torque is applied, the forces in the forward wheel direction, which are F_t and R_c according to Fig. 1.1, must balance. When the wheel is stopped, the slip ratio is undefined, according to Eq. (1.6). Depending on soil properties and wheel sinkage, there exists a slip ratio at which F_t and R_c balance, if the wheel sinkage is not too high. However, finding this slip ratio requires an iterative approach, if any of the semi-empirical models mentioned earlier are used. Here, one can use another model for a stopped wheel on flat, horizontal terrain that develops zero drawbar pull, for example, a model with symmetric stress distribution, as shown in Fig. 2.1. However, when the wheel or rover is on a slightly inclined surface, this model cannot work, as the normal and shear stress distributions will not be symmetric. In addition, directly using these semiempirical models requires finding a slip ratio (different from the slip ratio in the case of a horizontal surface) that results in the above-mentioned force balance. In the case of a rover that is stopped on irregular terrain, the above-mentioned approaches are not feasible for finding the slip ratios for all wheels that would result in the force balance. Furthermore, when the wheel moves very slowly, abrupt changes in the slip ratio can happen that could cause spurious oscillations

and even instability if the time-step of the simulation is not small enough. It is noted that when the wheel centre velocity and angular velocity are small, the slip ratio is close to an undefined state.

A framework is developed in this chapter for efficient implementation of semiempirical models, which handles these issues by introducing several constraints and applying soil reactions via these constraints, instead of considering them as directly applied forces/moments. This framework accommodates different semiempirical models and handles any wheel motion.

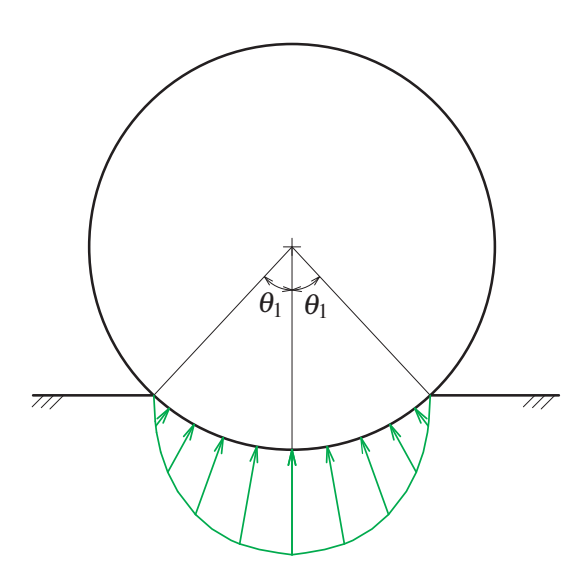


FIGURE 2.1. Schematic of a stationary wheel on a flat horizontal surface and the normal stress distribution developed on the soil (shear stress is not shown). Stress distribution is assumed symmetric, which results in zero drawbar pull. This form of stress distribution occurs when the wheel has only moved downwards with no rotation.

Considering these limitations, semi-empirical models have to be modified before being used in multibody dynamics simulation environments, as discussed in the remainder of this chapter. In addition, a framework is developed to *deregularize* the interaction model by means of kinematic constraints.

2.4 Implementation of Semi-empirical Models

In order to employ semi-empirical relations in a multibody dynamics environment like *Vortex*, it is necessary to determine soil reactions (forces and moments) based on the wheel pose (position and orientation) and twist (velocity and angular velocity) in addition to the dimensions of the wheel and soil parameters.

The overall procedure involved in the method is first discussed in Section 2.4.1, in which, by referring to the limitations mentioned in Section 2.3, the motivation of the approach developed in this chapter is explained. Then, the planar motion is discussed, followed by non-planar motion. Extensions for operation on rough deformable soil is then explained.

2.4.1 Motivation and Overall Procedure

As discussed in Section 1.3.1, using semi-empirical Bekker models, soil reactions can be readily determined from Eqs. (1.7)–(1.10), when wheel sinkage and slip ratio are known. A typical approach in the literature, as mentioned in Section 1.3.3, is to apply these reactions as external forces and moments to the wheel.

Now we recall the limitation L2 mentioned in Section 2.3 in the use of the slip ratio. As discussed therein, the problem is that when the rover is stopped, or it is close to stopping, the slip ratio is undefined according to Eq. (1.6). However, in order to determine soil reactions from Eqs. (1.7)–(1.10), the slip ratio has to be known a priori. Assuming an arbitrary slip ratio is also not possible, as it will lead to reaction forces/moments that will not result in force balance. Therefore, the reaction forces cannot be determined from the same semi-empirical formulation.

Furthermore, when the rover is moving very slowly, the slip ratio can vary substantially from one simulation step to the next one. This means that small changes in the rover

velocity can lead to large changes in the reaction forces, i.e., the system involves steep characteristics for the forces that involve the slip ratio. This, in turn, means that the differential equations resulting for such a system will be *stiff*.

As an alternative in dealing with systems with steep force laws, Pfeiffer (2007), replaced those force laws, in a hydraulic system, with their equivalent set-valued force representation. This led to a dynamics representation for the hydraulic system where the explicit, force representations based on constitutive equations are replaced by unilateral and bilateral constraints on the kinematic variables complementary to the forces. This approach can be referred to as *deregularization*. In the approach proposed in this thesis, the dynamic system is deregularized by introducing kinematic constraints with set-valued force laws, and avoiding direct use of terramechanics relations that would produce external applied forces/moments. As will be shown in Section 2.4.4, the system with these constraints will lead to a linear complementarity problem (LCP), which can be solved, in turn, in an efficient way using LCP solvers.

When modelling the terrain reactions to the wheel via external forces and moments, numerical problems can happen with large time-steps. Small time-steps must, therefore, be used, which can lead to unacceptably large simulation times. With non-smooth modelling, which results from deregularization, relatively large time steps may be used with great accuracy and stability. This can lead to high simulation efficiency.

Furthermore, as the terramechanics forces/moments are not directly applied as external forces/moments in the proposed approach, we can assume a particular slip ratio for the cases when the wheel is stopped. Therefore, the same terramechanics relations can be used for both a moving and a non-moving wheel, which makes the proposed framework appropriate for the implementation of various semi-empirical terramechanics models.

2.4.2 Planar Wheel Motion

Based on the form of the stress distribution under the wheel, the semi-empirical models

discussed in this thesis are divided into two. In the first model, referred to as the Bekker model, the normal stress distribution is obtained from Bekker's assumption, in which the location of the maximum normal stress is at the bottom of the wheel (Bekker, 1969). In the second model, referred to as the WRI model, for Wong, Reece, and Ishigami, the location of the maximum normal stress is shifted forward according to Wong and Reece (1967a), and a nonzero exit angle can be considered based on the model of Ishigami et al. (2007), as shown in Fig. 2.2. The following relation is used to determine the exit angle in the WRI model:

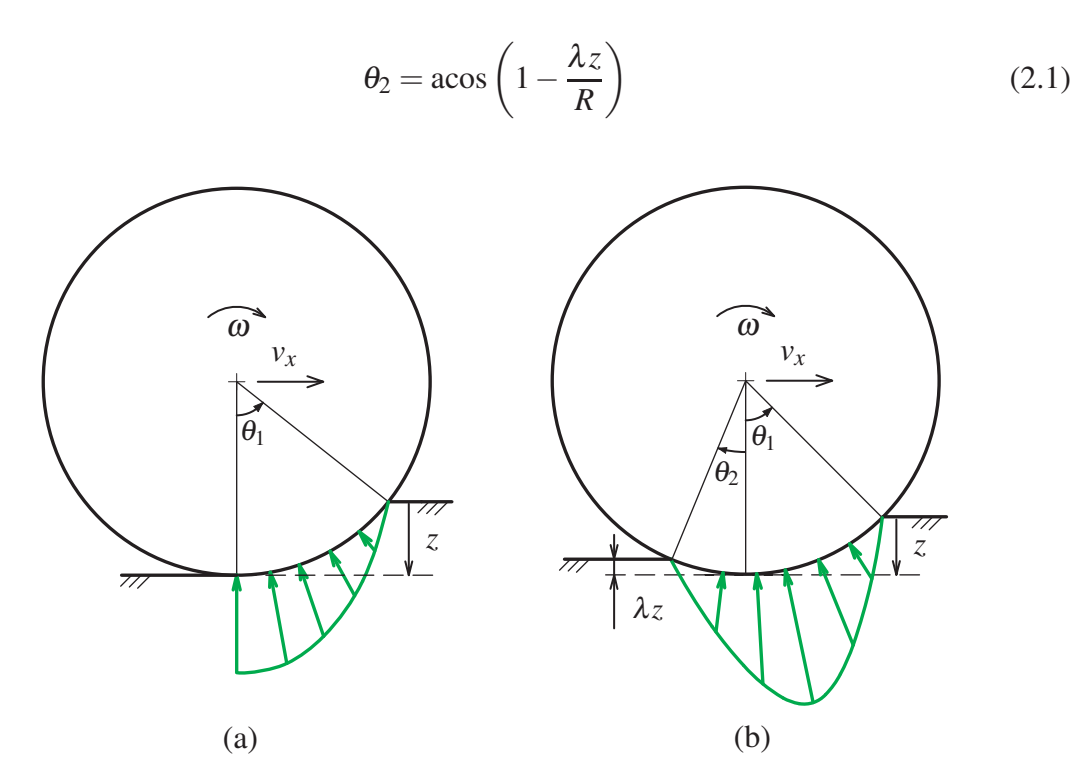


FIGURE 2.2. Normal stress distribution under a rigid wheel moving on an uncompacted soil as proposed by (a) the Bekker model, and (b) the WRI model, in which $\lambda = 0$ is equivalent to the Wong and Reece (1967a) model.

In addition, the shear stress distribution is obtained from Eqs. (1.4) and (1.5) in both models. Slight modifications to these relations, however, are required to obtain the shear stress in a multibody dynamics environment, as explained in Section 2.4.2.2.

2.4.2.1 Normal Direction

The force in the normal direction is introduced by means of a viscoelastic-like response, wherein we change stiffness and damping coefficients every time-step of the simulation, based on terramechanics relations. In this regard, it is noted that if the wheel sinkage is positive, the reaction force F_z occurs, while for negative sinkages, i.e., no contact between wheel and terrain, the reaction force vanishes. Therefore, the force in the normal direction can be modelled with a one-point contact with unilateral properties, in the planar case. In this case, by intersecting a circle, which represents the cylindrical wheel, and a line, which represents a plane, the sinkage value and the contact point A, as shown in Fig. 2.3, can be readily obtained².

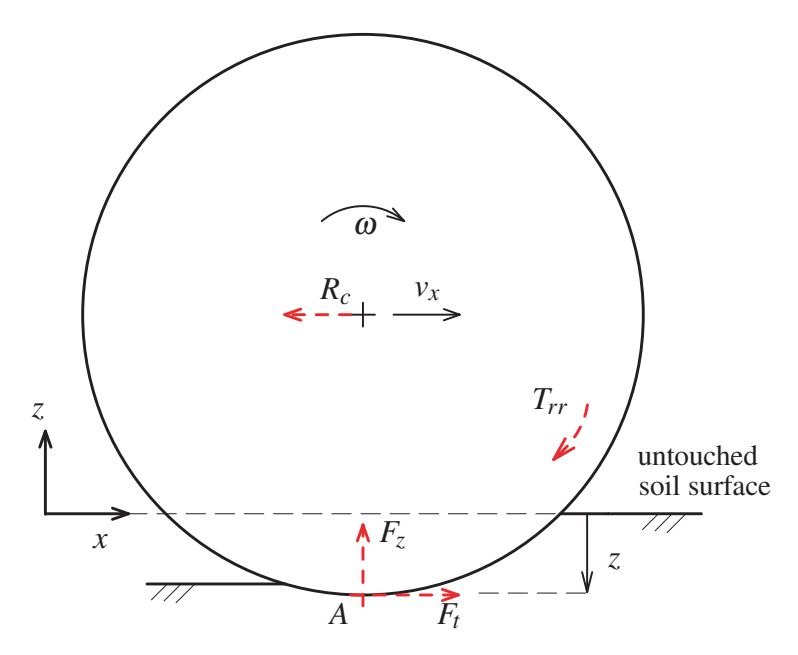


FIGURE 2.3. Schematic of wheel and soil contact in the planar case with the equivalent soil reactions. A is the contact point and z is the sinkage, which are obtained by intersecting a line representing the untouched soil surface and the circle, which represents the wheel.

The normal reaction force predicted by any of the semi-empirical models mentioned above, Eq. (1.10), is a function of wheel sinkage and slip ratio. As the semi-empirical

²It should be mentioned that *Vortex* provides the possibility of changing the stiffness and damping coefficients of any contact point at every simulation step.

CHAPTER 2. SEMI-EMPIRICAL MODELS IN A MULTI-BODY DYNAMICS ENVIRONMENT

formulae were not developed for dynamic conditions, the energy dissipation during the motion in the vertical direction is not captured. Therefore, if this relation is directly used in a multibody dynamics environment, undamped oscillations occur. To avoid this unrealistic behaviour, a damping term is added, as discussed below. It is noted that under steady-state conditions, i.e., zero relative vertical velocity between wheel and terrain, the damping term vanishes and the terrain reactions resulting from this implementation are equivalent to the ones obtained from the semi-empirical models.

The instantaneous stiffness coefficient k_z is defined based on the semi-empirical models as

$$k_z = \frac{Rb}{z} \int_{\theta_2}^{\theta_1} [\tau(\theta) \sin \theta + \sigma_n(\theta) \cos \theta] d\theta$$
 (2.2)

where z is the wheel sinkage. It should be noted that k_z is a nonlinear function of sinkage and slip ratio. At every time step, k_z changes according to the current values of sinkage and slip ratio, so the resulting force applied to the wheel will be equivalent to the reaction force given by the original semi-empirical models, i.e., Eq. (1.10). By including the damping term, the normal reaction force becomes

$$F_z = Rb \int_{\theta_2}^{\theta_1} \left[\tau(\theta) \sin \theta + \sigma_n(\theta) \cos \theta \right] d\theta + c_z \dot{z}$$
 (2.3)

where c_z is a damping coefficient and \dot{z} represents the velocity component of the wheel normal to the contact plane. Choosing an appropriate damping coefficient is not straightforward. Here, the damping coefficient is defined to be proportional to the stiffness coefficient as

$$c_z = \eta_c k_z \tag{2.4}$$

where η_c is the proportionality coefficient and has units of frequency. It was found empirically that if η_c lies between 0.1 and 0.4 s⁻¹, this added damping can lead to realistic

responses with zero or negligible oscillation. In the simulation runs included in this thesis, $\eta_c = 0.1~{\rm s}^{-1}$ is used. It should be noted that the criterion in selecting the proper damping coefficient lies in obtaining a simulated response with zero or negligible oscillation in the normal direction.

A viscoelastic system is also used by Sohl and Jain (2005) in the ROAMS planetary rover simulation package, regarding the wheel-terrain contact modelling in the direction normal to the terrain. They used a single-DOF Hunt-Crossley (Hunt and Crossley, 1975) model, in order to determine normal terrain reaction force on the wheels. However, as the instantaneous stiffness coefficient obtained from the semi-empirical model, i.e. Eq. (2.2), is different from the one obtained from the above-mentioned Hunt-Crossley model, wheel sinkage and the computed normal force differ from those expected by the equivalent semiempirical model. As mentioned by Sohl and Jain (2005), the normal force obtained from the viscoelastic model can then be used to determine the *corrected sinkage* and the other reactions of the terrain, using the semi-empirical model. This means that the semi-empirical model is not used in their approach in determining the normal force on the wheel and the simulated wheel penetration to the ground. In addition, no discussion regarding the rolling resistance was presented. However, in the approach proposed in this thesis, the viscoelastic model is determined based on the *instantaneous* stiffness of the terrain, which results in the sinkage and the normal force calculation matching the semi-empirical model employed. Moreover, as discussed later, other soil reactions determined from a semi-empirical model, including rolling resistance, are included in our formulation.

2.4.2.2 *Slip Ratio*

In this thesis, it is assumed henceforth that the same model is used for driving, braking, and towed conditions, as also assumed by Ishigami et al. (2007). In this regard, following the approach explained in the foregoing reference, the model proposed by Wong and Reece

CHAPTER 2. SEMI-EMPIRICAL MODELS IN A MULTI-BODY DYNAMICS ENVIRONMENT

(1967a) is also used for a braking or towed wheel upon redefining the slip ratio and the computation of shear stress, as discussed below.

REMARK 3. For a towed rigid wheel, a model was proposed by Wong and Reece (1967b) slightly different from their model for a driven wheel (Wong and Reece, 1967a). However, the two models show a discontinuity when switching between them, as is required when modelling general, dynamic rover operations including non-steady states. Therefore, the model for a driven wheel (Wong and Reece, 1967a) was used by Ishigami et al. (2007) for the entire range of operation. The same approach as in (Ishigami et al., 2007) is used in this thesis as well.

The slip ratio defined in Eq. (1.6) is only valid for a driving wheel (i.e., $|R\omega| \ge |v_x|$). It is redefined below to support the driving, braking, and towed cases:

$$i_{s} := \begin{cases} 1 - \frac{v_{x}}{R\omega} & \text{if } |v_{x}| \leq |R\omega| \neq 0 \text{ (driving)} \\ \frac{R\omega}{v_{x}} - 1 & \text{if } |R\omega| < |v_{x}| \neq 0 \text{ (braking or towed)} \end{cases}$$
 (2.5)

For a wheel moving very slowly, a small variation in v_x or ω can cause a large change in the slip ratio. Therefore, the value of slip ratio determined from Eq. (2.5) is modified as shown below. To this end, an intermediate variable is defined as

$$v_{\text{temp}} = \begin{cases} R\omega & \text{, if } |v_x| \le |R\omega| \\ v_x & \text{, otherwise} \end{cases}$$
 (2.6)

The slip ratio is then redefined as

$$i_{s} := \begin{cases} 0 & \text{, if } v_{\text{temp}} = 0\\ \frac{R\omega - v_{x}}{v_{\text{temp}}} \left[1 - \exp\left(-\frac{v_{\text{temp}}^{2}}{v_{\text{min}}^{2}}\right) \right] & \text{, otherwise} \end{cases}$$
(2.7)

where v_{min} is an indication of an insignificant speed for the rover. For example, when analyzing or simulating a rover with a nominal speed of 0.1 m/s, v_{min} of around 0.0001 m/s could be employed.

This modified definition for slip ratio leads to the same results as in Eq. (2.5) when the wheel is not moving very slowly. In addition, in the case of a stationary wheel, a slip ratio of zero is assumed³. Furthermore, when the wheel moves very slowly, the slip ratio remains close to zero, according to Eq. (2.7). This avoids fluctuations in the slip ratio for a slow-moving wheel. It should be mentioned that the assumed zero slip ratio for a stationary wheel, is a natural choice, as for a slowly-moving wheel the slip ratio determined from Eq. (2.5) can fluctuate around zero, which, in turn, means that the filtered value for slip ratio under this condition should be close to zero. The assumption of using zero slip ratio for a stationary wheel provides a smooth transition in the slip ratio when the wheel starts or stops moving, thus leading to numerical stability.

In addition, the shear stress distribution is obtained from the relation below, instead of Eq. (1.4), to properly account for the effect of a negative slip ratio:

$$\tau(\theta) = (c + \sigma(\theta) \tan \phi) \left[1 - \exp\left(-\frac{|j_d(\theta)|}{K_d}\right) \right] \operatorname{sgn}(j_d), \tag{2.8}$$

where j_d is expressed in Eq. (1.5) and $sgn(\cdot)$ is the signum function, defined as

$$\operatorname{sgn}(x) = \begin{cases} 1 & \text{if } x \ge 0 \\ -1 & \text{if } x < 0 \end{cases}$$
 (2.9)

It is noted that K_d is a positive scalar; therefore, directly using a negative j_d in Eq. (2.8) without taking its absolute value, makes no physical sense. According to Janosi and Hanamoto (1961), the shear stress $\tau(\theta)$ changes from zero to its maximum of $c + \sigma(\theta) \tan \phi$ by the use of an exponentially decaying function of a positive j_d . When j_d is negative,

³As mentioned in Section 2.4.1, our proposed approach makes it possible to use a particular slip ratio for a stationary wheel.

 $\tau(\theta)$ also becomes negative, while the form of the exponentially decaying function does not change. An illustration of the modified $\tau(\theta)$ of Eq. (2.8) is shown in Fig. 2.4.

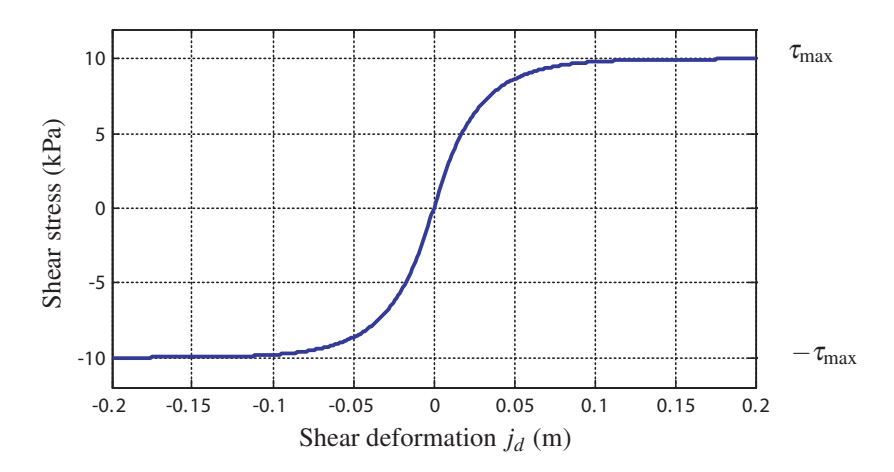


FIGURE 2.4. Change of shear stress versus j_d as suggested in Eq. (2.8). τ_{max} , which is equivalent to $c + \sigma(\theta) \tan \phi$, is set to 10 kPa in this figure and K_d is set to 0.025 m.

2.4.2.3 Traction and Resistance

As seen in Fig. 1.1, there are four reactions determined from Eqs. (1.7)–(1.10). F_z is considered by setting compliance and damping coefficients at the contact point in a one-point contact model, as mentioned above. R_c in Eq. (1.7) is related to $\sigma_n(\theta)$, while F_t and T_r are functions of the shear stress distribution. Instead of directly applying these forces/moments to the wheel, as mentioned in Section 2.4.1, appropriate constraints are formulated, which are consistent with the point-contact model employed. The traction force F_t is first discussed, followed by T_r and R_c .

Let us recall the ideal case of contact between a wheel and a plane, in the context of rigid-body dynamics. In this case, a standard modelling approach is to consider a unilateral constraint to represent the contact in the normal direction. In addition, in the presence of dry friction, the Coulomb friction model is often used for the tangential contact plane, with the velocity of the contact point as a key variable.

The traction force and resisting moment, determined from terramechanics, are included using the point contact model and the relative velocity of the contacting bodies at the contact points, as explained below.

The traction force F_t is obtained from the shear stress distribution; it is included in the model using the position and velocity of the contact point, as displayed in Fig. 2.3. Using the longitudinal velocity component of the contact point A of the wheel, referred to as v_{Ax} , the revised set-valued model for the traction force and its complementary variable, v_{Ax} , will be given. The revised model is explained in two steps. The first revised model for the traction force, referred to as F_{td} , can be given as

$$F_{td}(v_{Ax}) = \begin{cases} -|F_t| & \text{if } v_{Ax} > 0\\ [-|F_t|, |F_t|] & \text{if } v_{Ax} = 0\\ |F_t| & \text{if } v_{Ax} < 0 \end{cases}$$
 (2.10)

In other words, when $v_{Ax} \neq 0$, F_{td} acts in the opposite direction of v_{Ax} , and its value is clearly defined, while F_{td} can take any value between $|F_t|$ and $-|F_t|$ if v_{Ax} is zero.

A key concept in this formulation is that F_{td} is expressed as a set-valued force law in terms of its complementary kinematic variable v_{Ax} . Therefore, F_{td} , expressed in Eq. (2.10), can be interpreted by introducing a *kinematic constraint* on the contact velocity v_{Ax} , and assuming that the *maximum constraining force* that can be provided by this constraint is *limited*. For Eq. (2.10), the kinematic constraint is $v_{Ax} = 0$, with the maximum restraining force limit of $|F_t|$.

Let us now assume that the WR model is used and the wheel moves to the right, which is the assumed positive direction of motion. When the slip ratio is positive, which means $v_{Ax} < 0$, the shear displacement $j_d(\theta)$ will be non-negative according to Eq. (1.5). This, in turn, means that the shear stress $\tau(\theta)$ will be non-negative in the contact area as well, under Eq. (1.4). Therefore, the traction force F_t will be positive, according to Eq. (1.8). This is consistent with Eq. (2.10).

However, when $v_{Ax} > 0$, which means a negative slip ratio, the shear displacement in the contact area $j_d(\theta)$ can become positive, negative, or zero depending on the value of slip ratio and wheel sinkage, according to Eq. (1.5). Figure 2.5 illustrates this behaviour for a wheel moving to the right with a relatively high sinkage.

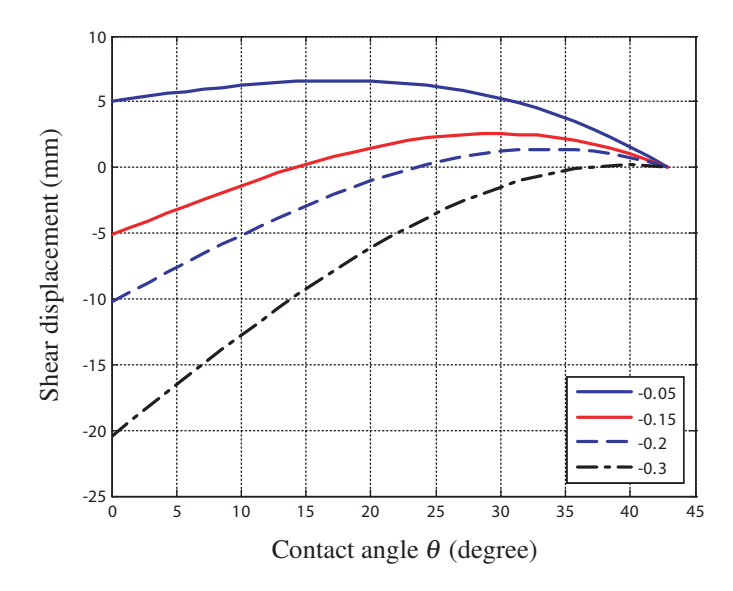


FIGURE 2.5. Shear displacement in the contact area computed from Eq. (1.5) for a wheel with radius and width of 0.15 m and a sinkage of 0.04 m, with soil properties reported in Table 2.1, and assuming zero exit angle. The results are displayed for slip ratios of -0.05, -0.15, -0.2, and -0.3.

Therefore, the shear stress can show a similar behaviour using Eq. (1.4). The shear stress in this case can vary as shown in Fig. 2.6, for example. This means that the traction force F_t , when the wheel has a negative slip ratio, can be positive, negative, or zero. This is not consistent with Eq. (2.10). For example, as mentioned in the caption of Fig. 2.6, the traction force F_t determined from Eq. (1.8) is positive for slip ratios -0.05 and -0.15, while F_{td} , determined based on Eq. (2.10), is negative, because the contact velocity v_{Ax} is positive (as $i_s < 0$). For slip ratios of -0.2 and -0.3, however, F_{td} , determined based on Eq. (2.10), is negative, as is the value of F_t .

The undesired change of the direction of F_{td} occurs due to using the reference contact velocity of zero in the formulation. This behaviour, however, can be corrected by revising

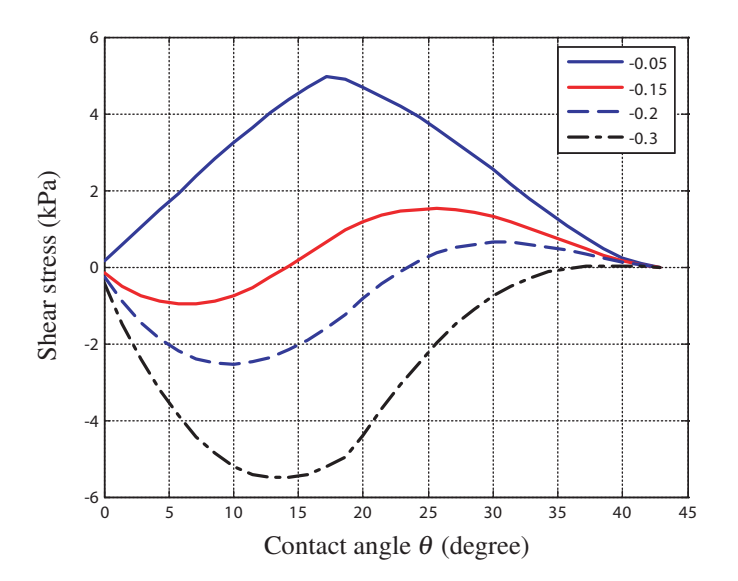


FIGURE 2.6. Shear stress distribution for a wheel with radius and width of 0.15 m and a sinkage of 0.04 m, with soil properties reported in Table 2.1, using the Wong and Reece (1967a) model with zero exit angle. The results are displayed for the slip ratios of -0.05, -0.15, -0.2, and -0.3, while the computed F_t values are 40.6 N, 5.1 N, -12.5 N, and -41.9 N, respectively.

TABLE 2.1. Parameters of the semi-empirical model, taken from Ishigami et al. (2007)

ϕ (deg)	37.2
c (Pa)	800
$k_{\phi} (N/m^{(n+2)})$	8.14×10^{5}
$k_c \left(N/m^{(n+1)} \right)$	1.37×10^{3}
n (-)	1.0
K_d (m)	0.025
<i>c</i> ₁ (-)	0.4
c ₂ (-)	0.15

 $F_{td}(v_{Ax})$ as:

$$F_{td}(v_{Ax}) = \begin{cases} -|F_t| & \text{if } v_{Ax} > v_{ref} \\ [-|F_t|, |F_t|] & \text{if } v_{Ax} = v_{ref} \\ |F_t| & \text{if } v_{Ax} < v_{ref} \end{cases}$$
(2.11)

where v_{ref} is non-zero when the slip ratio is negative and the F_t determined from Eq. (1.8) becomes positive; v_{ref} can be defined as

$$v_{ref} = \begin{cases} (1+c_3)v_{Ax} & \text{, if } i_s < 0 \& F_t > 0\\ 0 & \text{, otherwise} \end{cases}$$
 (2.12)

where c_3 is any small non-dimensional positive scalar. With the revised formulation, the kinematic constraint equation is $v_{Ax} = v_{ref}$, with the maximum restraining force of $|F_t|$. It should be mentioned that in every time-step of the simulation, the value of F_t is determined from terramechanics relations, e.g. Eq. (1.8), by means of the sinkage and slip ratio determined in the last time-step. In addition, v_{ref} is determined using the last time-step value of v_{Ax} . Therefore, before performing a new simulation step, the values of F_t and v_{ref} are determined from the results of the last time-step. With these values, the appropriate constraint that represents Eq. (2.11) is set up. As will be shown in Section 2.4.4, the dynamic equations of the multibody system with this constraint can lead to a linear complementarity problem.

By inspection, one can realize that Eqs. (2.11) and (2.12) are consistent with the expected behaviour from terramechanics relations. Different cases of planar wheel motion are discussed below. It is noted that F_t is the value directly determined from the terramechanics relations and it does not take into account the direction of motion of the wheel centre. Positive F_t helps the wheel to move, while negative F_t opposes the wheel motion.

- Case 1: Wheel moves to the right $(v_x > 0)$ with $i_s > 0$: In this case, positive i_s results in $F_t > 0$, and both conditions $v_x > 0$ and $i_s > 0$ lead to $v_{Ax} < 0$; therefore, from Eq. (2.12) $v_{ref} = 0$ and in turn $v_{Ax} < v_{ref}$. From Eq. (2.11), F_{td} becomes $|F_t|$, as expected.
- Case 2: $v_x > 0$ with $i_s < 0$, which implies that $v_{Ax} > 0$. In this case, if $F_t > 0$, v_{ref} becomes $(1 + c_3)v_{Ax}$ from Eq. (2.12), and hence, $v_{Ax} < v_{ref}$. Therefore, F_{td} becomes $|F_t|$, as expected.

In addition, if $F_t < 0$, v_{ref} becomes zero from Eq. (2.12), then $v_{Ax} > v_{ref}$, which results in $F_{td} = -|F_t|$. This is also the expected result.

Case 3: $v_x < 0$ with $i_s > 0$, which implies that $v_{Ax} > 0$. In this case, $F_t > 0$ and, as explained above, F_t should help the wheel to move in its current direction of motion, which is to the left. Therefore, it is expected to see a negative F_{td} .

From Eq. (2.12), $v_{ref} = 0$. As $v_{Ax} > v_{ref}$, F_{td} becomes $-|F_t|$, which is the expected result, too.

Case 4: $v_x < 0$ with $i_s < 0$, which implies that $v_{Ax} < 0$. In this case, if $F_t > 0$, v_{ref} becomes $(1+c_3)v_{Ax}$ from Eq. (2.12), and thus $v_{Ax} > v_{ref}$. Therefore, $F_{td} = -|F_t|$ is the outcome of Eq. (2.11), which again is the expected result. In addition, if $F_t < 0$, v_{ref} becomes zero from Eq. (2.12), and therefore, $v_{Ax} < v_{ref}$, which results in $F_{td} = |F_t|$. This is also the expected result.

As explained further in Section 2.4.4, Eq. (2.11) can lead to the formulation of a linear complementarity problem (LCP). This formulation, enables fast and stable simulation of rovers moving on soil, while wheel-soil contact is represented with semi-empirical terramechanics models. It should be noted that multibody systems with unilateral contact can generally be formulated as LCP, as mentioned by Anitescu and Potra (1997), who formulated a multibody system with unilateral contact and dry friction as a LCP. *Vortex*, the multibody dynamics simulation environment used in our implementation, is generally based on such formulations and it employs efficient LCP solvers.

The soil reactions displayed in Figs. 1.1 and 2.3 must be equivalent. The soil reactions shown in Fig. 1.1 are F_t , R_c , F_z , and T_r , with all the reaction forces acting through the wheel centre. The equivalent system of soil reactions shown in Fig. 2.3 is composed of F_t , F_t , and F_t , where F_t is referred to as the *residual resistance torque*. It should be noted that in this equivalent system, F_t acts at the contact point F_t , not at the wheel centre. For the two systems to be equivalent, F_t must be related to F_t by

$$T_{rr} = RF_t - T_r \tag{2.13}$$

Similar to the approach explained above for the traction force, the revised formula for the residual resistance torque can be given as

$$T_{rrd}(v_{Ax}) = \begin{cases} -|T_{rr}| & \text{if } \omega > \omega_{ref} \\ [-|T_{rr}|, |T_{rr}|] & \text{if } \omega = \omega_{ref} \\ |T_{rr}| & \text{if } \omega < \omega_{ref} \end{cases}$$
(2.14)

where ω_{ref} is defined by

$$\omega_{ref} = \begin{cases} \omega + c_3 \left(\omega - \frac{v_x}{R}\right) & \text{if } i_s < 0 \& T_{rr} < 0 \\ \frac{v_x}{R} & \text{otherwise} \end{cases}$$
 (2.15)

where R is the wheel radius and c_3 is the same as that used in Eq. (2.12). Again, by inspection, the validity of the proposed relations in Eqs. (2.14) and (2.15) can be verified similar to the arguments detailed above for the traction force. It should be noted that the assumed positive directions for T_{rr} , ω , and v_x are shown in Fig. 2.3. With this definition, a negative T_{rr} acts in the opposite direction of the angular velocity ω , while a positive T_{rr} in the direction of ω . Different cases of motion are briefly discussed below:

- Case 1: Wheel moves to the right $(v_x > 0)$ with $i_s > 0$: In this case, positive i_s results in $T_{rr} < 0$, and both conditions $v_x > 0$ and $i_s > 0$ lead to $\omega > v_x/R$; therefore, from Eq. (2.15) $\omega_{ref} = v_x/R$ and in turn $\omega > \omega_{ref}$. From Eq. (2.14), T_{rrd} becomes $-|T_{rr}|$, as expected.
- Case 2: $v_x > 0$ with $i_s < 0$, which implies that $\omega < v_x/R$. In this case, if $T_{rr} < 0$, ω_{ref} becomes $\omega + c_3(\omega v_x/R)$ from Eq. (2.15), and thus, $\omega > \omega_{ref}$. Therefore, T_{rrd} becomes $-|T_{rr}|$, as expected.

 In addition, if $T_{rr} > 0$, ω_{ref} becomes equal to v_x/R from Eq. (2.15), and therefore, $\omega < \omega_{ref}$, which results in $T_{rrd} = |T_{rr}|$. This is also the expected result.
- Case 3: $v_x < 0$ with $i_s > 0$, which implies that $\omega < 0$ and $|\omega| > |v_x|/R$, which means $\omega < v_x/R$. In this case, $T_{rr} < 0$ and, as explained above, T_{rr} should resist the

angular motion of the wheel in its current direction of motion. Therefore, it is expected to see a positive T_{rrd} , as $\omega < 0$.

From Eq. (2.15), $\omega_{ref} = v_x/R$. As $\omega < \omega_{ref}$, T_{rrd} becomes $|T_{rr}|$, which is the expected result, too, as explained above.

Case 4: $v_x < 0$ with $i_s < 0$, which implies that $|\omega| < |v_x|/R$ and therefore, $\omega > (v_x/R)$. In this case, if $T_{rr} < 0$, ω_{ref} becomes $\omega + c_3(\omega - v_x/R)$ from Eq. (2.15), and thus, $\omega < \omega_{ref}$. Therefore, $T_{rrd} = |T_{rr}|$ is the outcome of Eq. (2.14), which again is the expected result. In addition, if $T_{rr} > 0$, ω_{ref} becomes equal to v_x/R from Eq. (2.15), and therefore, $\omega > \omega_{ref}$, which results in $T_{rrd} = -|T_{rr}|$. This is also the expected result.

Similar to Eq. (2.11), Eq. (2.14) can lead to an LCP formulation, as will be explained in Section 2.4.4.

In addition, based on its physical nature, the rolling resistance R_c , also referred to as compaction resistance, is related to v_x , the velocity of the centre of the wheel; it always opposes v_x and can vanish when v_x does. Based on this, the revised formulation for compaction resistance R_{cd} can be expressed as:

$$R_{cd}(v_x) = \begin{cases} -|R_c| & \text{if } v_x > 0\\ [-|R_c|, |R_c|] & \text{if } v_x = 0\\ |R_c| & \text{if } v_x < 0 \end{cases}$$
 (2.16)

which has a form similar to Eq. (2.11) and can lead to an LCP formulation, as will be explained in Section 2.4.4.

2.4.3 Non-planar Motion on Flat Terrain

As mentioned above, in the development of semi-empirical models, like the Bekker and Wong-Reece models, planar motion was considered. The non-planar motion discussed in this section has two features: (*i*) lateral forces, developed during steering manoeuvres,

CHAPTER 2. SEMI-EMPIRICAL MODELS IN A MULTI-BODY DYNAMICS ENVIRONMENT

for example, and (ii) penetration of a cylindrical wheel such that the cylinder axis is not parallel to the terrain.

2.4.3.1 Lateral Forces

The lateral force F_l is composed of two parts; one is related to the shear stress developed under the wheel, F_{ls} , while the other is related to bulldozing resistance that acts on the side of the wheel, F_{lb} :

$$F_{l} = F_{ls} + F_{lh} (2.17)$$

Similar to the approach of Schwanghart (1968), and Yoshida and Ishigami (2004), F_{ls} can be calculated by integrating the shear stress under the wheel, as

$$F_{ls} = Rb \int_{\theta_2}^{\theta_1} \left[c + \sigma(\theta) \tan(\phi) \right] \left[1 - \exp(-j_y(\theta)/K_y) \right] d\theta, \qquad (2.18)$$

where K_y is the shear deformation modulus in the lateral direction; j_y is the shear deformation in the lateral direction and computed by Yoshida and Ishigami (2004) as

$$j_{\nu}(\theta) = R(1 - i_s)(\theta_1 - \theta) \tan \beta_s, \tag{2.19}$$

where β_s is the side slip angle, which is the angle between the wheel centre velocity vector and the wheel forward direction:

$$\beta_s = \operatorname{atan}\left(\frac{v_y}{v_x}\right) \tag{2.20}$$

with v_x and v_y denoting the forward and lateral components of the wheel centre velocity, respectively.

REMARK 4. Equation (2.19) needs special treatment: when $\beta_s \to 90^\circ$, $j_y \to \infty$, which in turn means that the shear stress becomes equal to the shear strength, as the exponentially

decaying term in Eq. (2.18) becomes zero. In the implementation in Vortex, β_s is limited to a slightly smaller value than 90° to avoid singularities, while its physical effect is preserved.

In addition, F_{lb} is computed by means of the Fundamental Earthmoving Equation (FEE) of Reece (1964) and by performing integration over the contact area in the sidewall of the wheel. In this approach, it is assumed that the sidewall of the wheel behaves similar to the cutting blade of a bulldozer.

According to FEE, the bulldozing force is composed of four terms, which represent the effects of soil density and cohesion, surcharge on the soil surface, and adhesion between blade and soil. Based on the shape of the failure surface, four *N*-factors have to be determined as well (Reece, 1964). The shape of the failure surface depends on the soil internal shear angle and the friction between blade and soil, as well as the blade shape and the soil mass involved. McKyes (1985) presented the method of *trial wedges*, in which the failure surface is approximated by a plane, which becomes a straight line in a 2D model, as shown in Fig. 2.7. Therefore, the above-mentioned *N*-factors can be readily determined, using the static equilibrium of the failing wedge.

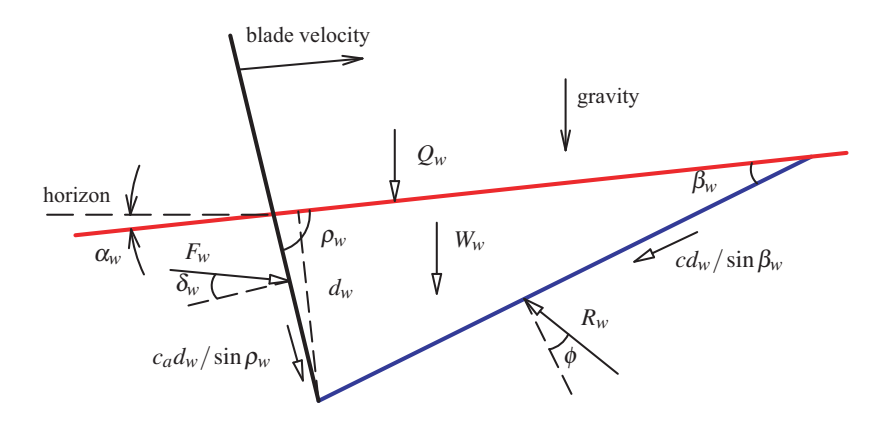


FIGURE 2.7. Forces acting on the soil wedge.

According to McKyes (1985), the bulldozing force per unit tool width can be expressed

$$F = \gamma d_w^2 N_\gamma + c d_w N_c + Q_w N_O + c_a d_w N_a \tag{2.21}$$

From the static equilibrium of all forces applied on the wedge, the *N*-factors are determined as

$$N_{\gamma} = \frac{(\cot \rho_w + \cot \beta_w) \sin(\alpha_w + \phi + \beta_w)}{2 \sin(\delta_w + \rho_w + \phi + \beta_w)}, \quad N_Q = \frac{\sin(\alpha_w + \phi + \beta_w)}{\sin(\delta_w + \rho_w + \phi + \beta_w)}$$
(2.22a)

$$N_c = \frac{\cos\phi}{\sin\beta_w \sin(\delta_w + \rho_w + \phi + \beta_w)}, \quad N_a = \frac{-\cos(\rho_w + \phi + \beta_w)}{\sin\rho_w \sin(\delta_w + \rho_w + \phi + \beta_w)}$$
(2.22b)

with soil slope inclination angle α_w , blade/soil angle ρ_w , blade penetration depth d_w , soil failure angle β_w , soil internal friction angle ϕ , soil cohesion c, specific weight of the soil γ , blade/soil friction angle δ_w , blade/soil adhesion c_a and surcharge force per tool width Q_w . In this method, β_w is determined such that it causes the least resistance from soil. According to McKyes (1985), the proper value for β_w minimizes N_γ ; however, it can also be approximated as the passive Rankine state angle (Wong, 2008):

$$\beta_w = \pi/4 - \phi/2 \tag{2.23}$$

It is also noted that usually the angle between the wheel side and soil surface, represented by the blade/soil angle ρ_w , is around 90°. Using Eq. (2.21), the lateral force from the bulldozing resistance on the sidewall of a cylindrical wheel is obtained by integrating over the submerged portion of the wheel sidewall, as shown in Fig. 2.8, as

$$F_{lb} = R \int_{-\theta_1}^{\theta_1} (\gamma \zeta(\theta)^2 N_{\gamma} + c \zeta(\theta) N_c + Q_w N_Q + c_a \zeta(\theta) N_a) \cos \theta \sin \beta_s d\theta, \qquad (2.24)$$

where the surcharge force per tool width Q_w can be obtained by assuming a particular shape for soil accumulation on top of the original soil surface. In addition, the slip angle β_s is included in the formulation, as, in reality, with zero slip angle, i.e., no lateral velocity, there will be no bulldozing on the sidewall.

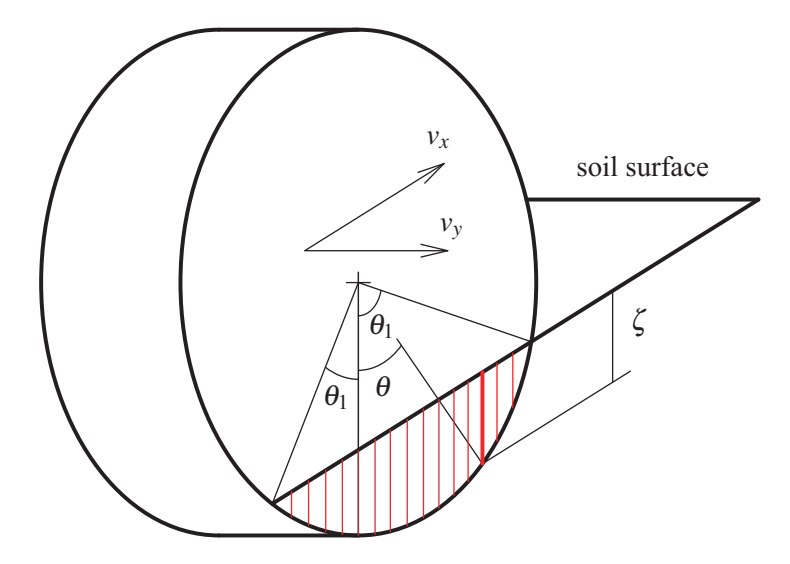


FIGURE 2.8. Schematic illustration of determination of bulldozing force via integration over the submerged portion of the wheel sidewall

It should be mentioned that the range of applicability of this formula is limited to toolsoil angles below 90° and slightly above 90° . In fact, the sidewall of a wheel and terrain usually makes a 90° angle, which makes the method of trial wedges a good candidate for this application. In addition, the *N*-factors, Eqs. (2.22a, 2.22b), become singular when $\sin(\delta_w + \rho_w + \phi + \beta_w)$ becomes zero, which is the case when the summation of these angles becomes 180° . In this situation, the forces F_w and F_w become collinear and, therefore, no static equilibrium for the forces acting on the wedge can be obtained. Furthermore, no static equilibrium can be achieved when the summation of these angles becomes larger than 180° . However, when ρ_w is around 90° or smaller, the solution is valid.

It should also be mentioned that, in this thesis, the friction between the sidewall of the wheel and soil is neglected, i.e., $\delta_w = 0$ is used here.

According to recent findings by Ding et al. (2011b), in cases of a large ρ_w , a single wedge is not enough. In this case, the approximation of the failure pattern using two wedges

⁴The other cases, summation of angles equal zero or 360°, do not have physical meanings.

leads to more acceptable results. However, as mentioned above, using a single wedge is appropriate for modelling bulldozing forces on the sidewall of a cylindrical wheel, with a negligible sidewall/soil friction.

The idea of decomposing the lateral force into a shear part and a bulldozing resistance part is similar to the approach proposed by Ishigami et al. (2007). However, the part related to bulldozing resistance is different. In the above reference, the bulldozing resistance is not related to the velocity direction of the wheel, which results in high bulldozing force at small side-slip angles—an outcome which is not physically correct. In addition, the method of trial wedges of McKyes (1985) is used here, as opposed to the Hegedus (1960) bulldozing force model. A benefit of using the former approach over Hegedus is that the slope of the terrain can also be included in the formulation.

Similar to the approach used for the traction force in Section 2.4.2.3, the lateral component of the velocity of contact point A of the wheel in Fig. 2.3, referred to as v_{Ay} , is used to set up the revised model for the lateral force F_{ld} as a set-valued force law:

$$F_{ld}(v_{Ay}) = \begin{cases} -|F_l| & \text{if } v_{Ay} > 0\\ [-|F_l|, |F_l|] & \text{if } v_{Ay} = 0\\ |F_l| & \text{if } v_{Ay} < 0 \end{cases}$$
 (2.25)

Similar to Eq. (2.11) that was proposed for the traction force, Eq. (2.25) leads to the formulation of a linear complementarity problem, as explained in Section 2.4.4.

2.4.3.2 Wheel Axis Not Parallel to the Terrain

In *Vortex*, when two or more bodies are in contact, several unilateral contact constraints are placed in the contact region, depending on the shape of the colliding objects. In the case of contact between a plane and the rolling side of a cylindrical wheel, one or two

contact points, as shown in Fig. 2.9, are generated. For each contact point, the sinkage is determined as the minimum distance from that point to the plane, as shown in Fig. 2.9.

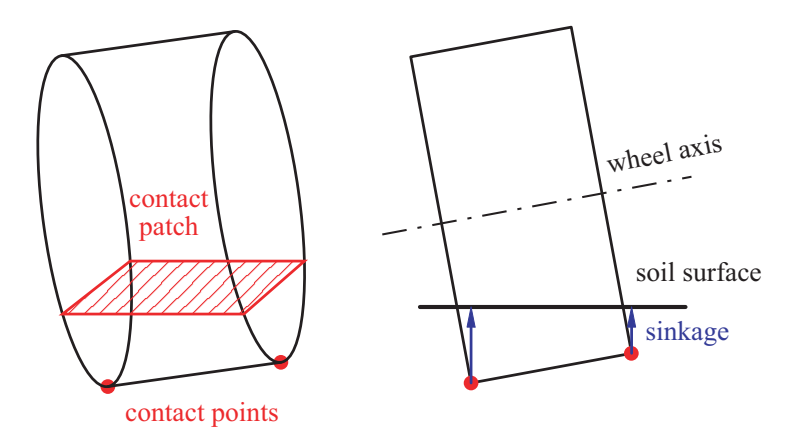


FIGURE 2.9. Illustration of contact points between a rolling cylindrical wheel and a planar terrain.

The stiffness and damping coefficients of each contact point are then set according to Eqs. (2.2)–(2.4). The traction force F_t is determined from Eq. (1.8) and is divided by 2 to compensate for the two-point contact model employed. For each contact point, one constraint with set-valued force law is added to the simulation and is set up according to Eq. (2.11), to model the traction force. In addition, as the velocity of the wheel centre is used to form the constraint associated with the compaction resistance R_c , Eq. (2.16), a single constraint is added per wheel for the compaction resistance, based on the average value of R_c determined from the two contact points. Similarly, the residual resistance torque T_{rr} is determined from Eqs. (1.9) and (2.13), for each contact point. Their average value is used to set up a single constraint per wheel for the residual resistance torque, according to Eq. (2.14).

It should be noted that the terramechanics models are developed and tested for the case of similar sinkages on both sides. Therefore, in the case of large differences between the sinkages on the two sides of the wheel, as schematically shown in Fig. 2.9, this implementation can only be seen as an approximation.

2.4.4 Soil Reactions in a Complementarity Formulation

A Linear Complementarity Problem is expressed as (Stewart, 2000):

Find
$$\mathbf{u}_1 \in \mathbb{R}^m$$
 such that:

$$\begin{cases} \mathbf{w}_1 = \mathbf{B}_1 \mathbf{u}_1 + \mathbf{b}_1 \\ \mathbf{w}_1 \ge 0 \quad ; \quad \mathbf{u}_1 \ge 0 \quad ; \quad \mathbf{w}_1^T \mathbf{u}_1 = 0 \end{cases}$$
(2.26)

where $\mathbf{B}_1 \in \mathbb{R}^{m \times m}$, $\mathbf{b}_1 \in \mathbb{R}^m$, and $\mathbf{w}_1 \in \mathbb{R}^m$. Moreover, $\mathbf{x} \ge 0$ indicates that all components of \mathbf{x} are greater than or equal to zero.

According to Acary and Brogliato (2008), a generalization of an LCP with an additional system of linear equations, which is referred to as Mixed Linear Complementarity Problem (MLCP), can be expressed as:

Find $\mathbf{u} \in \mathbb{R}^{m_1}$ and $\mathbf{w} \in \mathbb{R}^{m_2}$ such that:

$$\begin{cases}
\mathbf{B}\mathbf{u} + \mathbf{C}\mathbf{w} + \mathbf{b} = \mathbf{0}_{m_1 \times 1} \\
\mathbf{y} = \mathbf{D}\mathbf{u} + \mathbf{E}\mathbf{w} + \mathbf{d} \\
\mathbf{w} \ge 0 \quad ; \quad \mathbf{y} \ge 0 \quad ; \quad \mathbf{w}^T \mathbf{y} = 0
\end{cases}$$
(2.27)

where $\mathbf{B} \in \mathbb{R}^{m_1 \times m_1}$, $\mathbf{C} \in \mathbb{R}^{m_1 \times m_2}$, $\mathbf{b} \in \mathbb{R}^{m_1}$, $\mathbf{y} \in \mathbb{R}^{m_2}$, $\mathbf{D} \in \mathbb{R}^{m_2 \times m_1}$, $\mathbf{E} \in \mathbb{R}^{m_2 \times m_2}$, and $\mathbf{d} \in \mathbb{R}^{m_2}$.

Anitescu and Potra (1997) showed that using explicit Euler integration, a multiboy dynamics system having unilateral contact with dry friction and bilateral constraints can be formulated as a MLCP. Here we show that a multibody model with no constraints except for the kinematic constraints with the set-valued force laws expressed in Eqs. (2.11), (2.14), (2.16), and (2.25), can also be formulated as a MLCP. It then follows that a multibody system having unilateral contact with dry friction, bilateral constraints, and the constraints in Eqs. (2.11), (2.14), (2.16), and (2.25) can also be formulated as a MLCP, following the procedure explained by Anitescu and Potra (1997). The latter discussion, however, is avoided as it lies outside of the scope of the thesis.

In Sections 2.4.2.3 and 2.4.3, soil reactions were formulated in the form

$$f_d(x) = \begin{cases} -f & \text{if } x > x_1 \\ [-f, f] & \text{if } x = x_1 \\ f & \text{if } x < x_1 \end{cases}$$
 (2.28)

where f is a positive scalar and x is the complementary variable of f_d . It is noted that f and x are known a priory. Equation (2.28) is the general form for Eqs. (2.11), (2.14), (2.16), and (2.25). For example, in the case of the traction force expressed by Eq. (2.11), f, f_d , f, and f represent f, f, f, f, f, and f represent f, f, f, f, f, f, respectively.

Consider the dynamic equations of an n-degree of freedom system with the kinematic constraint and the set-valued force law expressed in Eq. (2.28) as:

$$\mathbf{M}(\mathbf{q})\dot{\mathbf{v}} + \mathbf{f}_c(\mathbf{q}, \mathbf{v}) = \mathbf{f}_a + \mathbf{A}^T f_d$$
 (2.29)

where \mathbf{M} is the n by n mass matrix, $\mathbf{q} \in \mathbb{R}^n$ and $\mathbf{v} \in \mathbb{R}^n$ are the vectors of generalized coordinates and velocities, respectively, $\mathbf{f}_c \in \mathbb{R}^n$ denotes the Coriolis and centrifugal forces, $\mathbf{f}_a \in \mathbb{R}^n$ is the applied forces, and \mathbf{A} is the constraint Jacobian obtained by:

$$\mathbf{A} = \frac{\partial x}{\partial \mathbf{v}} \tag{2.30}$$

It is noted that in our formulation, only one constraint with the set-valued force law, Eq. (2.28), is included in Eq. (2.29). Therefore, the constraint Jacobian **A** belongs to $\mathbb{R}^{1\times n}$. The extension of this formulation to more than one constraint is straightforward.

As A is the constraint Jacobian, the constraint velocity x is related to the generalized velocities by

$$x = \mathbf{A}\mathbf{v} \tag{2.31}$$

CHAPTER 2. SEMI-EMPIRICAL MODELS IN A MULTI-BODY DYNAMICS ENVIRONMENT

Following the procedures explained by Acary and Brogliato (2008) and Anitescu and Potra (1997), Eqs. (2.29) and (2.28) can be reformulated as a MLCP, as we prove below.

Let us introduce slack variables λ_1 and λ_2 , and define \overline{f}_d as

$$\overline{f}_d = \frac{\lambda_1 - \lambda_2}{2} \tag{2.32}$$

where λ_1 and λ_2 are the solutions of

$$\begin{cases} \lambda_{1} \geq 0 & ; \quad (x - x_{1}) + |x - x_{1}| \geq 0 & ; \quad \lambda_{1} \left[(x - x_{1}) + |x - x_{1}| \right] = 0 \\ \lambda_{2} \geq 0 & ; \quad -(x - x_{1}) + |x - x_{1}| \geq 0 & ; \quad \lambda_{2} \left[-(x - x_{1}) + |x - x_{1}| \right] = 0 \\ \lambda_{1} + \lambda_{2} = 2f \end{cases}$$
 (2.33)

By inspection, one can realize that in Eq. (2.33), $x > x_1$ leads to $\lambda_1 = 0$ and $\lambda_2 = 2f$. In addition, $x < x_1$ results in $\lambda_1 = 2f$ and $\lambda_2 = 0$. Moreover, if $x = x_1$, then $\lambda_1 \in [0, 2f]$ and $\lambda_2 \in [0, 2f]$ subject to $\lambda_1 + \lambda_2 = 2f$.

Now we claim that the value of f_d is equal to \overline{f}_d , determined from Eq. (2.32). For $x \neq x_1$, this is trivial, as mentioned above. Now let us consider $x = x_1$.

By eliminating λ_2 from Eq. (2.32) and the last relation of Eq. (2.33), \overline{f}_d is obtained as

$$\overline{f}_d = \lambda_1 - f \tag{2.34}$$

When $x = x_1$, $0 \le \lambda_1 \le 2f$, as mentioned above. This means that $-f \le \lambda_1 - f \le f$, and therefore, $\overline{f}_d \in [-f, f]$. This concludes our claim, i.e., f_d and \overline{f}_d are equivalent.

Now, let us introduce x^+ and x^- as

$$x^{+} = [(x - x_{1}) + |x - x_{1}|]/2 = \max(0, x - x_{1}) \ge 0$$

$$x^{-} = [(x - x_{1}) - |x - x_{1}|]/2 = \min(0, x - x_{1}) \le 0$$
(2.35)

Therefore, Eq. (2.33) can be expressed as:

$$\begin{cases} \lambda_{1} \geq 0 & ; \quad x^{+} \geq 0 & ; \quad \lambda_{1}x^{+} = 0 \\ \lambda_{2} \geq 0 & ; \quad -x^{-} \geq 0 & ; \quad \lambda_{2}x^{-} = 0 \\ x - x_{1} = x^{+} + x^{-} \\ \lambda_{1} + \lambda_{2} = 2f \end{cases}$$
(2.36)

Combination of Eqs. (2.29), (2.31), (2.32), and (2.36), and noting that f_d and \overline{f}_d are equivalent, lead to the MLCP defined in Eq. (2.27), where $m_1 = n + 2$, $m_2 = 2$, $\mathbf{E} = \mathbf{0}_{2\times 2}$, $\mathbf{d} = \mathbf{0}_{2\times 1}$, and \mathbf{B} , \mathbf{u} , \mathbf{C} , \mathbf{w} , \mathbf{b} , and \mathbf{D} are given below

$$\mathbf{u} = \begin{bmatrix} \dot{\mathbf{v}} \\ \lambda_1 \\ -x^- \end{bmatrix} , \quad \mathbf{w} = \begin{bmatrix} x^+ \\ \lambda_2 \end{bmatrix}$$
 (2.37)

$$\mathbf{B} = \begin{bmatrix} \mathbf{M} & -(1/2)\mathbf{A}^T & \mathbf{0}_{n\times 1} \\ \mathbf{0}_{1\times n} & 1 & 0 \\ -\mathbf{A} & 0 & -1 \end{bmatrix} , \quad \mathbf{C} = \begin{bmatrix} \mathbf{0}_{n\times 1} & (1/2)\mathbf{A}^T \\ 0 & 1 \\ 1 & 0 \end{bmatrix}$$
(2.38)

$$\mathbf{b} = \begin{bmatrix} \mathbf{f}_c - \mathbf{f}_a \\ -2f \\ x_1 \end{bmatrix} , \quad \mathbf{D} = \begin{bmatrix} \mathbf{0}_{1 \times n} & 1 & 0 \\ \mathbf{0}_{1 \times n} & 0 & 1 \end{bmatrix}$$
 (2.39)

It should be mentioned that the condition $\mathbf{w}^T \mathbf{y} = 0$ implies $\lambda_1 x^+ = 0$ and $\lambda_2 x^- = 0$, because $\lambda_1 x^+ \ge 0$ and $-\lambda_2 x^- \ge 0$, from Eq. (2.36). This concludes our claim.

Furthermore, using an explicit Euler integration scheme, Eq. (2.29) becomes:

$$\mathbf{M}(\mathbf{v}^{(l+1)} - \mathbf{v}^{(l)}) + h\mathbf{f}_c = h\mathbf{f}_a + h\mathbf{A}^T f_d$$
 (2.40)

where h is the integration time-step. The superscript (l) on \mathbf{v} symbolizes the general velocities at time-step l. Similarly, combining Eq. (2.40) with Eqs. (2.32) and (2.36) leads to the MLCP defined in Eq. (2.27) with $\mathbf{E} = \mathbf{0}_{2\times 2}$, $\mathbf{d} = \mathbf{0}_{2\times 1}$, and

$$\mathbf{u} = \begin{bmatrix} \mathbf{v}^{(l+1)} \\ \lambda_1 \\ -x^- \end{bmatrix} \quad ; \quad \mathbf{w} = \begin{bmatrix} x^+ \\ \lambda_2 \end{bmatrix}$$
 (2.41)

$$\mathbf{B} = \begin{bmatrix} \mathbf{M} & -(h/2)\mathbf{A}^T & \mathbf{0}_{n\times 1} \\ \mathbf{0}_{1\times n} & 1 & 0 \\ -\mathbf{A} & 0 & -1 \end{bmatrix} ; \mathbf{C} = \begin{bmatrix} \mathbf{0}_{n\times 1} & (h/2)\mathbf{A}^T \\ 0 & 1 \\ 1 & 0 \end{bmatrix}$$
(2.42)

$$\mathbf{b} = \begin{bmatrix} -\mathbf{M}\mathbf{v}^{(l)} + h(\mathbf{f}_c - \mathbf{f}_a) \\ -2f \\ x_1 \end{bmatrix} ; \mathbf{D} = \begin{bmatrix} \mathbf{0}_{1 \times n} & 1 & 0 \\ \mathbf{0}_{1 \times n} & 0 & 1 \end{bmatrix}$$
 (2.43)

The interested reader is referred to (Acary and Brogliato, 2008), (Anitescu and Potra, 1997), and (Pfeiffer and Glocker, 1996) for further discussion on this topic.

2.4.5 Motion on Rough Terrain and the Multipass Effect

In the computation of soil reactions based on semi-empirical models, estimation of a wheel/ground penetration value (wheel sinkage) is a key element. The sinkage is used to determine θ_1 and θ_2 , which are in turn used to calculate the soil reactions. In the semi-empirical Bekker models, it is assumed that the wheel has a cylindrical geometry and the terrain is flat (cf. Figure 1.1). In a basic implementation of such models, a cylindrical geometry for the wheel and a locally flat surface, e.g., a plane, for the terrain could be used as mentioned above.

In order to consider irregularities in the terrain surface, a high resolution height-field (HF) is used here for terrain representation. Determination of a sinkage value suitable for

use in the semi-empirical models, however, is far more difficult in this case. If, here too, we were to apply the basic approach described above and attempt to determine the sinkage from wheel and terrain geometries, we would have to deal with a general cylinder/HF intersection algorithm. Depending on the HF-resolution, this can be computationally a very expensive task. In addition, for arbitrary wheel interactions such as the wheel driving on high-frequency rough ground or entering the onset of an incline, finding a reasonable penetration depth that also changes smoothly from one simulation step to the next is algorithmically challenging, yet it is a requirement for stable simulation.

Here, this challenge is met by reducing the complex geometrical problem of the overlap between a cylindrical wheel and a general HF to the simple cylinder/plane intersection case. This is achieved by approximating the wheel/terrain contact patch locally by a plane. First, all the HF vertices in the wheel *footprint* are identified—see Fig. 2.10. Those vertices can be obtained by first determining a bounding box of the wheel in local height-field space and projecting it on the height-field. Then, for each of these vertices a ray cast is performed onto the wheel geometry along the local up-axis of the height-field. If a hit with the geometry is obtained, the vertex is considered as part of the footprint in the given simulation step. If the hit point lies below the HF, the wheel penetrates the ground at that point, and the vertex is called active. It is clear that the set of active vertices approximates the surface with which the wheel is in contact at any step in the simulation. This observation can be used to obtain the penetration sought as follows: at each simulation step a plane is found from the point cloud defined by the positions of the currently active vertices, via a least-squares fit. This plane is referred to as the least-squares plane. This plane intersects the cylindrical wheel by definition and is used as an approximation of the wheel/ground contact patch at the current simulation step. Finally, a cylinder/plane intersection test is conducted, from which the cylinder penetration can be readily obtained.

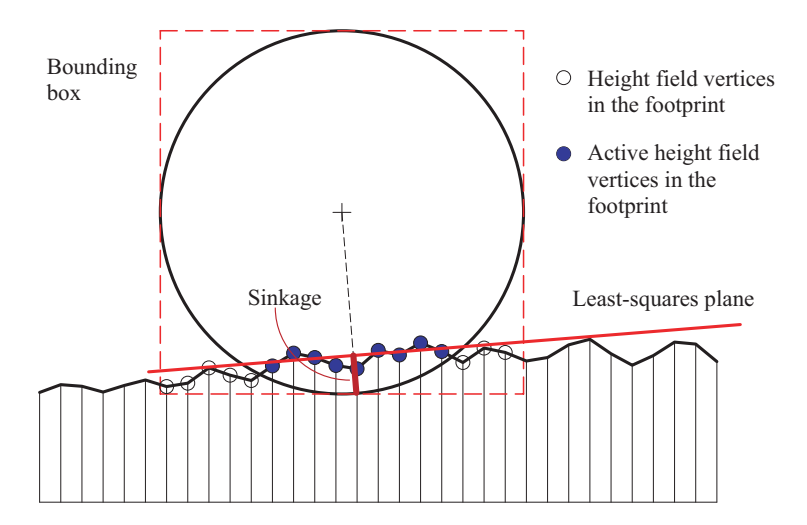


FIGURE 2.10. Schematic of height-field/wheel interaction and the approximating least-squares plane

The compaction aspect of a wheel passing over soft ground can also be captured with the HF-based terrain representation. Soil compaction is governed on one hand by a geometric change of the terrain surface, and on the other hand by a change of the compaction state of the soil material. Based on this observation, the HF data structure is enhanced by additional data entries associated with each vertex representing soil-hardening parameters, which capture the state of compaction in the HF at the corresponding location. Note that the type of parameters needed strongly depends on the type of wheel-soil interaction model used in simulation. The compaction of soil is modelled by evolving both the height and the soil-hardening parameters associated with the vertices in the wheel footprint. For semi-empirical models, the multi-pass approach of Wong (2010) has been adapted to this implementation. In this context, the wheel sinkage used in the pressure-sinkage relation is a key input for the evolution of soil hardening parameters.

The changes in the geometric properties and the compaction state of soil can be derived from the sinkage of the wheel in the ground. The determination of the wheel footprint allows for monitoring the wheel sinkage at each vertex of the footprint. This yields a discretized representation of the geometric effects of deformation occurring at the wheel/ground

interface at each simulation step. In order to obtain permanent (plastic) terrain deformation, at some point the sinkage data obtained has to be transferred to the HF. For a given HF vertex, this corresponds to lowering the height as well as updating the soil-hardening parameter at this vertex. In this approach, this transfer is conducted for a given vertex if it has just left the wheel footprint. In other words, the transfer is carried out in frame k if the vertex was part of the wheel footprint in frame k-1 and is not detected in the footprint any more in frame k.

In this way, the terrain surface is not modified while the wheel is still passing over it, an approach that avoids introducing disturbances in the simulation. Changing the HF surface while it is still in contact with the wheel would otherwise directly affect the computation of the sinkage parameter, which is used as the main input for computation of the soil reaction forces. As a consequence, the soil reaction forces would be altered due to the actions of the compaction model implementation, which is not desired. By deferring the modification of the deforming soil at a given HF location until after the wheel has passed, this issue is effectively avoided.

With the approach described above, all sorts of soil compaction effects can be represented. Deformation of a perfectly plastic soil, for instance, would be achieved by maintaining the maximum sinkage at each vertex in the footprint.

2.4.5.1 Basic Relations

As mentioned above, the multipass approach of Wong (2010) is used here, in which the pressure-sinkage relation follows the curve illustrated in Fig. 2.11. During elastic reloading or unloading, part AB in Fig. 2.11, the pressure p is a linear function of the total sinkage z_t , i.e.,

$$p = p_u - k_u(z_u - z_t) (2.44)$$

where z_t is the sinkage measured from the uncompacted soil surface, p_u refers to the pressure at point A, which is the pressure when the unloading starts, z_u is the total sinkage at which the unloading has started, and k_u is the slope of the loading-unloading curve, defined by Wong (2010) as:

$$k_u = k_0 + A_u z_u \tag{2.45}$$

in which k_0 and A_u are material constants that define the elastic unloading/reloading behaviour.

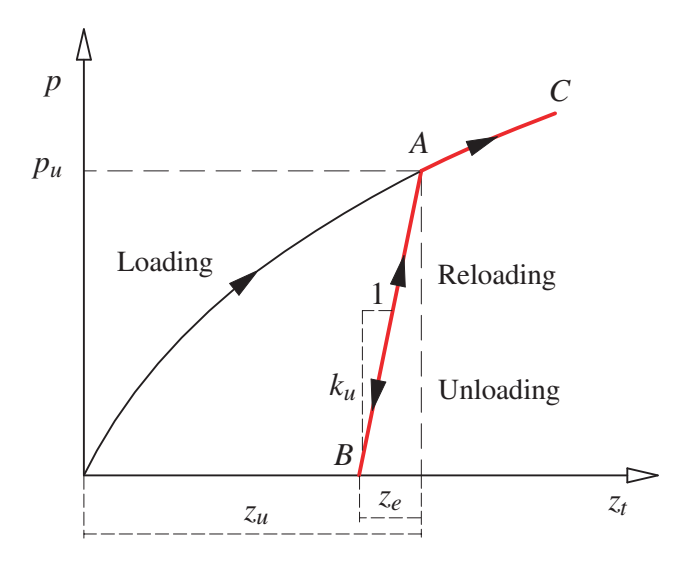


FIGURE 2.11. Schematic of unloading/reloading model of Wong used to find normal stress distribution with multipass.

It should be noted that in this model the total elastic sinkage z_e is assumed to be smaller than z_u . However, referring to the Bekker pressure-sinkage relationship, Eq. (1.3), if the sinkage exponent n is smaller than unity, the tangent line to the pressure-sinkage relation at $z_t = 0$ becomes vertical, which means an infinite slope for the tangent line. This in turn indicates that when n < 1, depending on the value of k_0 , there exists a z_u value at which $k_u z_u$ equals p_u . For values of z_u smaller than this value, z_e will be greater than z_u , which contradicts the above assumption that z_e must always be smaller than z_u . To address this issue, in this case, the elastic unloading line is modified to connect the origin to point A.

Therefore, in this case the pressure is obtained using Eq. (2.46), instead of Eq. (2.44), for the unloading case, and the soil vertex is flagged as uncompacted (not hardened):

$$p = \frac{p_u}{z_u} z_t \tag{2.46}$$

In addition, if $z_t \ge z_u$, the pressure is obtained from the pressure-sinkage equation for an uncompacted soil, e.g., Eq. (1.3) for the Bekker relation. It is clear that if a wheel is moving over already compacted soil, e.g., in a second pass, the penetration of the wheel into the ground is measured from an already compacted soil surface. However, the value of z_t is needed in Eqs. (2.44) and (2.46). The total sinkage z_t can be readily obtained as shown in Eq. (2.47) from the current wheel sinkage on compacted soil z, and the past maximal sinkage z_u , which is the hardening parameter

$$z_t = z + z_u - z_e \tag{2.47}$$

where z_e is obtained from

$$z_e = p_u/k_u \tag{2.48}$$

It should be noted that the past maximal sinkage z_u is a parameter of our hardening model, which is stored per vertex and modified as a result of multiple wheel passes (multipass). Furthermore, the shear stress is obtained using Eq. (2.8).

2.4.5.2 Unloading-Reloading Relations in Various Wheel-soil Interaction Models

In this approach, after a wheel has passed, the HF vertices that have been in contact are modified (both their height and hardening parameter). In the unloading/reloading model of the terrain, as discussed above, the hardening is a consequence of the maximum total sinkage.

In this section, two cases are of interest. In the first case, the Bekker model is discussed, while in the second case, the Wong and Reece (1967a) model and another model explained by Ishigami et al. (2007) are considered. Normal stress distributions under a rigid wheel for these models are displayed in Fig. 2.2.

There are two issues that need to be discussed for each model: (*i*) the amount of compaction (soil deformation) and hardening that is maintained in the terrain after the wheel has passed, and (*ii*) the stress distribution when a wheel is moving on an already compacted soil.

Case 1: Bekker model:

In this model, the point of maximum sinkage under the wheel corresponds to the maximum pressure; therefore, the maximum deformation can be directly used to update the vertex properties.

In order to update the vertex height and *permanent* hardening property, in the HF data structure two additional entries are also stored, maximum penetration and *temporary* hardening. During the time that a vertex is in contact with the wheel, vertex height and permanent hardening remain unchanged but maximum penetration and temporary hardening change. When the vertex has left the contact, maximum penetration and temporary hardening are used to update vertex height and permanent hardening, respectively.

In addition, when the Bekker model is used to find the soil reactions on a wheel moving on an already compacted soil, the normal stress distribution is directly determined based on the approach explained in Section 2.4.5.1. In this regard, using $\zeta(\theta)$, illustrated in Fig. 1.1, instead of z in Eq. (2.47), z_t is determined as a function of θ . Then, $z_t(\theta)$ is used to interpret and compute the pressure distribution, as explained in Section 2.4.5.1.

Furthermore, by knowing the normal stress at the bottom-dead-centre p_{max} , which is the normal stress at $z_t(\theta = 0)$, a nonzero exit angle is found from the elastic rebound of soil as (see Fig. 2.12):

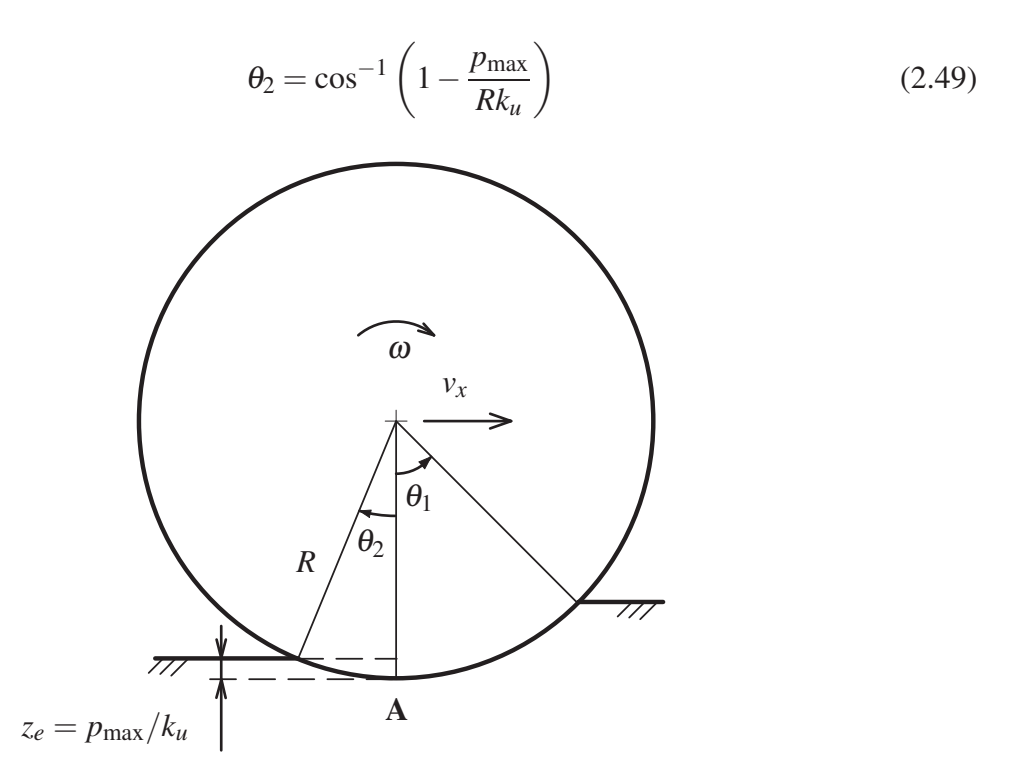


FIGURE 2.12. Determining the exit angle in the Bekker model from the elastic rebound. p_{max} is the normal stress at point **A**.

Case 2: WR and Ishigami et al. (2007) models:

In these models, the maximum pressure and maximum deformation do not occur at the same location as opposed to the case of the Bekker model. Here, the hardening parameter is updated based on the maximum normal stress but the soil height is set according to the maximum deformation that each vertex experiences. The elastic rebound is not considered because in these models, the normal stress at the exit angle reaches zero. By using the λ parameter, which was introduced by Ishigami et al. (2007) to find the exit angle, the total plastic deformation, that is set in these models for every vertex, is determined as

$$z_p = z_{\text{max}}(1 - \lambda) \tag{2.50}$$

where z_{max} is the maximum deformation the vertex has experienced during the contact with the wheel. The height of the soil vertex once the wheel has passed is thus consistent with

the assumptions made in the WR and Ishigami et al. (2007) models. For WR we use $\lambda = 0$ and for the Ishigami et al. (2007) model λ is set according to the material properties. For more details, the reader is referred to (Ishigami et al., 2007).

In addition, when the wheel moves over an already compacted soil, the normal stress for θ between θ_1 and θ_M follows the reloading equation and is directly obtained as in the Bekker model. For θ between θ_M and the exit angle θ_2 , the normal stress follows the scaled symmetry assumed by Wong and Reece (1967a) and Ishigami et al. (2007), where the symmetry line is identified by θ_M , the location of maximum normal stress. The normal stress distribution is schematically displayed in Fig. 2.13.

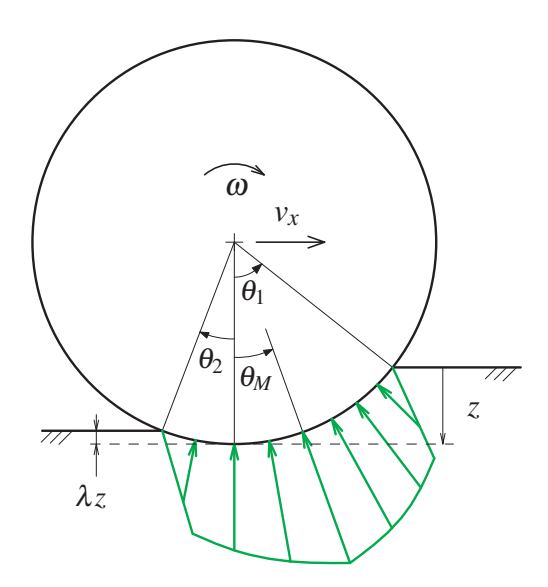


FIGURE 2.13. Schematic of normal stress distribution under a rigid wheel moving over the track of another wheel, using the Wong and Reece (1967a) and Ishigami et al. (2007) models.

In Fig. 2.13, the front wheel portion, represented by the interval $[\theta_1, \theta_M]$, touches precompacted soil. In this zone, the soil reacts elastically at the beginning, represented in the proposed model by the reloading line BA, shown in Fig. 2.11. Here, the soil has been hardened by a previous wheel pass. As a consequence, in the current pass, the wheel has to first overcome the pressure required to elastically deform the soil, until the pressure reaches p_u . Therefore, the normal stress increases rapidly at the beginning on the reloading curve

BA, and then continues increasing more slowly, once p_u is reached. At this point, the soil has transitioned into a plastic state represented by the curve AC, shown in Fig. 2.11, which has a smaller slope. As a result of the plastic deformation, the soil is hardened to another level during this wheel pass. It should be noted that, if the normal stress applied by the wheel does not overcome p_u , the soil only deforms elastically, which leads to no further hardening in the current wheel pass.

When θ varies from θ_M to θ_2 , the stress decreases so that the stress profile forms the scaled symmetry used in the WR and Ishigami et al. (2007) models mentioned above.

2.5 Summary and Conclusions

In this chapter, a new framework was developed for efficient implementation of semiempirical terramechanics relations in multibody dynamics environments. In the proposed framework, a viscoelastic-like response combined with a unilateral contact model is introduced to incorporate the reaction force F_z in the direction normal to the terrain. Furthermore, the traction force F_t , resistance moment T_r , resistance force R_c , and the lateral force F_l are included in the model by modelling them as set-valued force representations with their complementary kinematic variables. As shown in this chapter, the dynamics equations of the multibody system with these representations of terramechanics relations led to a linear complementarity problem.

In addition, in our implementation, the terrain is represented as a high resolution height-field data structure. To deal with motion on rough terrain, we developed an efficient scheme in approximating the contact area using a least-squares technique. Furthermore, wheel-induced soil deformation and hardening is captured in our model, by which the multi-pass effect is included.

CHAPTER 3

An Alternative Model Based on Elasto-Plasticity Theory

3.1 Introduction

A novel approach in analyzing the interaction between a wheel and soft soil is introduced in this chapter. In this approach, normal and shear stress distributions in the contact area are determined using continuum mechanics without resorting to finite element discretization, which led to a computationally efficient technique. A velocity field in the vicinity of the contact area is proposed, which is motivated by the physical nature of the problem. Using this field, the incremental changes to the stress field are computed by resorting to elasto-plasticity theory and an appropriate constitutive relation for soil. As opposed to classical finite element approaches, which model the soil in contact with the wheel as a high-resolution mesh, our approach focuses on the wheel-soil contact patch only. This highly localized simulation scheme provides the basis for fast wheel-soil interaction modelling. By combining this approach with a height-field as terrain representation, elasto-plastic soil deformation and changes in the hardening state of soil are directly captured.

The procedure for computing soil reactions in the contact area is explained in Section 3.2. In this section, the computation of stress-increment tensor for a single point in the contact area is explained first in Section 3.2.1. This involves: (*i*) proposing a velocity field and obtaining the strain-increment tensor for it; (*ii*) using an elasto-plastic constitutive relation for soil, which is the Drucker-Prager with cap hardening in this thesis; and (*iii*) using an iterative procedure from the classical elasto-plasticity theory for decomposing the strain-increment tensor to the elastic and plastic parts. In Section 3.2.2, the determination of the stress tensor in the entire contact area is explained. The elastic rebound computation is then discussed in Section 3.2.3.

Simulation results are discussed in Section 3.3. In this section, the results of the proposed approach in steady-state operations are first compared with the results obtained from the Bekker and the Wong and Reece (1967a) models, where the latter is referred to as WR model. The simulation results of non-steady motion with variable slippage are discussed in Section 3.3.2. The slip-sinkage phenomenon captured in the novel model is discussed in Section 3.3.3. A discussion on the proposed velocity field is the focus of Section 3.3.4. Validation with experimental results available in the literature, which are obtained from a single-wheel testbed, are explained in Section 3.4, followed by integration in the multibody dynamics environment, *Vortex*, in Section 3.5. Further discussion and comparison with semi-empirical models and their behaviour regarding multi-pass is presented in Section 3.7.

The research work discussed in this chapter was reported in (Azimi et al., 2011c,b, 2013b).

3.2 Soil Reaction Estimation Using Elasto-Plasticity

Assume that a rigid wheel, under planar motion, is in contact with homogeneous soft soil. In order to find soil reactions, the calculation or estimation of the normal and shear

stress distributions around the wheel are required. Then, from Eqs. (1.7–1.10), soil reactions will be calculated. A novel approach is developed in this section based on elastoplasticity theory to calculate σ_n and τ in the contact area. The proposed approach comprises two stages: first, we explain how, for any point in the contact area, the change in the stress tensor $\Delta \sigma$ caused by wheel motion is determined; then, the stress field in the entire contact area is computed, using the algorithms introduced below.

3.2.1 Computation of the Stress-increment Tensor

Let us consider that at a point (in the soil) close to the wheel surface, the stress tensor σ and the current strain tensor ε are known. In addition, the elastic ε^e and plastic ε^p parts of the strain tensor are also known. Given the state of the rigid wheel, we look for the $\Delta \sigma$ developed in a *small* time-interval Δt . The main issue is the determination of the strain increment tensor $\Delta \varepsilon$, which is done here by assuming a velocity field at the region near the contact area. The assumed velocity field and the determination of $\Delta \varepsilon$ are explained in this section.

Using elasto-plasticity theory and a suitable constitutive relation for soil, the elastic and plastic parts of the strain increment, $\Delta \boldsymbol{\varepsilon}^e$ and $\Delta \boldsymbol{\varepsilon}^p$, are calculated based on an iterative procedure for finding a plastic multiplier (de Souza Neto et al., 2008). Further details are available in Appendices A and B.

REMARK 5. As mentioned by Khan and Huang (1995), the constitutive equations for plastic deformation should be formulated in incremental form because of path dependence in plastic deformation. \square

As previously indicated, any elasto-plastic constitutive relation can be used in our proposed approach to represent the soil response. In this thesis, the Drucker-Prager model with cap hardening is used to express the plastic behaviour of soil. In order to have a complete elasto-plastic constitutive relation, an elastic model needs to be adopted as well, for which a linearly elastic relation has been used here. For the plastic behaviour, yield surfaces and

flow potentials should be described with any hardening or softening rule. These are explained in detail in (SIMULIA, 2010) and (Helwany, 2007); a brief explanation is included in Appendix A.

3.2.1.1 *The Assumed Velocity Field*

By assuming that the friction coefficient between the wheel and the soil surfaces is higher than the internal friction coefficient of soil, any slippage happens between soil particles, not between wheel surface and soil. Therefore, the velocity of any soil particle in contact with the wheel circumference is equal to the velocity of the corresponding point on the wheel surface. Under these conditions, the soil velocity field near the contact surface is assumed to have the form

$$v_r(r,\theta) = (v_x \sin \theta - v_z \cos \theta) \exp \left[-\frac{\alpha_1}{\varepsilon_{\text{vol}}^p + \alpha_2} (r - R) \right]$$
 (3.1)

$$v_{\theta}(r,\theta) = (v_x \cos \theta + v_z \sin \theta - r\omega) \exp\left[-\alpha_3(r-R)\right]$$
 (3.2)

where polar coordinates r and θ are used to uniquely define the location of any point in the soil with respect to the wheel centre, while v_x , v_z , and ω are the generalized velocities of the wheel in planar motion, as shown in Fig. 3.1. In addition, (r-R) indicates the depth in the radial direction measured from the wheel surface, α_1 , α_2 , and α_3 being constant positive scalars, and $\varepsilon_{\text{vol}}^p$ the volumetric part of the plastic strain tensor. It is noted that the velocity field defined in Eqs. (3.1–3.2) is valid for $r \geq R$ and $\theta_2 \leq \theta \leq \theta_1$.

REMARK 6. By assuming the presence of small narrow grousers on the wheel surface, slippage will happen only among soil particles. This assumption tallies with the presence of high friction between wheel surface and soil. \Box

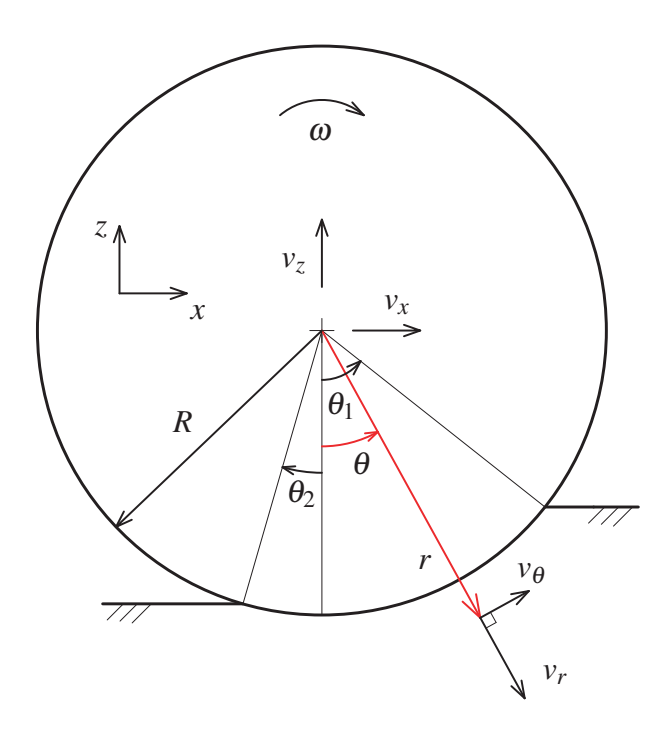


FIGURE 3.1. The r- θ directions in which the soil-particle velocity is decomposed

The assumed velocity field is in agreement with the boundary conditions of the problem, i.e., at r = R soil particle velocity is equal to that of the contact point on the wheel, while the velocity approaches zero as $r \to \infty$. It is also noted that the motion of a soil particle under the wheel is a phenomenon of diffusion, as opposed to propagation; thus the exponential decaying terms in the velocity field are consistent with this behaviour. In addition, as discussed below, the velocity field is only used in the vicinity of the wheel surface, as the only use of the velocity field in our approach is to determine the velocity gradient in the contact area. The assumed velocity field is in agreement with the experimental observations reported in the literature (Senatore et al., 2012), (Skonieczny et al., 2012), where the motion of soil particles under the wheel is recorded using high speed cameras; the velocity field is then visualized from post-processing of the recorded images.

By using the above-mentioned Drucker-Prager model for soil, the model predicts either elastic deformation or elasto-plastic deformation with hardening or softening for soil, all depending on the state of stress. If the stress in the p-q plane lies in the cap region F_c ,

shown in Fig. A.2, the soil shows compaction; otherwise dilation. In addition, p and q are the stress invariants defined in Appendix A.

Moreover, when the soil is loose, which means a small $\varepsilon_{\text{vol}}^p$, a surface-applied penetration, by a rigid wheel surface for example, will mainly cause some compaction on the soil under the wheel, but will not cause considerable soil flow to the sides. However, the same penetration on the same soil but with a higher density could result in soil-particle motion to the sides. This means that the soil with higher initial density will become less compacted when facing the same motion on its surface. This behaviour is captured to some extent by including $\varepsilon_{\text{vol}}^p$ in the velocity field and the model parameter α_2 . More discussion on the assumed velocity field is included in Section 3.3.4.

REMARK 7. The proposed velocity field is compatible with the above-mentioned constitutive relation used for soil, as the hardening/softening pattern of soil is fully identified by ε_{vol}^p , which is a key parameter in the velocity field. \square

Then, the velocity gradient tensor at $r = R^+$, on the external wheel periphery¹, is determined as

$$\mathbf{G}_{r\theta}(R^{+},\theta) = \begin{bmatrix} -\frac{\alpha_{1}}{\varepsilon_{\text{vol}}^{p} + \alpha_{2}} v_{r}(R,\theta) & \omega \\ -\alpha_{3}v_{\theta}(R,\theta) - \omega & 0 \end{bmatrix},$$
(3.3)

where $v_r(R, \theta)$ and $v_{\theta}(R, \theta)$ are the radial and tangential velocity components at the wheel surface at location θ and are obtained from Eqs. (3.1) and (3.2), respectively.

Introducing the rotation matrix

$$\mathbf{R} = \begin{bmatrix} \sin \theta & \cos \theta \\ -\cos \theta & \sin \theta \end{bmatrix},\tag{3.4}$$

 $^{{}^{1}}R^{+}$ indicates the value of r when r approaches R from "the right", as the function whose argument is r is not defined at R^{-} .

the velocity gradient tensor $G_{r\theta}$ can be transformed into the fixed coordinate system (*x-z*) via a similarity transformation:

$$\mathbf{G}_{xz} = \mathbf{R}\mathbf{G}_{r\theta}\mathbf{R}^T \tag{3.5}$$

where G_{xz} is the velocity gradient tensor in the *x-z* system. Then, the time-derivative $\dot{\boldsymbol{\varepsilon}}$ of the infinitesimal strain tensor can be obtained as the symmetric part of the velocity gradient:

$$\dot{\boldsymbol{\varepsilon}} = \frac{1}{2} (\mathbf{G}_{xz} + \mathbf{G}_{xz}^T) \tag{3.6}$$

The strain increment is then obtained as:

$$\Delta \boldsymbol{\varepsilon} = \dot{\boldsymbol{\varepsilon}} \Delta t \tag{3.7}$$

3.2.2 Determination of the Stress Tensor in the Contact Area

The procedure for obtaining soil reactions is explained in the two algorithms below. In Algorithm 1, it is assumed that the rigid wheel is in steady-state condition, similar to the Bekker and WR models, and moves with a nonzero angular velocity, while in Algorithm 2, the general motion is considered. Algorithm 1 is straightforward for implementation, compared to Algorithm 2, and is useful for parameter-tuning and comparison with the Bekker and WR models, as explained in Section 3.3.4. Algorithm 2, however, is applicable to the general motion of the wheel, as explained further below.

In Algorithm 1, the normal and shear stress distributions in the contact area are obtained by following the motion of a single point on the wheel periphery from its initial contact with soil ($\theta = \theta_1$) until separation ($\theta = \theta_2$ in Fig. 3.1). During this motion, at any location of this point identified by the angle θ , shear and normal stresses are obtained. As the wheel moves under steady-state conditions, the stress values should not change in time at any contact angle θ . Therefore, the calculated stress distributions, obtained by following

the motion of the point mentioned above, represent the stress distributions under the wheel.

ALGORITHM 1.

Assumptions:

- The rigid wheel operates under steady-state conditions. This means that the velocity component v_z is zero. Also, the stress field in the contact area should not change in time.
- The pre-compaction level and the initial stress level of soil before contacting with the wheel are known. Therefore, the stress and strain tensors are known at the initial contact point $\theta = \theta_1$ in Fig. 3.1.
- A high friction coefficient exists between wheel surface and soil, as explained earlier and in Remark 6.

Steps:

- (i) At the initial contact point, $\theta = \theta_1$ in Fig. 1.1, initialize σ and ε from the initial compaction data of soil. Then, choose a small Δt for integration, set $\Delta \theta = \omega \Delta t$, and go to Step 5.
- (ii) Update $\theta = \theta_p \Delta \theta$.
- (iii) From Eqs. (3.1–3.7), calculate $\Delta \mathbf{\varepsilon}$ associated with the motion during $\Delta \theta$.
- (iv) Using plasticity theory, $\Delta \boldsymbol{\varepsilon}^e$ and $\Delta \boldsymbol{\varepsilon}^p$ are determined (see Appendix B), which leads to the computation of $\boldsymbol{\sigma}$, $\boldsymbol{\varepsilon}^e$, and $\boldsymbol{\varepsilon}^p$ at the current location on the wheel (with angle θ). Then, express the stress tensor in the r- θ directions to obtain $\sigma_n(\theta)$ and $\tau(\theta)$.
- (v) Set $\theta_p = \theta$. If $\theta > 0$, go to Step (ii); else, go to Step (vi).
- (vi) If $\sigma_n(\theta) \leq 0$, go to Step (viii); else, soil particle is in the elastic rebound condition. Follow the steps in Algorithm 3 to find σ and $\Delta \varepsilon^e$. Note that in this case $\Delta \varepsilon^p = 0$.

- (vii) Express the stress tensor $\boldsymbol{\sigma}$ in the r- θ directions to obtain $\sigma_n(\theta)$ and $\tau(\theta)$. Then, go to Step (vi).
- (viii) Use Eqs. (1.7–1.10) to obtain soil reactions. ■

REMARK 8. By default, elastic rebound of soil is included in Algorithm 1 in steps 6 and 7. Omitting these steps means neglecting the elastic rebound of soil. \square

The algorithm below outlines the procedure involved in this novel approach, for the dynamic motion of a rigid wheel in planar motion. In this algorithm, an explicit integration scheme is used to obtain the updated normal and shear stress distributions under the wheel, based on the motion of the wheel and hardening state of the soil. Here, the stress values are obtained at some *mesh points* on the contact region of the wheel and soil (Fig. 3.2).

ALGORITHM 2.

Assumptions:

- The pre-compaction level and the initial stress level of soil before contact with the wheel are known.
- A high friction coefficient exists between wheel surface and soil, as explained earlier and in Remark 6.

Steps:

- (i) Determine some mesh points on the periphery of the wheel by creating a surface mesh on the wheel periphery. The nodes of this mesh are the mesh points used in this algorithm (see Fig. 3.2).
- (ii) Determine the mesh points that are in contact with the terrain (referred to as active points). The values of stress and strain at active points that have not been in contact with the terrain in the previous time-step will be initialized from the initial stress and strain of soil.

CHAPTER 3. AN ALTERNATIVE MODEL BASED ON ELASTO-PLASTICITY THEORY

- (iii) For a given time-step and for each active point, the steps below are followed. It should be noted that for each active point, the current stress and strain tensors are known at time t.
 - (a) Define the loading condition: loading or unloading:
 - (i) Compute v'_z as

$$v_z' = \mathbf{v}_{\text{mesh}} \cdot \mathbf{n}_{\text{terrain}} \tag{3.8}$$

where \mathbf{v}_{mesh} is the velocity vector of the active point and $\mathbf{n}_{terrain}$ is the normal direction of the terrain².

- (ii) If $v'_z > 0$, the active mesh point is in the rebound³; go to Step (iii-d). Otherwise, the point is in a loading condition; go to Step (iii-b).
- (b) $\Delta \varepsilon$ is calculated from Eqs. (3.1–3.7).
- (c) Using elasto-plasticity theory, $\Delta \boldsymbol{\varepsilon}^e$ and $\Delta \boldsymbol{\varepsilon}^p$ are determined (see Appendix B), which leads to the updated stress tensor $\boldsymbol{\sigma}(t+\Delta t)$ and updated strain tensors $\boldsymbol{\varepsilon}^e(t+\Delta t)$ and $\boldsymbol{\varepsilon}^p(t+\Delta t)$. Then, go to Step (iv).
- (d) Elastic rebound condition: follow the steps in Algorithm 3 to find the updated stress tensor $\boldsymbol{\sigma}(t+\Delta t)$ and updated strain tensor $\boldsymbol{\varepsilon}^e(t+\Delta t)$, while $\boldsymbol{\varepsilon}^p$ remains unchanged.
- (iv) Express the updated stress tensor of all active points in the r- θ directions to obtain σ and τ . Integration of σ and τ over the area of wheel surface covered by the active points will result in the reaction forces of soil.
- (v) Increment time in simulation with the reaction forces obtained in the previous step. Set $t \leftarrow t + \Delta t$ and go to Step (ii).

²The computation of $\mathbf{n}_{\text{terrain}}$ is explained in Section 3.5 when operating on an irregular terrain.

³For numerical stability reasons, in our implementation instead of zero, we compare v_z' with a small positive scalar ε' to start our elastic rebound phase. When $0 \le v_z' \le \varepsilon'$, soil will show rebound with softening.

REMARK 9. $\Delta \boldsymbol{\varepsilon}$ should be small enough to ensure the convergence of the numerical procedure involved in obtaining $\Delta \boldsymbol{\varepsilon}^e$ and $\Delta \boldsymbol{\varepsilon}^p$, in Step (iii); the required time-step for the $\Delta \boldsymbol{\varepsilon}$ calculation is usually much smaller than the time-step of the multibody system simulation. In this case, Step (iii) is conducted multiple times under smaller increments to ensure the convergence of the $\Delta \boldsymbol{\varepsilon}^e$ and $\Delta \boldsymbol{\varepsilon}^p$ calculations. \square

REMARK 10. Having a large number of mesh points will increase the computation time; however, the algorithm is highly parallelizable as each mesh point can be treated independent of the other points in this algorithm. It should be noted that using a very small number of mesh points can cause non-negligible discretization error, which may result in noticeable oscillations.

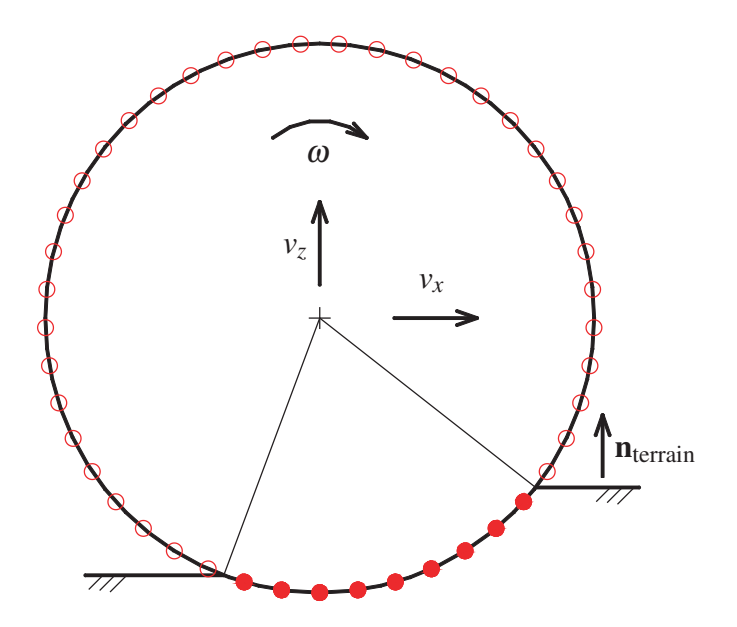


FIGURE 3.2. Mesh points in a 2D case for a cylindrical wheel. Solid circles are active mesh points.

3.2.3 Elastic Rebound Computation

In wheel and soil interaction, soil rebound happens when the wheel surface starts to separate from soil instead of pushing it. Therefore, in this stage pressure between soil particles decreases, which causes reduction in both normal and shear stresses. In our model,

CHAPTER 3. AN ALTERNATIVE MODEL BASED ON ELASTO-PLASTICITY THEORY

during elastic rebound, normal and shear stresses decrease such that the hardening state of soil does not change (due to a purely elastic rebound assumption).

The assumed velocity field expressed in Eqs. (3.1) and (3.2) is valid for the region undergoing no rebound, because there it is assumed that the soil particle in the wheel surface follows the velocity of the wheel surface. However, if the soil particle at the wheel surface is in a rebound condition, then it cannot follow the wheel surface, because it cannot be pulled by the wheel, where negligible adhesion between wheel surface and soil is assumed. We can, however, assume that in the radial direction, the soil particle follows the motion of the wheel surface until the contact pressure between wheel and soil reaches zero. After that, separation between wheel surface and the soil particle happens. During this rebound phase, the shear strain is adjusted in our algorithm such that the state of stress remains inside or on the yield surface (state of stress outside the yield surface is invalid), while the hardening of soil does not change. To this end, the procedure below is introduced for any point that is in the elastic rebound phase. It is noted that the condition for a soil particle to be in the elastic rebound phase was explained in Algorithms 1 and 2.

ALGORITHM 3.

Given the current stress tensor σ , strain tensors $\boldsymbol{\varepsilon}^e$ and $\boldsymbol{\varepsilon}^p$, wheel geometry and state variables, and knowing that the soil particle is experiencing elastic rebound, compute updated stress and strain tensors after a small time-step Δt .

Steps:

(i) Compute $\Delta \boldsymbol{\varepsilon}$ from Eq. (3.7) and initialize the elastic and plastic parts of the strain increment tensor by

$$\Delta \boldsymbol{\varepsilon}_{\text{trial}}^{e} = \Delta \boldsymbol{\varepsilon} \tag{3.9a}$$

$$\Delta \boldsymbol{\varepsilon}^p = \mathbf{0} \tag{3.9b}$$

(ii) Introduce a trial stress state, which has the form below for a linearly elastic behaviour:

$$\boldsymbol{\sigma}_{\text{trial}} = \boldsymbol{\sigma} + \mathbf{C} : \Delta \boldsymbol{\varepsilon}_{trial}^{e} \tag{3.10}$$

where C is the fourth-rank elastic stiffness tensor. Symbol ":" denotes double contraction, as needed between a fourth-rank tensor C and a second-rank tensor $\boldsymbol{\varepsilon}_{\text{trial}}^{e}$ (de Souza Neto et al., 2008), to produce a second-rank stress tensor.

- (iii) Check the validity of σ_{trial} . If it is inside or on the yield surface, go to Step (v), as σ_{trial} is a valid stress tensor (de Souza Neto et al., 2008); otherwise, go to Step (iv).
- (iv) Modify $\Delta \boldsymbol{\varepsilon}_{\text{trial}}^{e}$: This is done by modifying the lower off-diagonal element of $\mathbf{G}_{r,\theta}(R^{+},\theta)$ in Eq. (3.3), referred to as $\mathbf{G}_{r,\theta}(2,1)$, by the relation below:

$$\mathbf{G}_{r,\theta}(2,1) = -\alpha_3 v_{\theta}(R,\theta)(1-\eta) - \omega \tag{3.11}$$

where η is a positive scalar. Here we increase η stepwise from zero until the condition in Step (iii) is satisfied on σ_{trial} . The updated $\Delta \boldsymbol{\varepsilon}_{trial}^e$ is computed from Eqs. (3.1–3.7) and using Eq. (3.11). It is noted that, by using this modified strain increment tensor in the elastic rebound phase, the state of stress remains valid, while the hardening state of soil does not change. This is the necessary condition for a purely elastic rebound. After incrementing η and computing $\Delta \boldsymbol{\varepsilon}_{trial}^e$, go to Step (ii)⁴.

(v) Set $\sigma = \sigma_{\text{trial}}$ and exit.

⁴Instead of increasing η stepwise, a more computationally efficient approach would be formulating a single-variable optimization problem, basically a line search, to find the appropriate η .

3.3 Simulation Results and Further Analysis

To validate the proposed approach, our results are compared with those obtained using the Bekker and WR models. As mentioned above, the Drucker-Prager constitutive relation with cap hardening is used to model the plastic deformation of soil in this thesis. Combined with a linear elasticity model, this relation leads to an elasto-plastic constitutive relation for soil. However, the nature of the Bekker and WR models being different from this elasto-plastic constitutive relation, they have different sets of parameters. The parameters of the elasto-plastic constitutive relation are listed in Tables 3.1 and 3.2; some of these parameters are taken from (Chiroux et al., 2005).

REMARK 11. It is noted that the approach proposed in this thesis does not depend on a specific constitutive relation for soil or a specific form of the velocity field. Soil constitutive relation and the assumed velocity field are important elements of the approach, but other pertinent constitutive relations and velocity fields can also be employed. \square

The parameters needed for the Bekker and WR models are k_c , k_ϕ , n, ϕ , c, and K_d . Here we need to find the equivalent set of parameters needed for these models based on the parameters of the elasto-plastic constitutive relation listed in Tables 3.1 and 3.2. To do so, we simulated the plate-penetration test (bevameter test) using Abaqus to identify k_c , k_ϕ , and n, as explained below. In addition, ϕ and c are defined from the parameters of the Drucker-Prager model (β and d) using the relations below (Shoop, 2001), by "assuming plane strain response and non-dilatant flow" (Shoop, 2001):

$$\tan \beta = 1.73 \sin \phi, \quad d = 1.73 c \cos \phi \tag{3.12}$$

Furthermore, an average value for K_d was chosen based on values reported in the terramechanics literature⁵. Moreover, for the WR model two other parameters, c_1 and c_2 , are

⁵A more appropriate way for defining ϕ , c, and K_d is simulating the bevameter shear test in Abaqus, which should result in more accurate calculation of shear stress distribution.

needed to locate the position of the maximum radial stress. These parameters are also selected from p. 386 of (Wong, 2010) for loose sand; their values are listed in Table 3.3.

TABLE 3.1. Material properties for the elasto-plastic constitutive relation

Young's modulus, E (Pa)	3×10^6
Poisson's ratio, v (-)	0.32
Angle of friction, β (deg)	41
Material cohesion, d (Pa)	350
Cap eccentricity, R_e (-)	0.15
Initial value for $\varepsilon_{\mathrm{vol}}^{p}$ (-)	0.001
Transition surface parameter, α (-)	0.01

TABLE 3.2. The hardening pattern used in the elasto-plastic constitutive relation

p_b (kPa)	$arepsilon_{\mathrm{vol}}^p$	p_b (kPa)	$arepsilon_{\mathrm{vol}}^p$
0.15	0	24	0.149679
1.5	0.014661	27	0.160028
3	0.028334	30	0.16928
6	0.053024	36	0.185036
9	0.074619	48	0.208422
12	0.093572	63	0.228045
15	0.110262	87	0.248232
18	0.125006	120	0.266976
21	0.138069	150	0.280999

TABLE 3.3. Parameters of the Bekker and WR models used for comparison

φ (deg)	30
c (Pa)	234
$k_{\phi} (N/m^{(n+2)})$	4.104×10^5
$k_c \left(N/m^{(n+1)} \right)$	0
n (-)	0.8
K_d (m)	0.013
<i>c</i> ₁ (-)	0.18
c ₂ (-)	0.32

As mentioned above, the plate-penetration test (bevameter test) is simulated using Abaqus to identify k_c , k_ϕ , and n. For this, 2D simulation runs were conducted on Abaqus/Explicit with plate widths of 100 mm and 120 mm. The von Mises stress distribution under the plate

CHAPTER 3. AN ALTERNATIVE MODEL BASED ON ELASTO-PLASTICITY THEORY

is shown in Fig. 3.3. It should be noted that only one half of the plate and soil mass is simulated, as the problem has a plane of symmetry. The average pressure developed under the plate is plotted in Fig. 3.4 versus plate sinkage for both plate sizes. From that figure, k_c , k_{ϕ} , and n are identified.

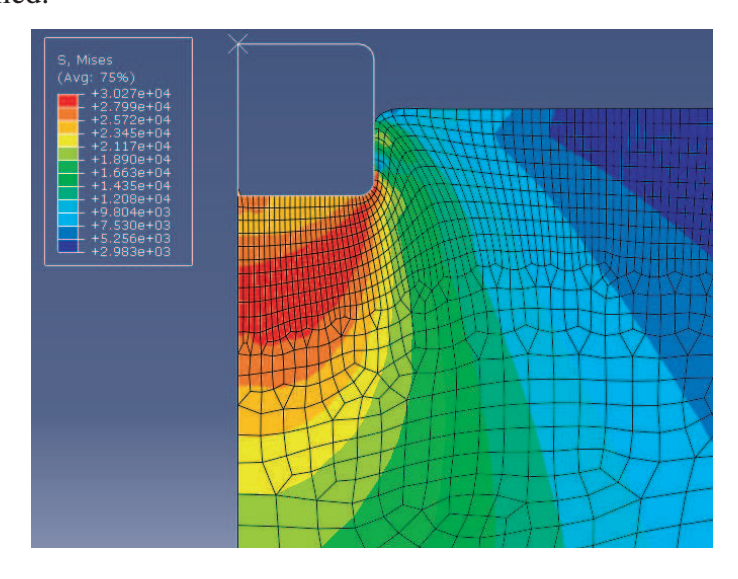


FIGURE 3.3. Von Mises stress distribution under the plate in the penetration test with a plate width of $0.1\ m$

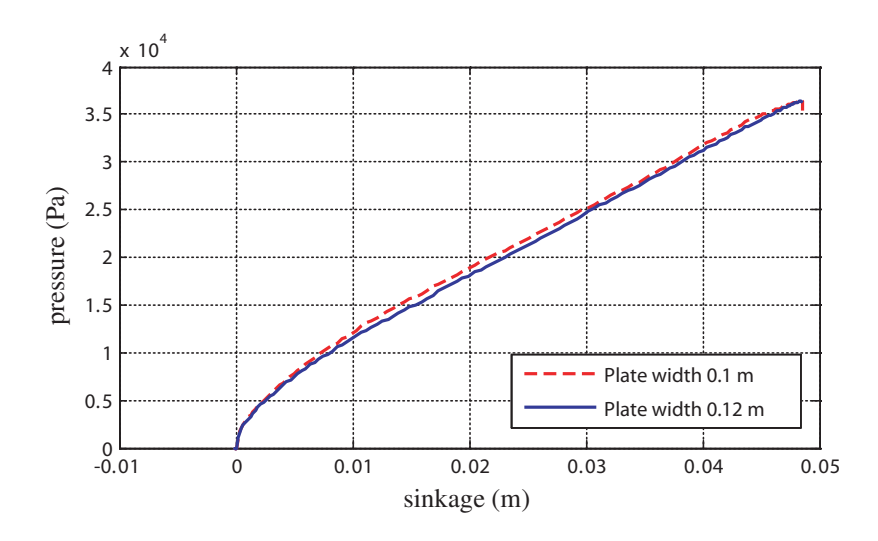


FIGURE 3.4. Average pressure developed under the plates vs. plate sinkage using Abaqus Explicit

In the remainder of this section, an example of steady-state motion for a single wheel is analyzed, followed by non-steady motion of the same wheel in the second example. Then, the slip-sinkage behaviour is investigated. An explanation of the assumed velocity-field parameters and general discussion are the topics of the last two subsections.

3.3.1 Steady-state Motion

In this case, a rigid cylindrical wheel with 0.30 m diameter and 0.10 m width moves under steady-state conditions, which means a constant v_x and ω and a zero v_z . v_x is 0.12 m/s and ω is 1.0 rad/s, which results in a 20% slip ratio. This example is repeated for different values of vertical load, ranging from 39 N to 206 N. Soil reactions are compared with the Bekker and the WR models. The parameters of the proposed velocity field, which were tuned based on an approach explained in Section 3.3.4, are listed in Table 3.4. It should be mentioned that in the results displayed in Figs. 3.5–3.9 we have adopted a zero exit angle ($\theta_2 = 0$) by assuming that the elastic rebound of soil is negligible. As $\theta_2 = 0$ is also assumed in the Bekker and WR models, this assumption helps us do a fair comparison between the basic elements of our model and the aforementioned Bekker and WR models. After that, all the results are obtained while considering the elastic rebound of soil.

TABLE 3.4. Parameters of the proposed velocity field

$\alpha_1 (\mathrm{m}^{-1})$	α_2 (-)	$\alpha_3 (\mathrm{m}^{-1})$
0.64	0.03	35

By comparing the results of the drawbar pull and the resistance force, Figs. 3.5 and 3.6, the estimated resistance force closely matches the ones resulting from the Bekker and WR models; however, the traction force is overestimated at low and underestimated at high sinkage values, when compared with these models. In addition, as shown in Fig. 3.7, the estimated wheel sinkage matches the Bekker and WR models relatively well, under various loadings and a fixed 20% slip ratio.

Furthermore, the normal and shear stress distributions are displayed in Figs. 3.8 and 3.9. The normal stress distribution is closer to the Bekker model, but shows that the position of maximum normal stress is shifted forward, which agrees with experimental evidence (Wong, 2010). It is noteworthy that the normal stress distribution resulting from

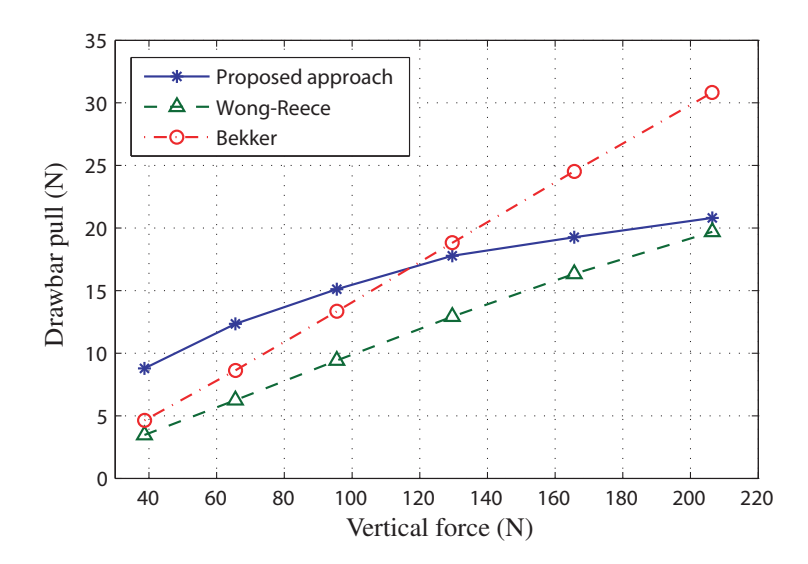


FIGURE 3.5. Comparison of the calculated drawbar pull for 20% slip ratio under the action of different vertical loads

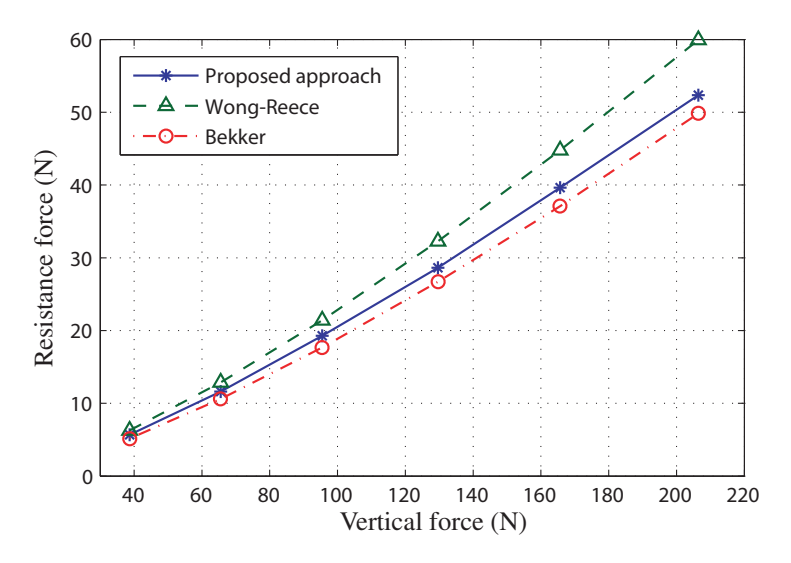


FIGURE 3.6. Comparison of the calculated resistance force for 20% slip ratio under the action of different vertical loads

the proposed approach is in good agreement with these models. The shear stress, however, is overestimated at the area closer to the entry point and underestimated towards the bottom-dead-centre. This can be related to a shortcoming of the adopted constitutive relation, which can represent the compaction process relatively well but overestimates the

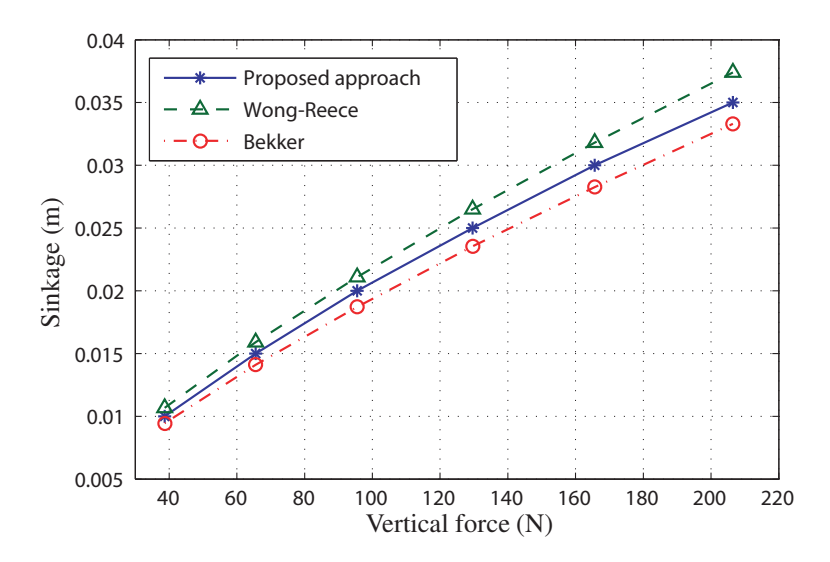


FIGURE 3.7. Comparison of the resulting sinkage for 20% slip ratio under the action of different vertical loads

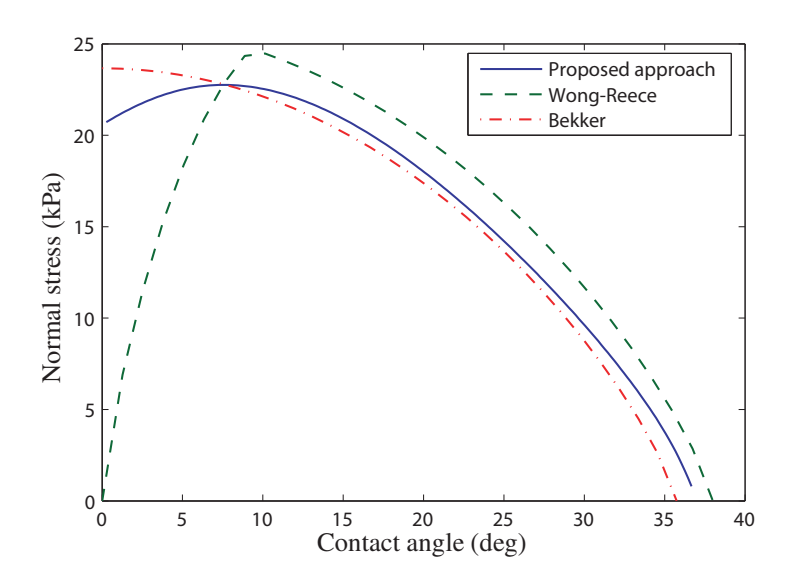


FIGURE 3.8. Normal stress distribution for 20% slip ratio under $F_z = 165 \text{ N}$

shear stress at small shear strains. This means that the proposed model with this constitutive relation can more accurately represent terrains with small K_d . It should, however, be noted that the Bekker and WR models provide an estimation for the stress distribution in the contact area; further experimental data, for stress distribution, are needed to comment more specifically on the validity of these results.

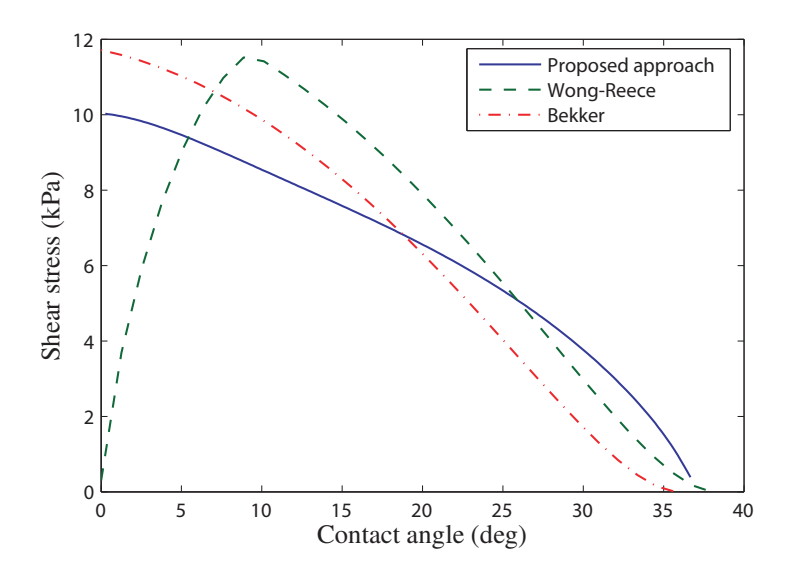


FIGURE 3.9. Shear stress distribution for 20% slip ratio under $F_z = 165 \text{ N}$

In Figs. 3.8 and 3.9, the stress values are zero for negative contact angles ($\theta < 0$). It should be noted that in steady-state operations ($v_z = 0$), the radial component of the velocity vector on the wheel periphery at angle θ , $v_r(R,\theta)$, becomes negative for $\theta < 0$, and points toward the wheel centre. For this case, if we assume that the soil shows negligible elastic rebound, there will be no contact when $v_r(R,\theta) < 0$, as the wheel can only *push* the soil. Therefore, assuming zero elastic rebound when $v_z = 0$ results in $\theta_2 = 0$ and a discontinuity in the stress distribution.

This example was analyzed again while considering the rebound of soil due to its elasticity and using a relatively small Young's modulus for soil (see Young's modulus in Table 3.1). Normal and shear stress distributions are shown in Fig. 3.10. As a relatively small Young's modulus is used for soil, the rear region ($\theta_2 < \theta < 0$), corresponding to the elastic rebound, is noticeable. Increasing Young's modulus results in smaller θ_2 . As expected, the stress distributions show no discontinuity in this case.

REMARK 12. As mentioned above, the non-zero exit angle in this model is the result of the elastic rebound of soil. In practice, soil flow and grousers affect the exit angle and they

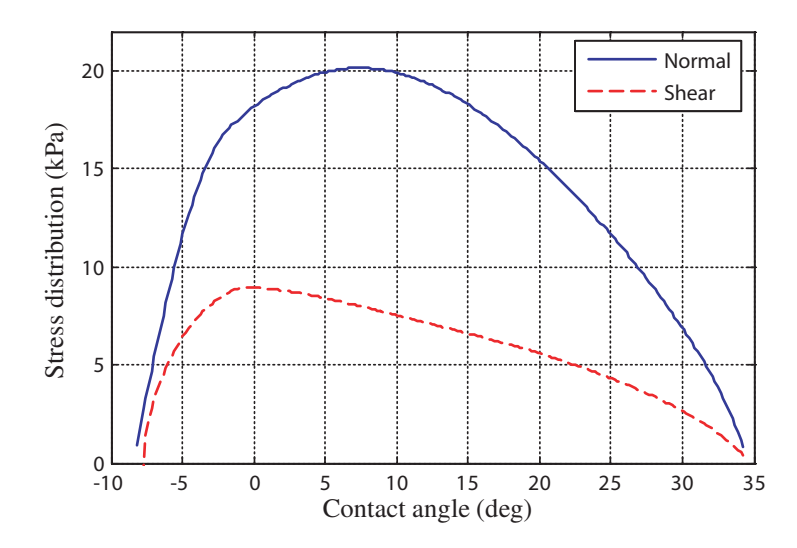


FIGURE 3.10. Normal and shear stress distributions for 20% slip ratio under $F_z = 165 \text{ N}$ using Algorithm 1 with consideration of elastic rebound of soil.

could be the dominant factors when moving on sand with relatively high slip ratio. However, when adapting a continuum model with using an elasto-plastic soil representation, the elasticity of soil (and wheel) determine the exit angle, which is an inherent limitation of elasto-plastic soil representation. It should be mentioned that the common practice in the literature is to either assume the exit angle as a function of the entrance angle, as in (Ishigami et al., 2007), or use soil and wheel elasticity, as in (AESCO, 2005).

3.3.2 Non-steady Motion and Variable Slippage

In this section, we analyze a simple but illustrative example in order to demonstrate the behaviour of our model in non-steady operations and under a wide range of wheel-slippage conditions. In this example, we investigate the planar motion of a rigid wheel on soil, in which v_x and ω are controlled to achieve certain values for the wheel slip ratio with ω measured positive cw and v_x positive to the right (Fig. 1.1). In the *z*-direction, the wheel is free to move under gravity. Mass, radius, and width of the wheel are 16 kg, 0.15 m, and 0.10 m, respectively.

The wheel is *dropped* with a zero initial velocity and an initial sinkage of 1 mm. Algorithm 2 is used to obtain the reaction forces applied on the wheel, and the elastic rebound of soil is included that leads to a non-zero exit angle for the proposed model. From t = 0 s to t = 1 s, the wheel moves in the z-direction only, due to gravity, and causes plastic deformation in soil. The wheel is then commanded to move forward with the velocity profiles shown in Fig. 3.11. With these velocity profiles, the slip ratio grows incrementally from 0 to 30%. The results obtained with our proposed approach are displayed in Figs. 3.12 and 3.13.

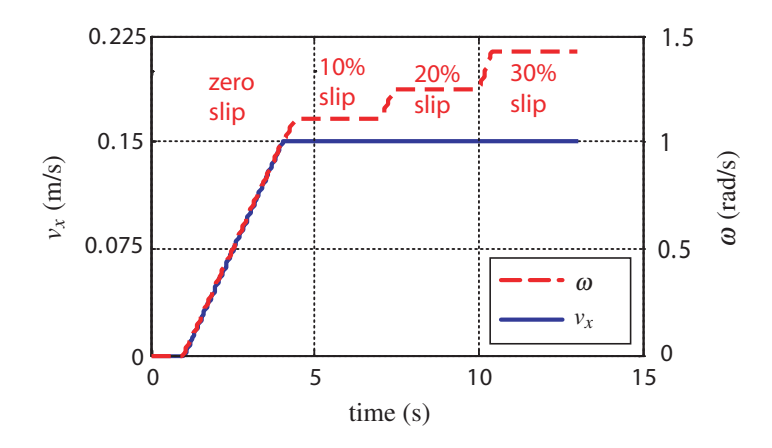


FIGURE 3.11. Command forward and angular velocities to the wheel

Again, our results are compared with those obtained based on the Bekker and WR models. However, directly using the Bekker or WR model in this example leads to an unrealistic oscillatory response in soil reactions and wheel sinkage, because energy dissipation in the *z*-direction is not considered in those models, as briefly explained in Section 2.3. Therefore, we used the modified version of these models, as proposed in Chapter 2. The results are shown in Figs. 3.14 and 3.15.

As can be seen from Fig. 3.12, using our model, wheel sinkage increases with slip ratio, which agrees qualitatively well with the experimental observations, known as slip-sinkage. In the Bekker and WR models, however, this feature is not captured. In addition, at the initial phase, when the wheel is *dropped*, it sinks with a negligible rebound when the

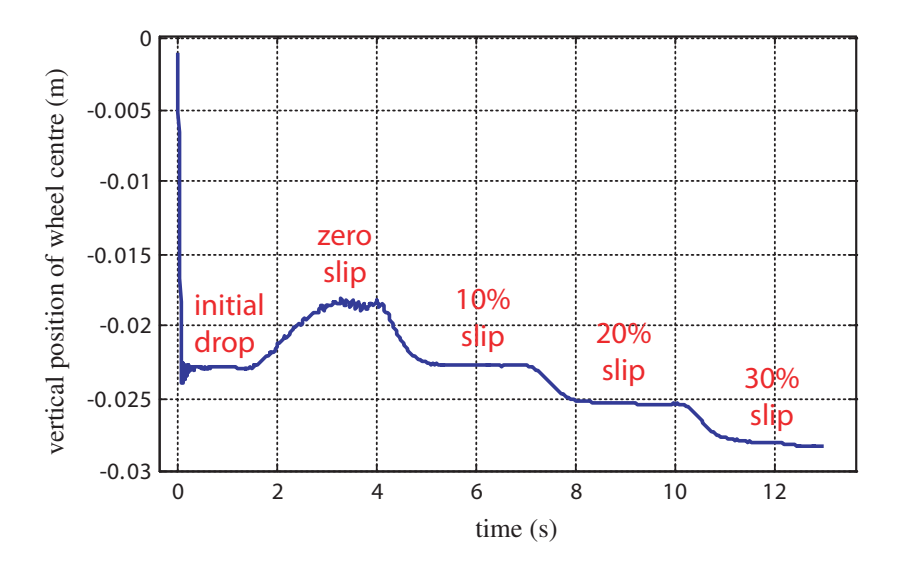


FIGURE 3.12. Vertical position of wheel centre versus time as predicted by our novel approach in modelling wheel-soil interaction

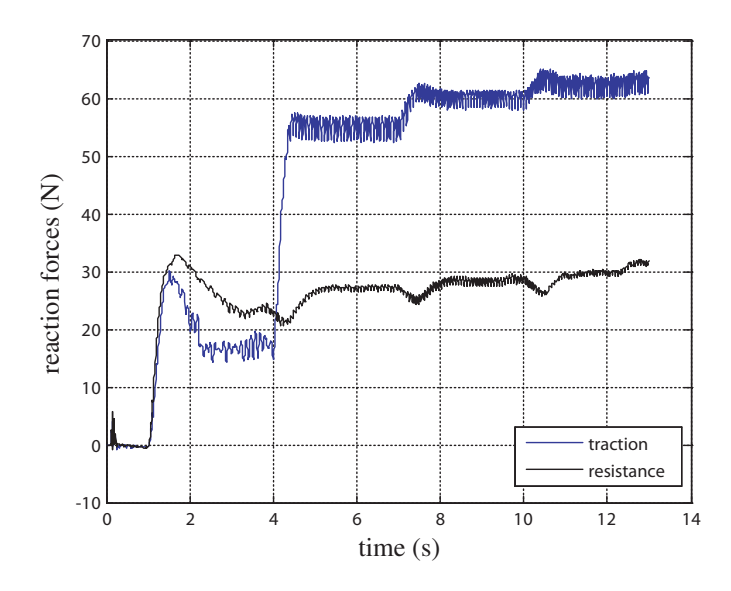


FIGURE 3.13. Wheel traction and rolling resistance as predicted by our novel approach in modelling wheel-soil interaction

proposed model is used, due to plastic deformation of soil. The wheel moves up when it starts its motion with zero slip ratio, which agrees with experimental observations.

In Fig. 3.13, the traction and resistance forces predicted by our model exhibit some oscillations from their nominal value. This is caused by the discretization error associated

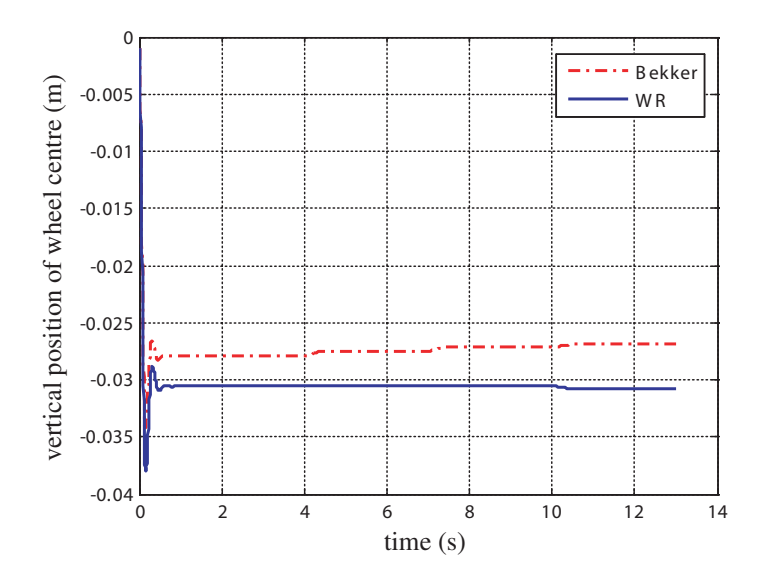


FIGURE 3.14. Vertical position of wheel centre vs. time as predicted by the modified Bekker and WR models (Azimi et al., 2011a)

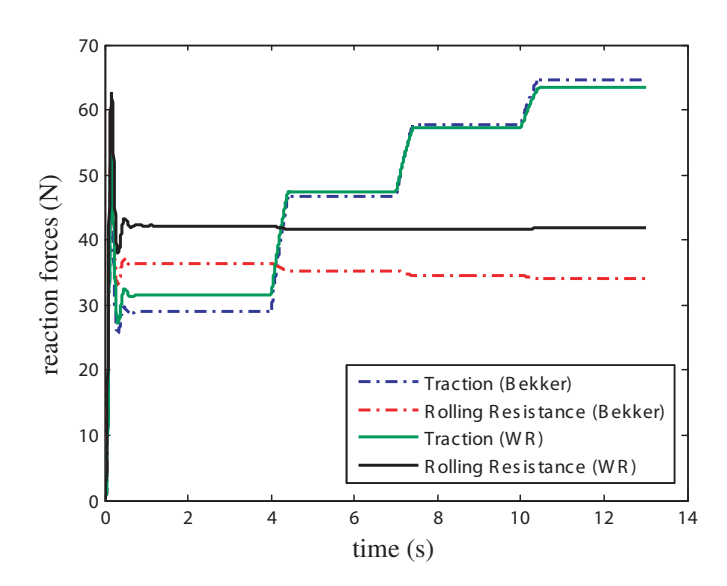


FIGURE 3.15. Wheel traction and rolling resistance as predicted by the modified Bekker and WR models explained in Chapter 2.

with the use of mesh points. Increasing the number of the mesh points results in smaller oscillation amplitudes in the reaction forces.

To better illustrate the effect of discretization, the same simulation is conducted with higher resolution for the mesh points, the results being shown in Fig. 3.16. In the results

shown in Fig. 3.15, the rigid wheel has 72 mesh points, one mesh point every 5 degrees. The results displayed in Fig. 3.16 are obtained with 180 and 360 mesh points for the wheel. As can be seen, the oscillation amplitude decreases substantially upon increasing the number of mesh points.

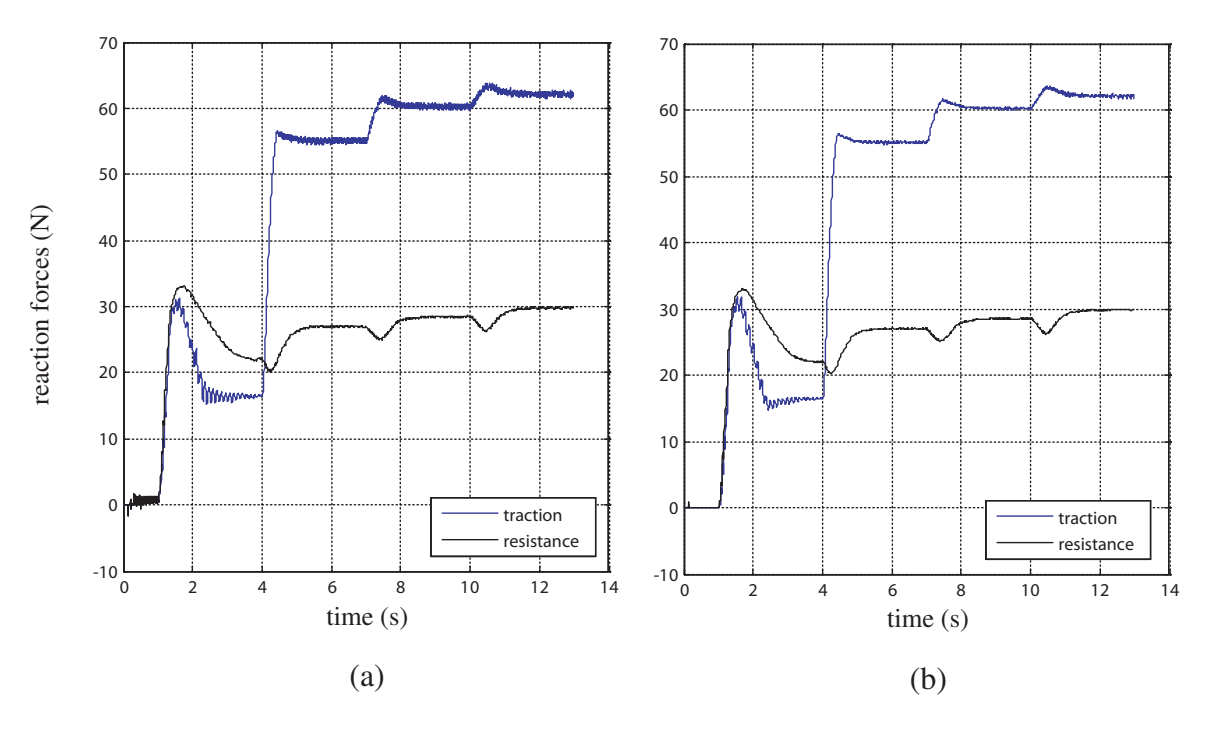


FIGURE 3.16. Wheel traction and rolling resistance as predicted by the proposed model with different mesh points on the wheel. (a) 180 mesh points; and (b) 360 mesh points.

3.3.3 Analyzing the Slip-sinkage Phenomenon

According to the WR model (Wong and Reece, 1967a), the effect of wheel slip on normal stress distribution under a rigid wheel is at the position of maximum radial stress (θ_M) , but the stress distribution from soil surface to θ_M remains independent of wheel slip and follows Bekker's pressure-sinkage relation. However, the results of our model suggest that the wheel slip affects the stress distribution in the entire contact area.

By increasing wheel slip, according to our model, soil particles at the contact area experience a higher shear deformation (in the direction tangent to the wheel surface), while receiving a lower push from the wheel in the direction normal to the wheel surface. Based on our assumed velocity field, and the Drucker-Prager constitutive relation adopted for soil, this combination leads to a strain increment tensor $\Delta \varepsilon$ with a smaller volumetric plastic part. As a result, a lower soil hardening is predicted with our model when wheel slip increases. The pressure-sinkage relations under a rolling/slipping wheel (with various slippage conditions), obtained by using our model, is displayed in Fig. 3.17. As can be seen, the pressure-sinkage relation changes in the entire contact area when the wheel slip changes. This overall behaviour is consistent with the model recently proposed by Ding et al. (2010a) regarding slip-sinkage. In their approach, they modified the sinkage exponent n as a linear function of slip ratio, in order to capture experimental observations. However, further experimental studies where stress distribution is measured at different slip ratios are necessary to fully investigate the validity of these models.

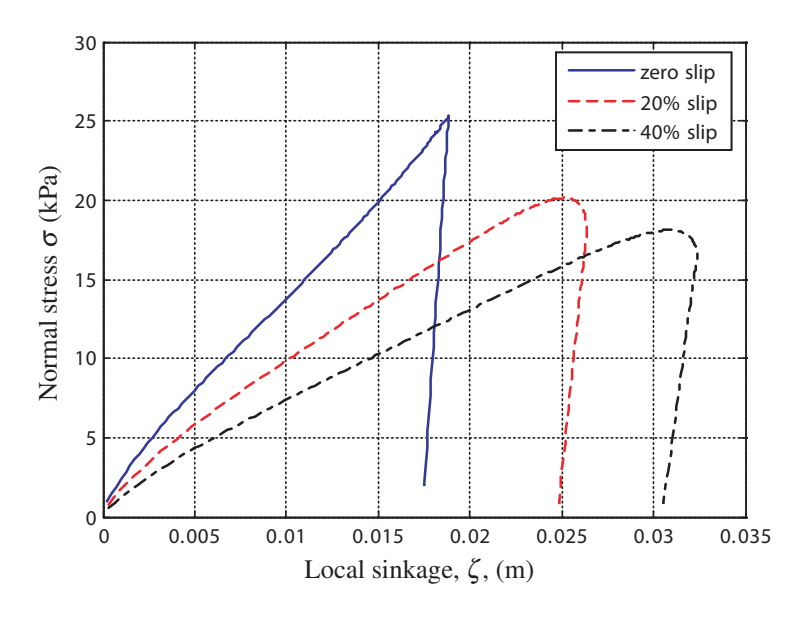


FIGURE 3.17. Normal stress under a rigid wheel versus local sinkage ζ (see Fig. 1.1 for a definition of ζ) at various slip ratios under $F_z = 165$ N, while the elastic rebound is considered.

It is also noted that during elastic rebound, normal stress decreases linearly with ζ , as a result of the linearly elastic relation used to represent the elastic behaviour of soil. Of

course, nonlinear elastic relations can also be incorporated to more accurately capture the elastic response of different types of soil.

Stress distributions at different slip ratios are displayed in Fig. 3.18 to better illustrate the situation. As can be seen from the figure, in the case of zero slip ratio, maximum normal stress occurs at the bottom-dead-centre ($\theta = 0$); however, it shifts forward by increasing wheel slip. This shift in the location of maximum normal stress is caused by soil softening⁶. For example, in the case of 20% or 40% slip ratio in Fig. 3.18, the normal stress increases from zero at $\theta = \theta_1$ to its maximum value at $\theta = \theta_M$. In this region, soil hardening is happening. From $\theta = \theta_M$ to around $\theta = 0$, soil softening happens and causes the normal stress to decrease. After that, normal and shear stresses decrease because of the elastic rebound of soil.

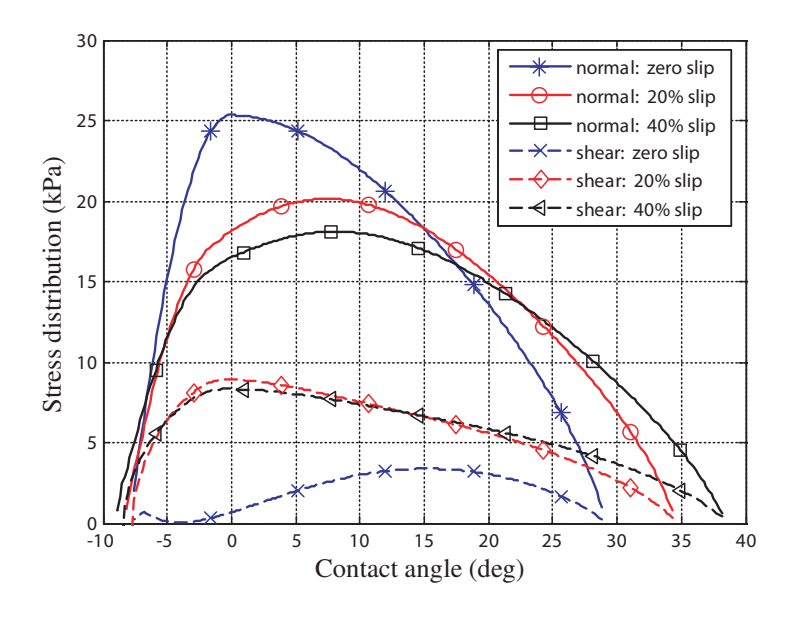


FIGURE 3.18. Normal and shear stress distributions for various slip ratios under $F_z = 165$ N using Algorithm 1, where the elastic rebound is considered.

3.3.4 Discussion on the Proposed Velocity Field and Its Parameter Selection

To better illustrate the proposed velocity field, in Fig. 3.19 trajectories of soil particles

⁶It should be noted that in the Drucker-Prager model adopted in this thesis, when a plastic deformation happens at the failure surface F_s or the transition surface F_{tr} , the deformation may cause soil softening.

initially at soil surface and 10 mm below surface are plotted at different slip ratios for a wheel diameter of 0.3 m. The trajectories are overall consistent with reported experimental observations in (Shikanai et al., 2000), (Maciejewski and Jarzebowski, 2004) and (Fukami et al., 2006). The difference lies in that soil particles initially located deeper in soil (not on the surface) tend to scape to soil surface where there is no loading, as they move along the least resistive path; this behaviour becomes more significant when soil compaction increases. What is important for our approach is the effect of this behaviour on the velocity gradient and strain tensor in soil particles very close to the contact surface. Here we have considered the effect of soil compaction by including $\varepsilon_{\text{vol}}^p$, which is the hardening/softening variable, in the velocity field.

In addition, in the proposed velocity field, it is assumed that a soil particle at the contact area has the same velocity as the adjacent point on the wheel surface. However, if the entry angle θ_1 is large, as shown in Fig. 3.20, soil particles at the beginning of the contact may not follow the wheel surface motion. Furthermore, a soil particle at this location shows a higher tendency to *escape* to the surface. This means that its tendency to become compacted is lower. Even further improvement to the model can be achieved by improving these aspects of the velocity field. This can be done based on experimental observation and analysis of the motion of soil particles under a wheel. For example, the soil visualization techniques used by Senatore et al. (2012) and Skonieczny et al. (2012) could be used for this.

As an example of using the visualization techniques mentioned above, the velocity filed obtained from the experiments reported by Senatore et al. (2012) is used to compare with the velocity field assumed in this thesis. The experimental result is shown in Fig. 3.21, while our simulation result is shown in Fig. 3.22. The comparison shows that the proposed velocity field can closely capture the experimental results for the type of soil and loading condition used in the experiments of Senatore et al. (2012).

Velocity field parameters, α_1 , α_2 , and α_3 , have to be identified in order to use the proposed model. However, these parameters are not inherent to either the Drucker-Prager

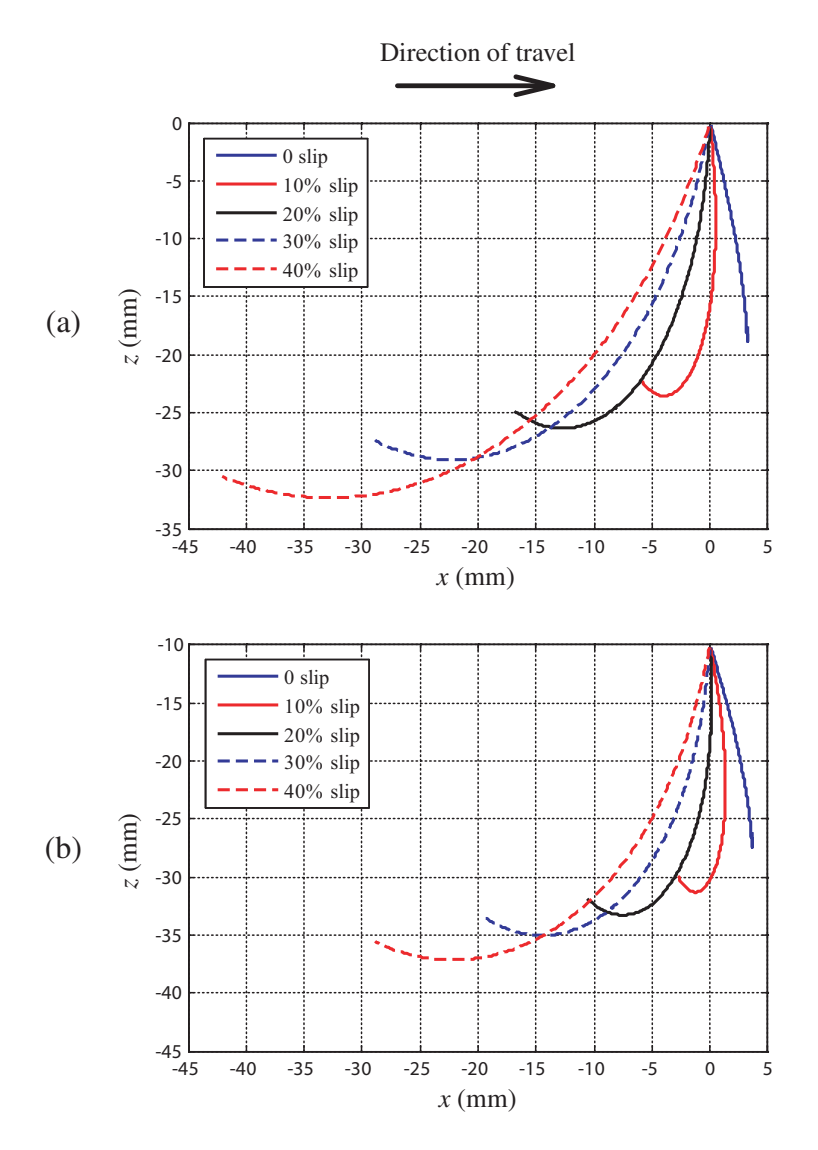


FIGURE 3.19. Trajectories of a soil particle when a wide rigid wheel with a diameter of 0.3 m moves over it at various slip ratios, as predicted by the proposed velocity field. Wheel and soil properties are the same as those used in this section: (a) Soil particle is initially at the soil surface; and (b) soil particle is initially 10 mm below the soil surface.

parameters or the Bekker model (α_1 and α_3 have units of m⁻¹ and α_2 is dimensionless). These parameters, however, are related to soil properties. Based on our observation from various simulation trials, we noticed that by varying α_1 and α_2 , we can cover a rather wide range of soil parameters, characterized by a range of values of n and k_{ϕ} of the Bekker model, without changing any parameter in the Drucker-Prager constitutive relation. Shear

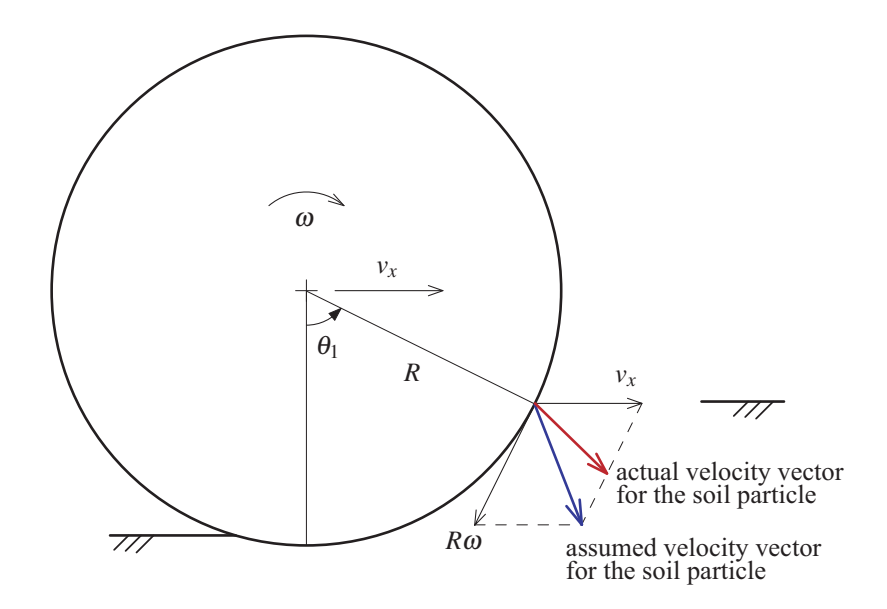


FIGURE 3.20. Schematic of assumed and actual velocity vectors of soil particle near the beginning of contact when the entry angle (θ_1) is relatively large.

response can also be captured by tuning α_3 and ϕ (and c if soil cohesion is significant). This interesting behaviour suggests that any parameter identification algorithm may need to focus on finding α_1 and α_2 based on the normal stress distribution, independent of α_3 and ϕ (and possibly c). This reduces the dimensionality and complexity of the identification problem. Also, identifying the other Drucker-Prager parameters is often not needed.

Considering these observations, we used a trial-and-error approach in selecting velocity field parameters. To appropriately select α_1 and α_2 , it is required to have normal stress distribution around the wheel at one operating condition with 10–20% wheel slippage. As this information is usually not available, we use the Bekker model to find a normal stress distribution. Here, we assume that the pressure-sinkage parameters are known. Parameters α_1 and α_2 are, then, selected such that the normal stress distribution (from the entry angle to the point of maximum stress) under the wheel at 20% slippage closely matches Bekker's pressure-sinkage curve.

After selecting α_1 and α_2 , α_3 is selected such that the traction force in an operating condition with 15–20% wheel slippage under a given vertical load on the wheel is close to

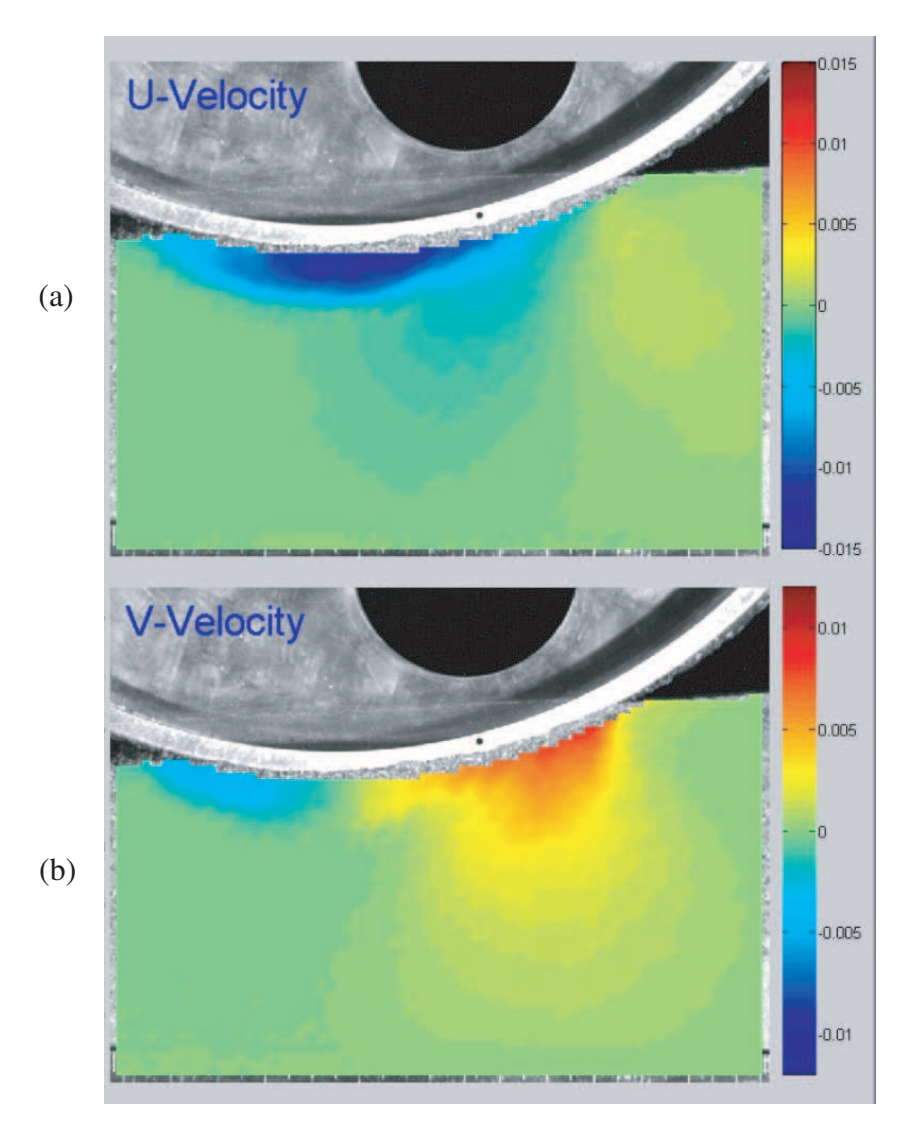


FIGURE 3.21. Velocity field of soil particles under a rigid wheel moving with 30% slip ratio: (a) the horizontal; and (b) the vertical velocity components. The unit of color bars is m/s (Courtesy of Karl Iagnemma from MIT)

the traction force calculated from the Bekker model. It should be noted that selection of these parameters is done at only one loading and operating condition, but the results are valid over a wide range of loading conditions, as shown in Figs. 3.5–3.7.

3.4 Validation with Experimental Results

The experimental data reported by Ding et al. (2011a) are used for validation of the model proposed here. Wheel radius and width are 157.35 mm and 165 mm, respectively.

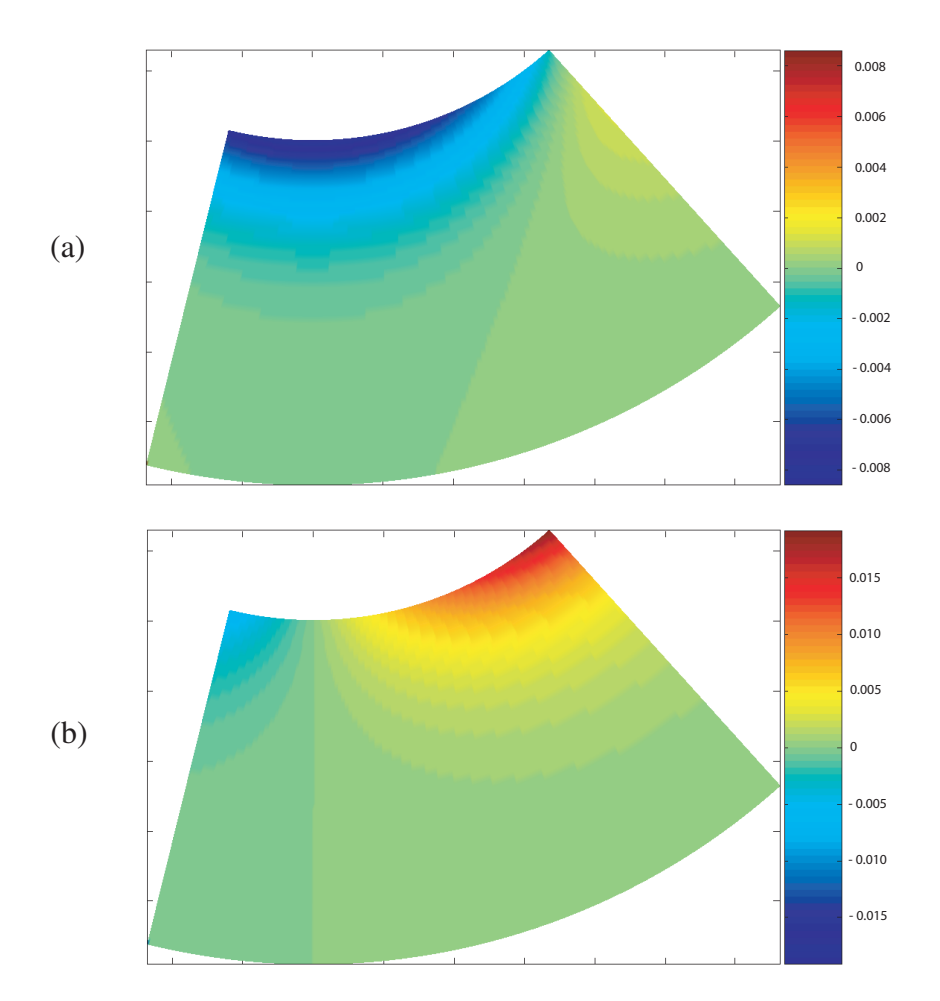


FIGURE 3.22. Colour plots of the proposed velocity field for soil particles under a rigid wheel moving with 30% slip ratio: (a) the horizontal; and (b) the vertical velocity components. The unit of color bars is m/s

The steady-state response of our model is compared with the experimental data for various values of slippage—Figs. 9(a), 9(b) and 9(c) of Ding et al. (2011a). The experimental data reported for a wheel with no grousers, a wheel with 5-mm grousers, and a wheel with 10-mm grousers are used for comparison, as shown in Figs. 3.24–3.26. To this end, a single-wheel testbed is simulated in *Vortex*, in which forward and angular speed of the wheel are controlled, while the wheel is free to move in the vertical direction, same as the example discussed in Section 3.3.2. The soil data set used for parametrization of the elasto-plastic constitutive relation is the same as what was used in the previous section, except for β and d, which are set to 42.4° and 367 Pa, respectively, according to Eq. (3.12). This is done

in order to comply with the soil properties reported by Ding et al. (2011a), where ϕ and c are 31.9° and 250 Pa, respectively. It should be noted that the model parameters required for our elasto-plastic constitutive relation were not available in (Ding et al., 2011a)⁷. In spite of that, by tuning the parameters of the velocity field according to Section 3.3.4, the terrain response is closely captured. Numerical values of the velocity field parameters are displayed in Table 3.5. The vertical position of the wheel centre is shown in Fig. 3.23 during this motion.

TABLE 3.5. Parameters of the proposed velocity field used in the experimental validation

$\alpha_1 (m^{-1})$	α_2 (-)	$\alpha_3 (\mathrm{m}^{-1})$
1.0	0.045	25

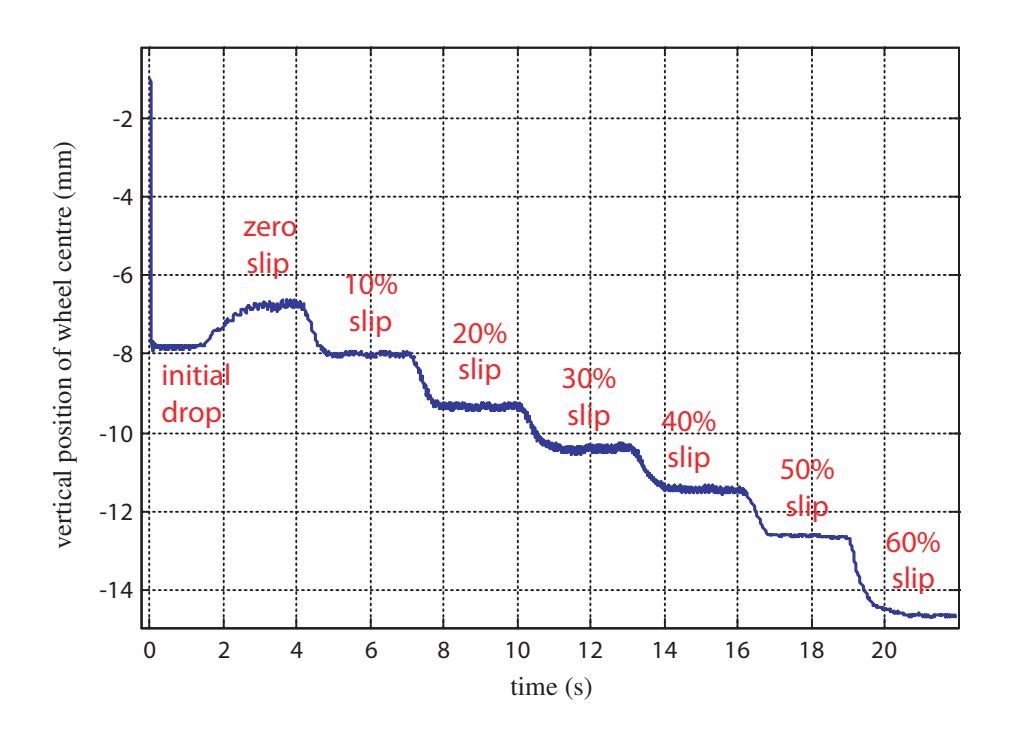


FIGURE 3.23. Vertical position of wheel centre vs. time under an 80-N vertical load on the wheel centre and different slip ratios, as predicted by our model

⁷Appropriate parameter identification of this elasto-plastic model can be done by means of triaxial test data (Helwany, 2007).

The slip-sinkage phenomenon is captured by our model; however, as can be seen from Fig. 3.24, the sinkage is underestimated compared with the experimental data. In our model, the sinkage increases from almost 7 mm at zero slip to around 15 mm at 60% slip, whereas in the experiments reported for a wheel with no grousers, the sinkage increases from around 6 mm to around 17.5 mm⁸.

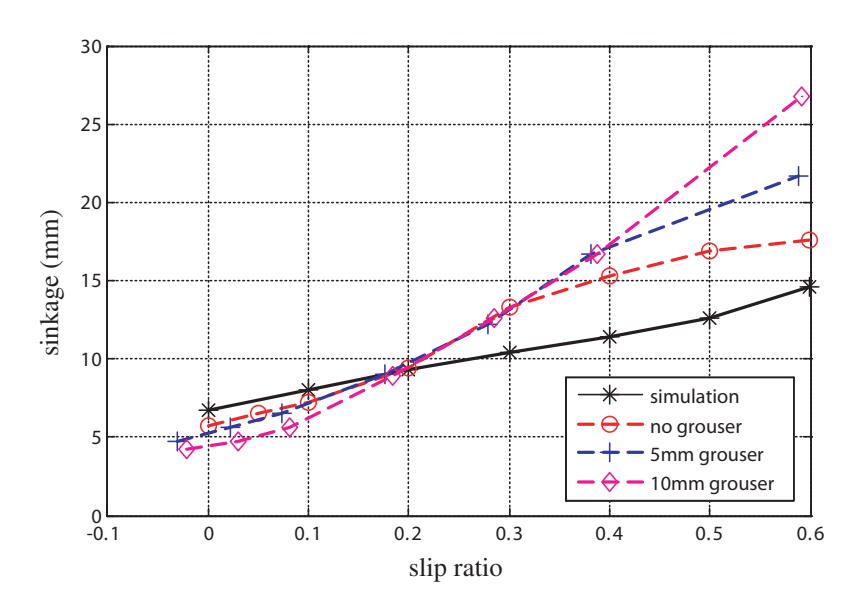


FIGURE 3.24. Variation of wheel sinkage vs. slip ratio under an 80-N vertical load on the wheel centre

Even though the predicted wheel sinkage values are not exactly the same as in the experimental data, it is noteworthy that generally, the experimentally observed behaviour is naturally captured by the proposed model. In addition, the drawbar pull and driving torque estimation match the experimental data fairly well, as shown in Figs. 3.25 and 3.26.

In order to further verify the scalability of our model, its prediction is compared with the experimental data under the different vertical loads reported by Ding et al. (2011a). However, the only available data are for a wheel with 10-mm grousers under 35 N, 80 N, and 150 N vertical loads. The comparison is displayed in Figs. 3.27–3.29. As expected, the

⁸It is noted from observing the experimental data in Fig. 3.24 that the sinkage at zero slip ratio decreases when the grouser height increases. This suggests that, in these experiments, the sinkage has been measured from the wheel surface, not from the grouser tip. In this case, the extra support, provided from grousers penetration in soil, causes the wheel to sink less.

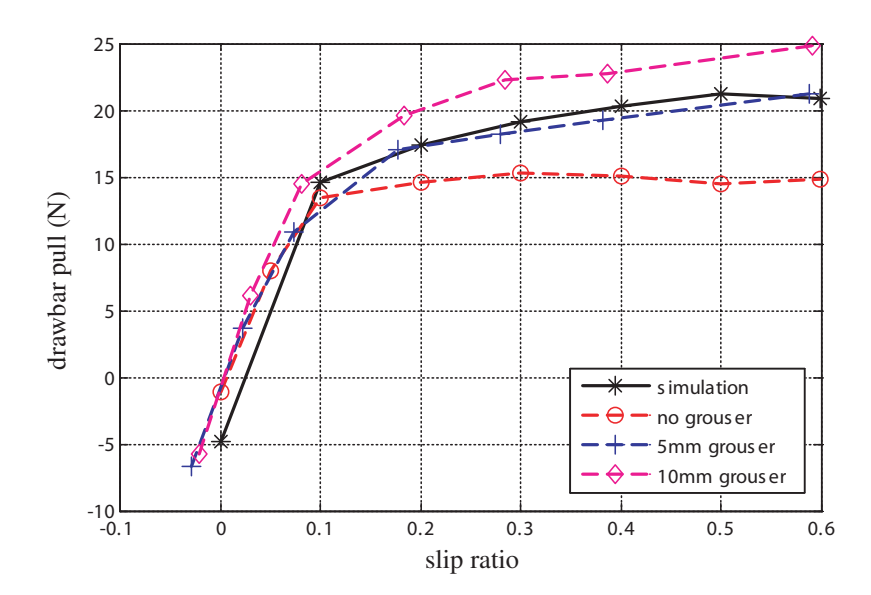


FIGURE 3.25. Variation of developed drawbar pull vs. slip ratio under an 80-N vertical load on the wheel centre

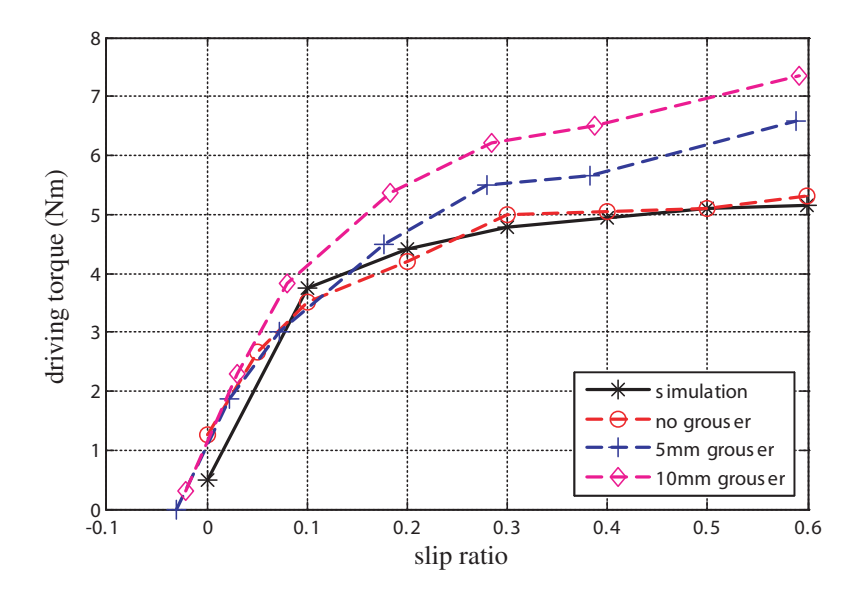


FIGURE 3.26. Variation of applied torque on the wheel vs. slip ratio under 80-N vertical load on the wheel centre

slip-sinkage is underestimated, due to the extra sinkage that these relatively big grousers have caused in the experiments. Drawbar pull and driving torque (Figs. 3.28 and 3.29, respectively), are captured relatively well.

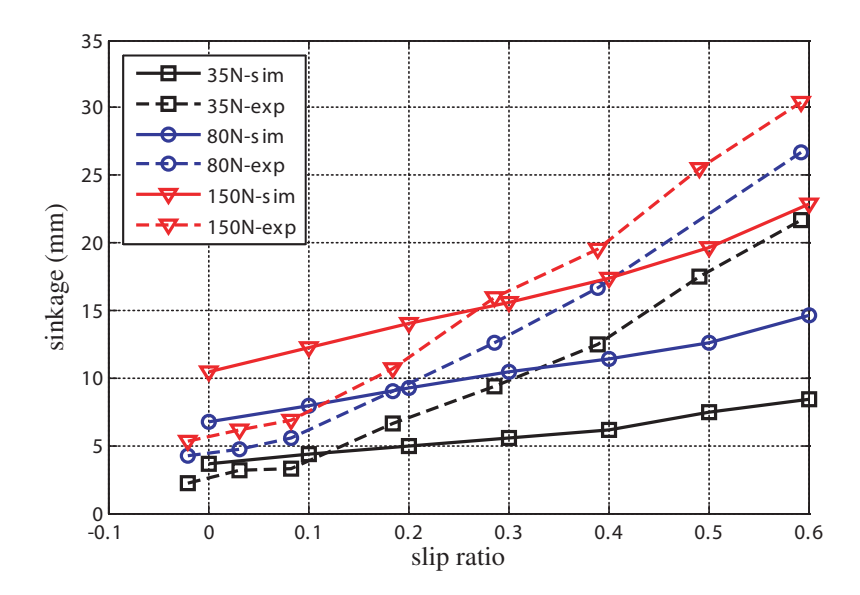


FIGURE 3.27. Comparison of wheel sinkage computed from the plasticity model with experimental data reported in Fig. 18 of Ding et al. (2011a), under a 35-N, 80-N, and 150-N vertical load acting on the wheel centre. A rigid wheel with 10-mm grousers was used in the experiments.

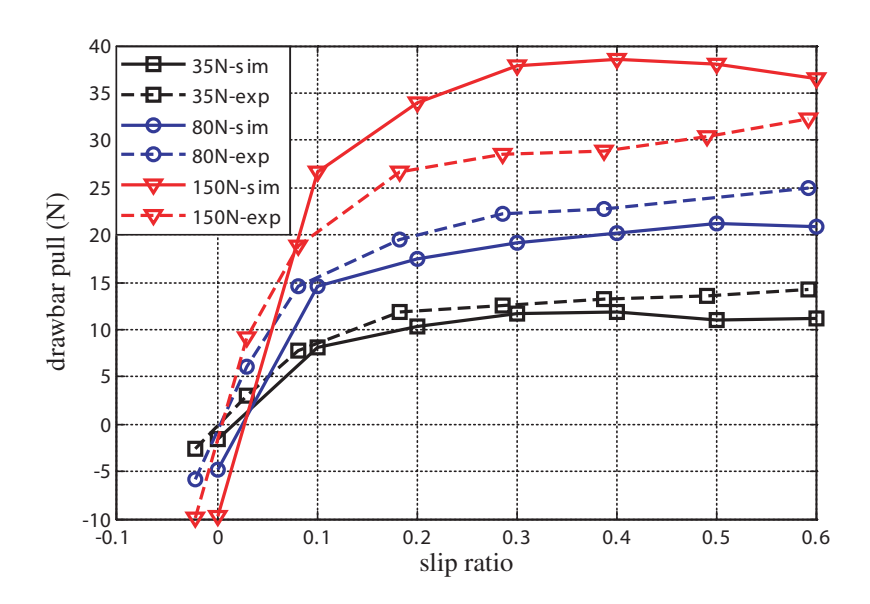


FIGURE 3.28. Comparison of the drawbar pull computed from the plasticity model with experimental data reported in Fig. 18 of Ding et al. (2011a), under a 35-N, 80-N, and 150-N vertical load on the wheel centre.

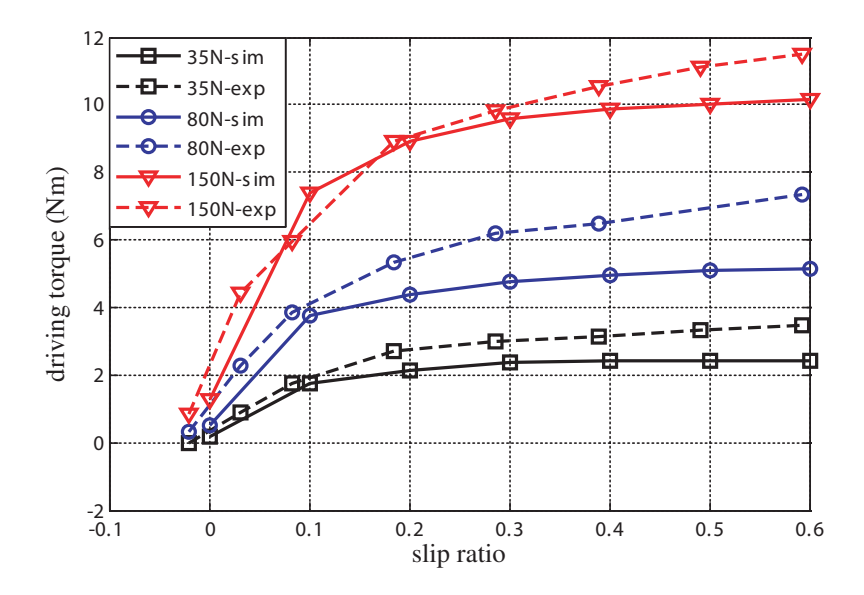


FIGURE 3.29. Comparison of the driving torque computed from the plasticity model with experimental data reported in Fig. 18 of Ding et al. (2011a), under a 35-N, 80-N, and 150-N vertical load acting on the wheel centre.

3.5 Integration In the Multi-body System

Algorithm 2, in combination with Algorithm 3, is suitable for implementation in the multi-body dynamics simulation environment *Vortex*. Using these algorithms, soil reactions are readily determined. These reactions can be added directly to the wheel as external loads or by using the approach explained in Sections 2.4.2.1 and 2.4.2.3, in which the latter is used here. It should, however, be mentioned that the damping coefficient c_z introduced in Eq. (2.4) is set to zero in all implementations associated with the elasto-plasticity model, as the energy dissipation is ensured by capturing the plastic deformation in soil.

In this implementation, the terrain surface is represented by a height-field, similar to the approach explained for semi-empirical models in Section 2.4.5. The active vertices, explained in Algorithm 2, are determined by intersecting the wheel and the height-field vertices. The least-squares plane approximation of the terrain, as discussed in Section 2.4.5, is also used here to find the terrain normal $\mathbf{n}_{\text{terrain}}$ and the wheel sinkage. Deformation of the terrain and changes in the hardening/softening parameter, $\varepsilon_{\text{vol}}^p$, are stored in the vertices of

the height-field. It is noted that this approach directly captures elasto-plastic deformations and soil-hardening/softening properties, which directly results in the multipass effect.

Moreover, as a lateral force model is required to operate the rover on an irregular terrain, the lateral force model explained in Section 2.4.3.1 is also added to the model. For that, the normal stress distribution obtained from the elasto-plasticity model is used to determine the shear stress in the contact area using Eq. (2.18). The shear stress is then integrated over the contact area to determine F_l , which is used to set up the set-valued function representation of the lateral force with its complementary kinematic variable expressed in Eq. (2.25).

3.6 Execution Time of the Proposed Algorithms

Plane-strain FE simulation of a rigid cylinder on soil with Abaqus/Explicit was conducted for comparison of execution time between the proposed approach and FEA, as shown in Fig. 3.30. In this case, the wheel radius was 0.15 m and the wheel centre velocity 0.00375 m/s with a slip ratio of 20%. The wheel was released with zero initial velocity and zero sinkage, while it was touching the soil surface. During the first 3.1 s, the wheel only moved in the vertical direction under gravity. Then, it was gradually accelerated to reach its final speed in 5 s. It continued moving with this velocity and 20% slip ratio. It took about four hours to simulate 83.1 seconds of motion. The same motion was simulated using the new approach with a wheel using 72 mesh points, which resulted in 8–9 active mesh points, with total simulation time of about 180 s on the same processor (Intel CoreTM 2 Duo T7500 @ 2.2 GHz). This means about 80 times faster than with the FE simulation mentioned above. The code based on the proposed approach, however, was written in Matlab and only a single CPU core was used; therefore, shorter execution times are possible if parallel computing is used.

In addition, as shown in Fig. 3.31, simulation of the Sojourner rover was conducted in Vortex using the proposed approach on an Intel CoreTM i7-920 processor @ 2.67 GHz.

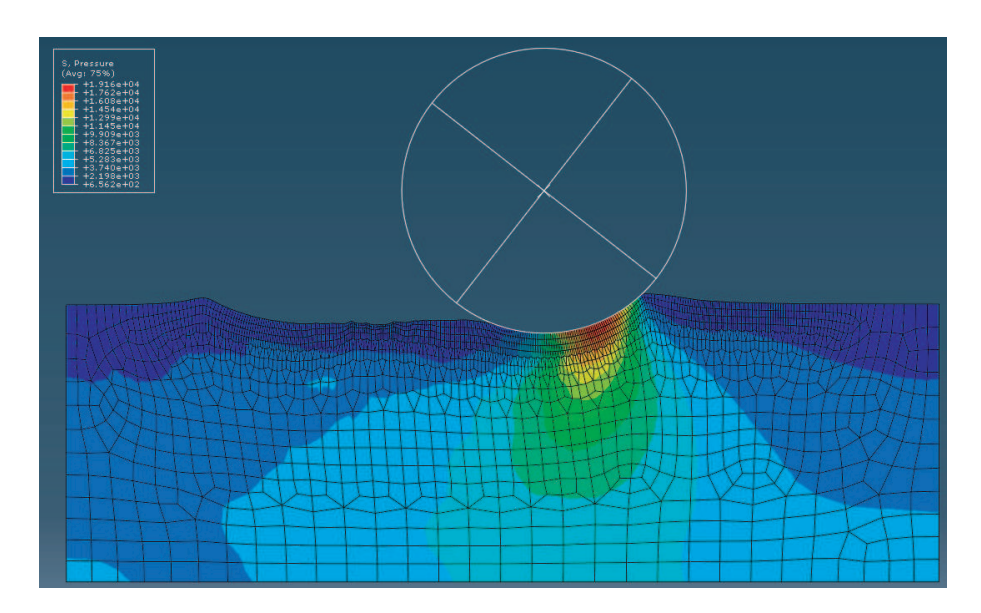


FIGURE 3.30. Plane-strain FE simulation of a rigid cylinder on a soil with Abaqus/Explicit. The cylinder moves with 20% slip ratio.

This rover has six wheels but all of the computations associated with the new model were performed on a single CPU core. During straight-line motion with a rover speed of 0.10 m/s, every second of motion took about 13 s simulation time, while the total number of active mesh points was 52 on average, which means about nine active mesh points per wheel. Since this simulation was performed using only a single CPU core for the computation associated with the new model, interactive and even real-time performance can be achieved for slow-moving rovers if the data-parallel nature of this model is used. It should be noted that each active mesh point can be executed independently from the others, which makes the model data-parallel, and therefore, readily parallelizable. This feature, however, has not yet been implemented.

It is noted that for implementation on a single CPU core, the execution time linearly depends on the number of active mesh points. As the wheel sinkage grows, the number of active mesh points increases, which in turn can result in variation of the computational time. This is not desirable for real-time applications. However, parallel processing can help in improving that situation. The other variable that directly affects the execution time is the



FIGURE 3.31. Sojourner rover simulation in Vortex using the elasto-plasticity model. The rover moves on a height-field and the soil deformation and the hardening parameter are stored in the height-field vertices.

rover speed. A higher rover speed requires a smaller time-step to ensure the convergence of the elasto-plasticity solver, which could, in turn, increase the overall execution time.

It is also noted that by decreasing the number of mesh points on the wheel, which in turn decreases the number of active mesh points, the discretization error increases. This could lead to substantial oscillatory behaviour in the computed reaction forces. We recommend to choose the settings such that in a 2D simulation of a wheel, at least five active mesh points cover the contact area.

3.7 Further Discussion and Comparison with Semi-empirical Models

The results obtained with the proposed model and the assumed velocity field were close to those obtained based on the WR and Bekker models under steady-state operating conditions for a particular slip ratio, as shown in Section 3.3.

Some of the limitations of the semi-empirical models were listed in L1 and L2 (Section 2.3). To address limitation L1, a remedy is adding a damping term in the *z*-direction,

as done in Chapter 2. However, in the method proposed in this chapter in Algorithm 2, the energy dissipation due to dynamic motion in the *z*-direction is captured by using an elasto-plastic soil representation.

Regarding the slip-sinkage phenomenon, the results obtained with the proposed method showed a clear dependency of normal stress distribution on the slip ratio, with larger slip ratio resulting in larger wheel sinkage. This aspect was analyzed in Section 3.3.3. The results of this approach are also compared with the experimental data reported by Ding et al. (2011a); this comparison in Section 3.4 showed good agreement between the proposed model and the experimental data, regarding the slip-sinkage phenomenon.

REMARK 13. A modification to the pressure-sinkage exponent n in the WR model was suggested by Ding et al. (2010a), in order to capture the slip-sinkage behaviour observed in their experimental data. To do so, they assumed that n changes linearly with the slip ratio of the wheel, but no theoretical analysis was provided. \square

Moreover, the stress distribution under the wheel obtained from the novel approach is affected by the type of motion that the wheel undergoes. For example, consider the example discussed in Section 3.3.2. At instants 0.045 s and 0.095 s when the wheel is moving downward under the action of gravity, the normal stress distribution is even, as shown in Fig. 3.32, while the shear stress is odd. As a result, the soil reaction can be expressed as a single vertical force vector, as expected. In addition, when the wheel is moving, the evenness no longer holds, as shown in Fig. 3.33, due to plastic deformation in soil. It should be noted that this behaviour is achieved without any need for considering special cases for a moving or stationary wheel, which is a limitation of semi-empirical relations as discussed in Section 2.3 under L2. It should be mentioned that the only difference from the conditions of the example in Section 3.3.2 and the results displayed in Figs. 3.32 and 3.33 is the use of 180 mesh points for the wheel, instead of 72.

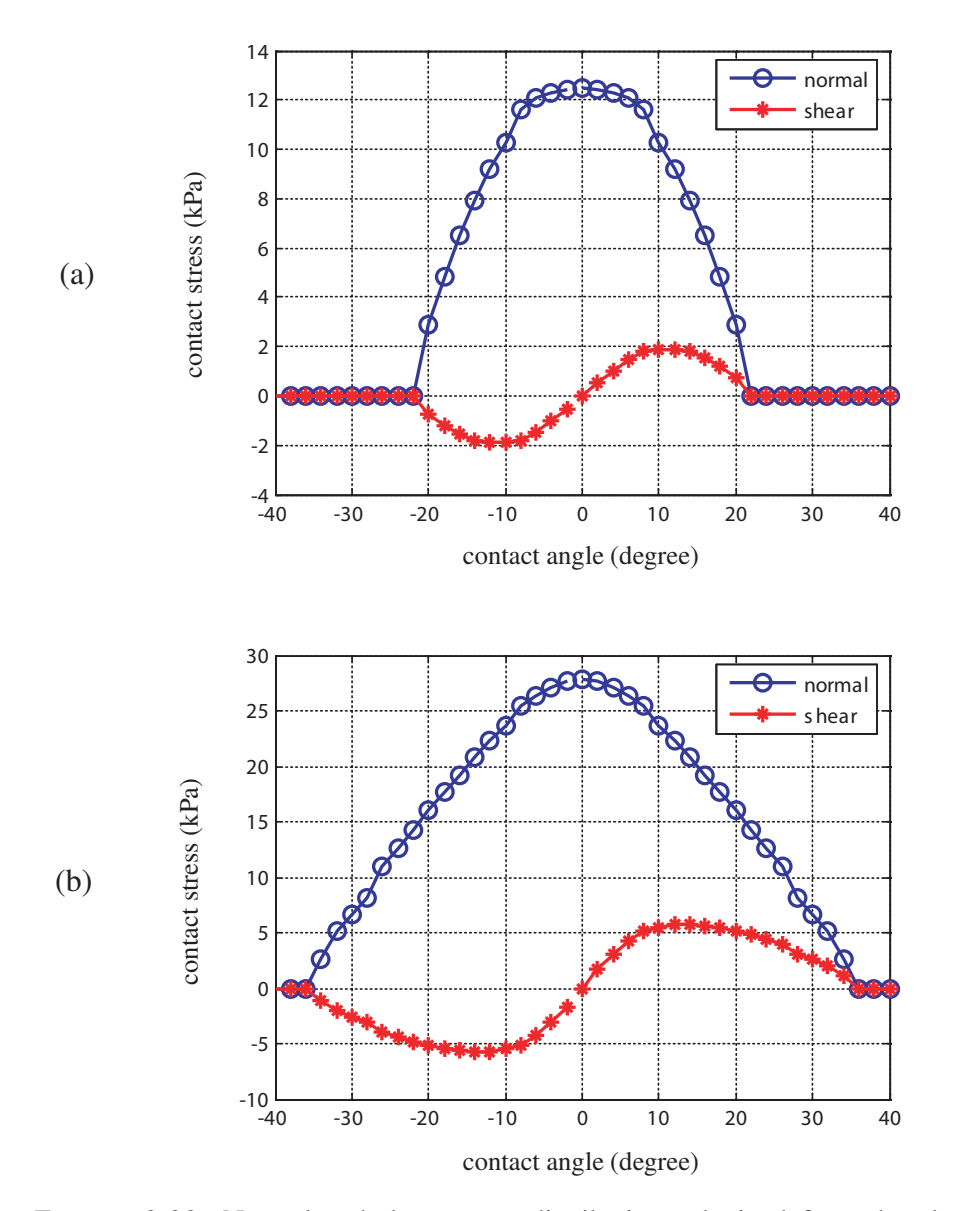


FIGURE 3.32. Normal and shear stress distributions obtained from the elastoplasticity model when the wheel is moving downward in the example included in Section 3.3.2: (a) stress distributions at t = 0.045 s and $v_z = -0.357$ m/s; (b) stress distributions at t = 0.095 s and $v_z = -0.194$ m/s. As expected, the contact stresses are such that soil reaction can be expressed with a single vertical force vector.

It is noted that in the approach introduced in this thesis, no special assumption is considered to capture certain features like the slip-sinkage phenomenon. These features are natural outcomes of the model. This, together with the other features, makes this novel model and framework conceptually different from semi-empirical models. In addition, the

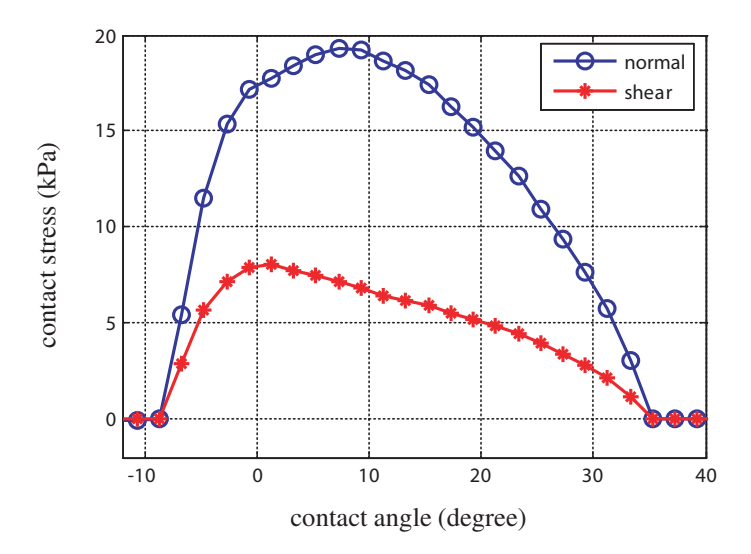


FIGURE 3.33. Normal and shear stress distributions obtained from the elastoplasticity model when the wheel is moving with 10% slip. The result correspond to t = 6.495 s and $v_z = 0$.

proposed approach provides a framework for the more efficient use of elasto-plasticity theory. Today, elasto-plastic constitutive models of soil are only used with FEM for wheel-soil interaction analysis, but rover simulation on soft soil with FEM is prohibitively slow for interactive simulation or mission planning, for example. The proposed approach provides a good balance between fidelity and computational efficiency, by eliminating the need of FEM.

CHAPTER 4

Experimental Investigation and Rover Simulation

4.1 Introduction

An extensive set of experiments was conducted using a version of the Juno rover (Juno II) that is owned by the Canadian Space Agency. The experiments were planned and performed by our McGill research team with help from personnel of the Canadian Space Agency, University of Waterloo, and Neptec Design Group. The author of this thesis played a key, leading role in planning and carrying out these experiments. The experiments were conducted at the facilities of the Canadian Space Agency in Ottawa. The rover used in the experiments is displayed in Fig. 4.1.

In this chapter, a brief description of the rover and its model developed in *Vortex* are presented in Section 4.2. In Section 4.3, a set of experiments conducted for identifying rover properties like its total mass and centre of mass, its overall drive-train friction, and motor constants are discussed.

The drawbar pull experiments performed on soft soil is the focus of Section 4.4. In this section, the experimental results are compared with the results from simulation. The simulation runs are conducted using the two wheel-soil modelling approaches developed



FIGURE 4.1. Pictures of the Juno rover, captured during experiments.

and described in Chapters 2 and 3. Furthermore, the rover is loaded with extra weight and the drawbar pull experiments are repeated in order to investigate the scalability of the models developed in the thesis.

In Section 4.5, motion on irregular surfaces is investigated, upon comparing the experimental results with the outcomes of both simulation models.

In addition to the experiments reported and analyzed in this thesis, other experiments were conducted as well, including traversing obstacles and steering manoeuvres. These will be used for further investigations and developments.

4.2 Description of the Rover and its Model

Juno II is a four-wheel rover with a linked walking beam suspension system (Visscher and Reid, 2012). It was developed by Neptec and Ontario Drive Gear (ODG) for the Canadian Space Agency. Juno II has two walking beams that are connected to form the suspension system. This suspension makes the rover capable of adjusting the orientation of its main body while travelling over obstacles and uneven terrain. In addition, it has an active part in the suspension that allows for tilting the main body by means of a linkage. On each side of the rover, two wheels are connected to a walking beam; each pair of wheels

on the side are driven using a single DC motor (Fig. 4.2). Furthermore, the rover uses skid steering.

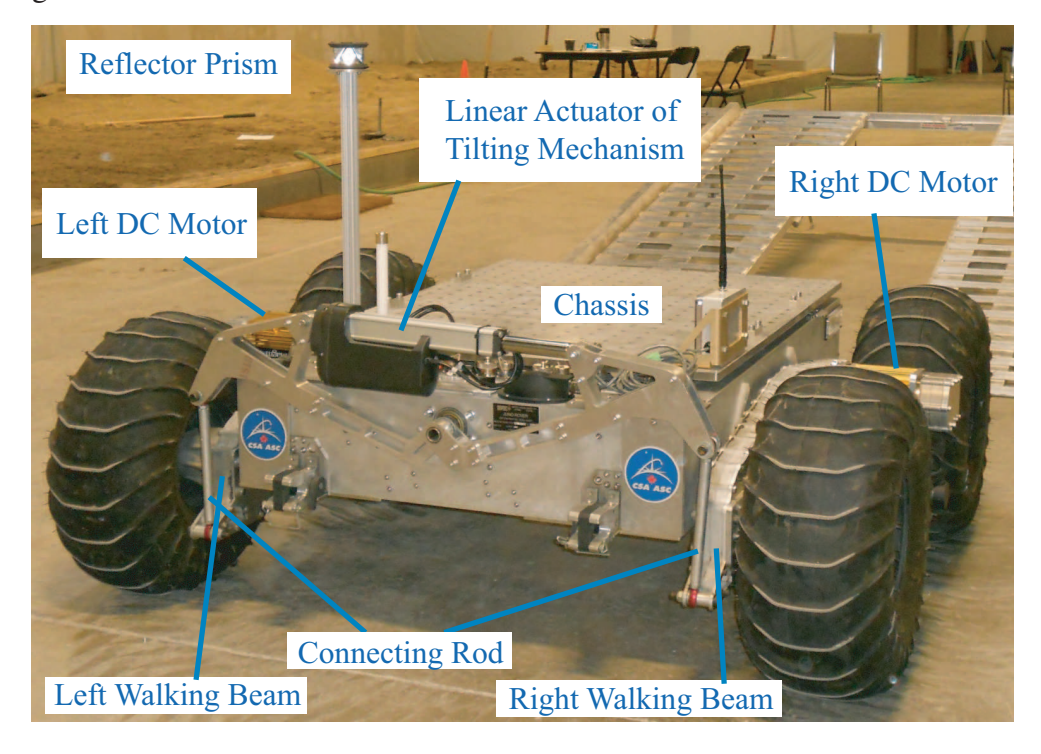


FIGURE 4.2. Juno II rover

Overall approximate dimensions of the rover are 1.4 m in length, 1.5 m in width, and 0.6 m in height, with a total mass of approximately 317.6 kg. The wheels used during experiments were ARGO tires with small grousers. The wheels have 22" diameter, including the height of the grouser.

A full-scale model of the rover was developed in *Vortex*; snapshots of the rover model during simulation are shown in Figs. 4.3 and 4.4. In order to develop this model, a CAD model of the rover was used. The multi-body model of the rover has 13 rigid bodies and 15 joints. The rigid bodies and joints used in modelling the rover are shown in Fig. 4.5. The rigid bodies are representations of: the chassis, two walking beams, four wheels, and six bodies that connect the walking beams to the chassis at the rear end of the rover and allows for tilting the chassis. The model of the rover in *Vortex* at different configurations of the tilting mechanism is shown in Fig. 4.4.

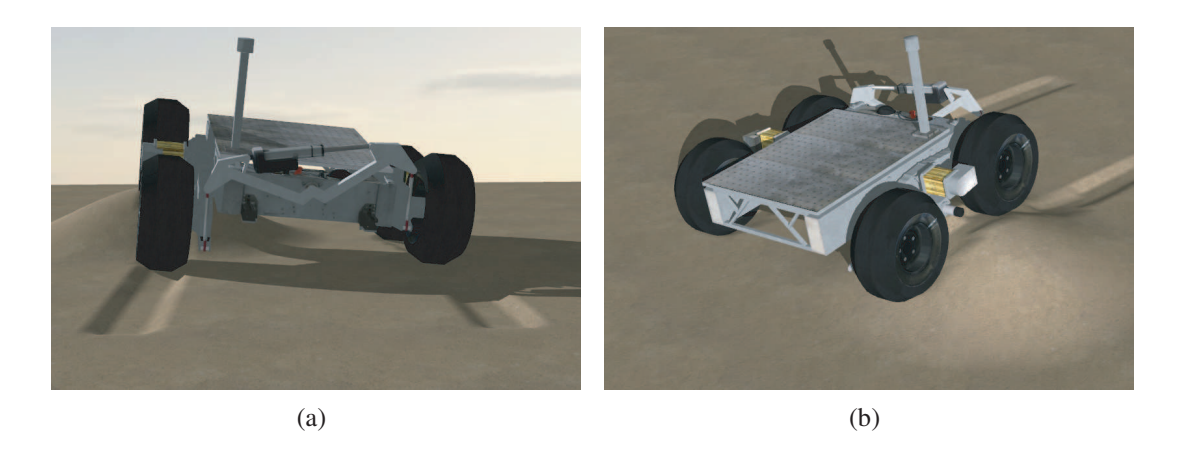


FIGURE 4.3. Images from the simulation of Juno rover in *Vortex*.



FIGURE 4.4. Simulated Juno rover in *Vortex* at different tilting configurations.

In *Vortex*, the above-mentioned rigid bodies, referred to as *parts*, are created at their appropriate location. The parts are restrained together with the joints shown in Fig. 4.5. As mentioned in Section 2.2, in order to detect contact between parts in *Vortex*, *collision geometries* can be added to the parts. Cylindrical collision geometries are considered for the wheels, while for the irregular terrain, a height-field is used.

Four types of joints are used in modelling the rover, which are revolute joint (RJ), prismatic joint (PJ), spherical joint (SJ), and universal joint (UJ), as shown in Fig. 4.5. A RJ or PJ adds five constraint equations to the multi-body dynamic equations. The RJ allows for the relative rotation of the two bodies around the revolute axis, while the PJ allows for relative translation along one direction. A UJ adds four constraint equations and allows for

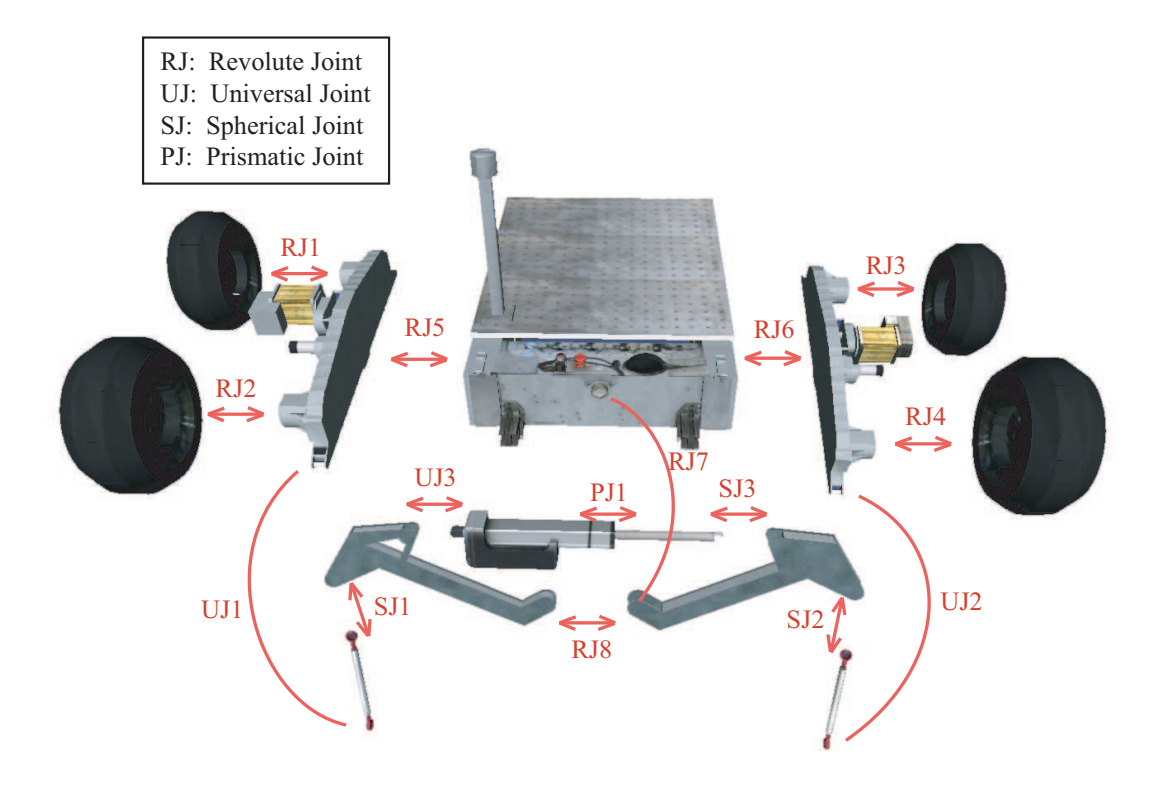


FIGURE 4.5. Illustration of the rover model with its joints. Totally, eight revolute joints, three universal joints, three spherical joints, and one prismatic joint are used in the multibody model of the rover.

rotations around two co-planar perpendicular axes. A SJ adds three constraint equations that constrain the relative position of the two bodies.

The allowable relative motion of some joints, e.g., relative rotation around the revolute axis of the RJ and relative translation along the prismatic direction in the PJ, can be controlled. These are referred to as *controllable joint coordinates*, which are either *free* or *actuated* in the model developed for the rover. In an *actuated* controllable joint coordinate, the relative velocity of the joint is specified, which adds an additional kinematic constraint to the model.

In order to command the rover to move with specified angular velocities for wheels, the controllable joint coordinates of the revolute joints connecting the wheels to the walking beams (RJ1, RJ2, RJ3, and RJ4 in Fig. 4.5) are *actuated*. The rover moves by commanding the appropriate angular velocities to these controllable joint coordinates. In addition, the

controllable joint coordinate of the prismatic joint (PJ1 in Fig. 4.5) is modelled as *actuated*. This allows us to tilt the rover. The rest of the joints in the model are *free* joints.

Furthermore, the torque or force associated to any of the above-mentioned kinematic constraints are determined from the Lagrange multipliers associated to the constraint equation. It is noteworthy that the torques required to maintain the kinematic constraints related to the controllable joint coordinates of RJ1 to RJ4 are of particular interest to us. These torques, which are determined from the Lagrange multipliers corresponding to their kinematic constraints, are used to determine the equivalent torques of the left and right DC motors, shown in Fig. 4.5. In this regard, the summation of the torques obtained from RJ1 and RJ2, divided by the gear ratio of the drive-train, provides the equivalent torque of the left DC motor determined from the simulation. Similarly, the torques obtained from RJ3 and RJ4 provide the equivalent torque of the right DC motor. In the subsequent sections, these torques are compared against the motor torques determined from experimental measurements.

4.3 Determining Rover Properties

For the inertial properties, the total mass of the rover and its centre of mass (COM) were determined experimentally. To do so, we placed a digital weighting scale under each wheel on a horizontal, flat concrete floor. This gave us the total weight of the rover and the location of its COM, as projected on the horizontal plane. In addition, we tilted the rover, as shown in Fig. 4.4, and recorded the readings of the weighting scales. This provided an approximate location for the COM of the chassis.

The mass of the wheels were also measured using the weighting scales. The rest of the inertial properties were determined based on the CAD model of the rover and its overall mass.

The rover was instrumented with

• a tachometer for each motor to measure the angular velocities of the motors, and

• an inertial measurement unit (IMU).

Furthermore, the rover was equipped with motor current measurement devices, which reported motor currents versus time during the experiments. The torque of each motor is determined in the thesis using the current measurements. In addition, the global position of the rover was measured using a *Total Station*¹ that tracks the position of a reflector prism attached to the rover². The reflector prism is shown in Fig. 4.2. During our experiments, the position of the reflector prism was recorded versus time.

Before operating the rover on soft soil, it was commanded to move on a horizontal, flat concrete floor and on a configurable metallic incline, as shown in Fig. 4.6.



FIGURE 4.6. Juno II on the configurable metallic incline.

The rover was operated at different velocities on a straight line trajectory on the horizontal, flat concrete floor. From this set of experiments, an approximation of the torque required to overcome the overall friction forces in the drive-train of the rover was found. Figure 4.7 shows the measured currents for each motor at different motor speeds.

¹http://www.worldoftest.com/totalstation.htm

²Total Station is an electronic-optical instrument that is used in surveying. This device can determine the position of a reflector prism with respect to the position of the device itself, as long as a clear line-of-sight is maintained between the prism and the total station.

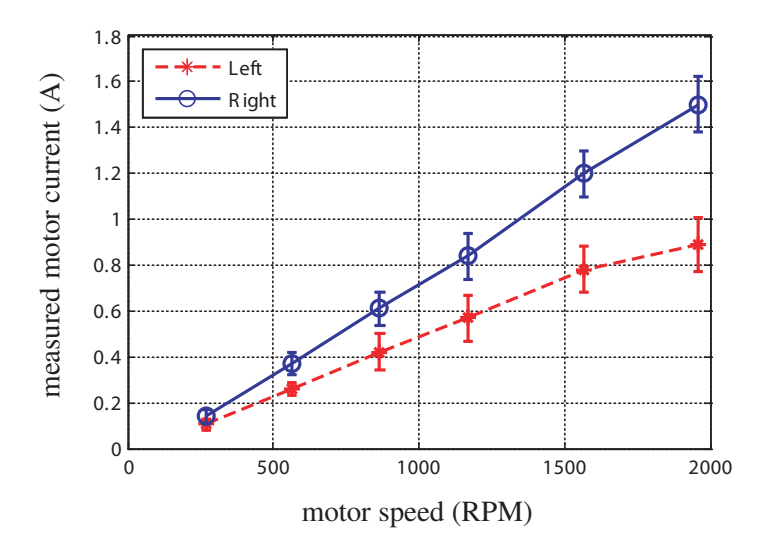


FIGURE 4.7. Measured current of both motors (left and right sides) versus average speed of the motors for the rover moving on horizontal flat concrete floor. The error-bars show the variation in the measured current.

The torque applied by each motor can be estimated from the measured current under the assumption of a linear relation between the current and the torque:

$$T_{\text{motor}} = \frac{K_{mt}}{\alpha_{dc}} A_{\text{motor}} \tag{4.1}$$

where $T_{\rm motor}$ is the estimated motor torque, $A_{\rm motor}$ is the measured current of the motor, K_{mt} is the motor constant related to torque, and α_{dc} is the *duty cycle* of the pulse-width modulation (PWM) driver of the motor. The duty cycle varies between 0 and 1. By changing the duty cycle, the effective voltage of the motor changes, which, in turn, causes the rover to move at different speeds. The relation between the duty cycle and the average motor speed is shown in Fig. 4.8. As expected, this relation is linear.

The motor constant K_{mt} is determined by driving the rover on slopes of 11.5° , 13.5° , and 15.5° . The comparison between the measured torques and the torques determined by simulation is shown in Fig. 4.9. As the motors are similar, the same K_{mt} was determined for both motors. These experiments were conducted by using a duty cycle of 0.45. It should be mentioned that a velocity-dependent friction is added to each controllable joint coordinate

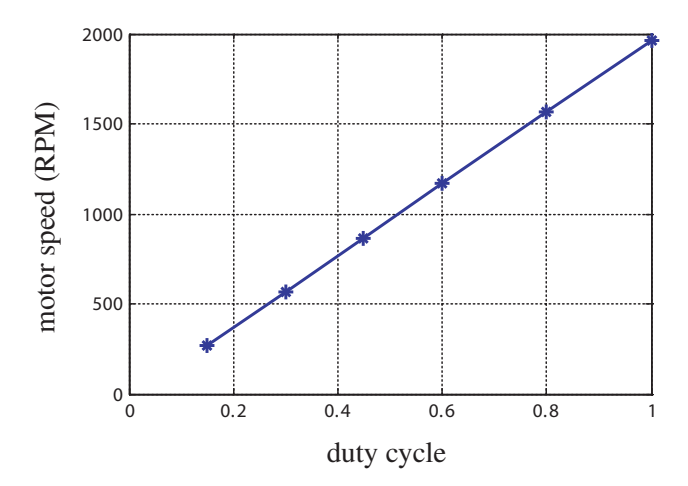


FIGURE 4.8. Average motors speed versus the duty cycle for the rover moving on horizontal flat concrete floor.

of the wheels, based on our measurements. To do so, the measured current in Fig. 4.7 with the duty cycle shown in Fig. 4.8 are used to determine the motor torque from Eq. (4.1). For each side of the rover, the motor torque determined in this approach is equivalent to the total drive train friction. For each side, the torque is multiplied by the total drive train ratio, in order to determine the equivalent friction that is added to the controllable joint coordinates of the wheels. With this model, the torque determined by simulation can closely match the torque expected from the experiments and can determine the energy expenditure for a certain manoeuver of the rover.

In the next section, the drawbar pull experiments are reported and the results compared with both modelling approaches. After that, the operation of the rover on uneven terrain is investigated. The trajectory of the rover and energy expenditure are compared from the simulation runs and experiments.

4.4 Drawbar Pull Experiments on Soft Soil

During this set of experiments, the rover was commanded to move in a straight line on uncompacted soil with a flat, horizontal surface. In the experiments, the rover was held by a rope, and its speed was manually controlled by constantly feeding a rope through a

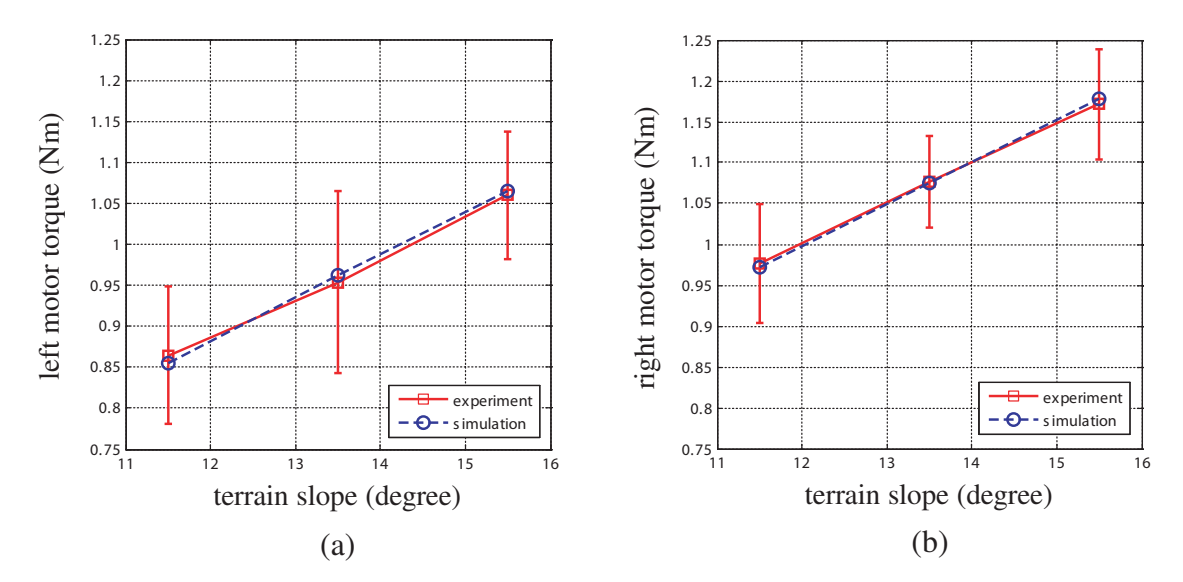


FIGURE 4.9. Comparing the motor torques obtained from the simulation and the torque determined from experiments using current measurements with the determined K_{mt} of 0.251: (a) left motor; (b) right motor

descender. The tension in the rope was measured using a load cell. This tension is equal to the drawbar pull developed by the rover. The input duty cycle of the motors was set to 0.45 in all experiments.

A picture of the descender and the load cell is shown in Fig. 4.10. The rover with the cable and the load cell attached to it is shown in Fig. 4.11. This picture was taken after finishing an experiment. In addition, a schematic diagram illustrating this set of experiments is shown in Fig. 4.12.

Several experiments were carried out. In each experiment, the intention was to keep the speed of the rover constant, but different from other experiments. This caused the wheels to maintain a relatively constant slip ratio in each run, while obtaining the results at different slip ratios. The average rover velocity and the average angular velocity of the rover were used to compute the slip ratio for each experiment. For one of the tests, the measurements over time are displayed in Figs. 4.13–4.16. As can be seen in Fig. 4.15, the angular velocity is fairly constant. In addition, rover speed can be assumed constant from Fig. 4.16, as the rover position changes linearly over time.

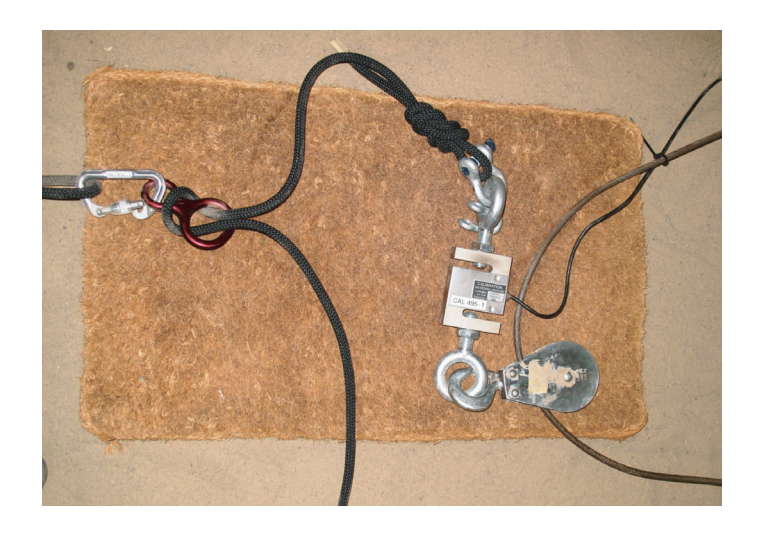


FIGURE 4.10. The descender and the load cell used in the drawbar pull tests



 $FIGURE\ 4.11.\ The\ rover\ attached\ to\ the\ load\ cell\ after\ a\ drawbar\ pull\ test$

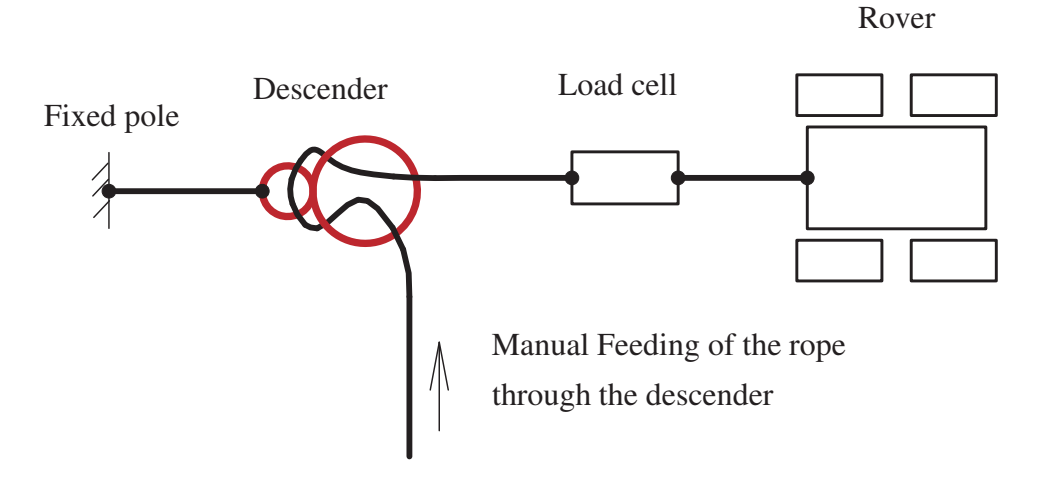


FIGURE 4.12. Schematic illustration of the drawbar pull experiments

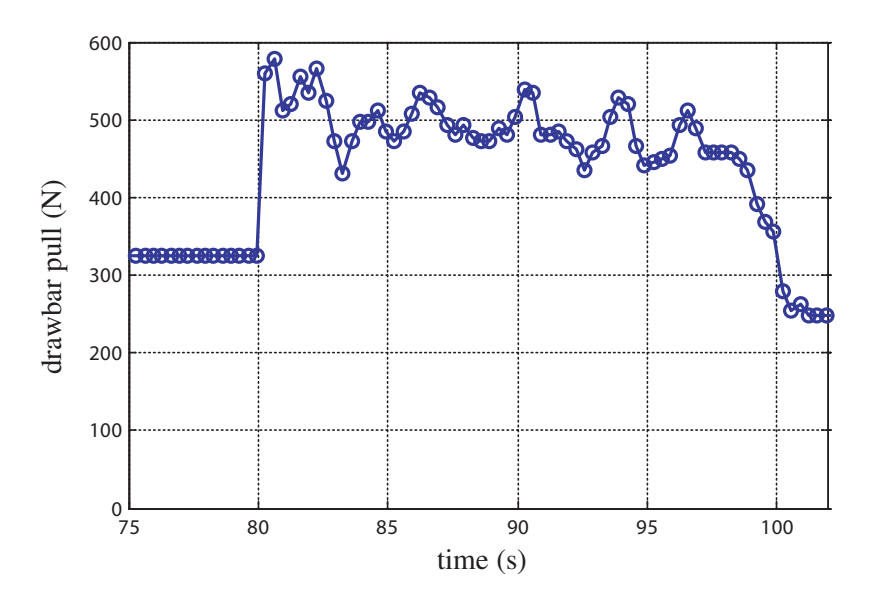


FIGURE 4.13. Measured tension in the rope over time. Sampling frequency of the load cell was 3 Hz.

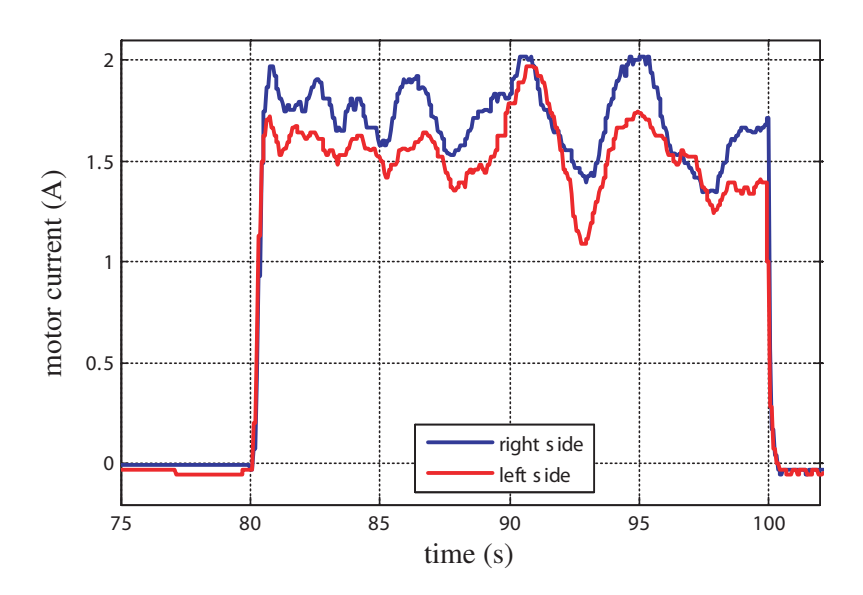


FIGURE 4.14. Measured motor current over time during the drawbar pull test. Sampling frequency was 20 Hz.

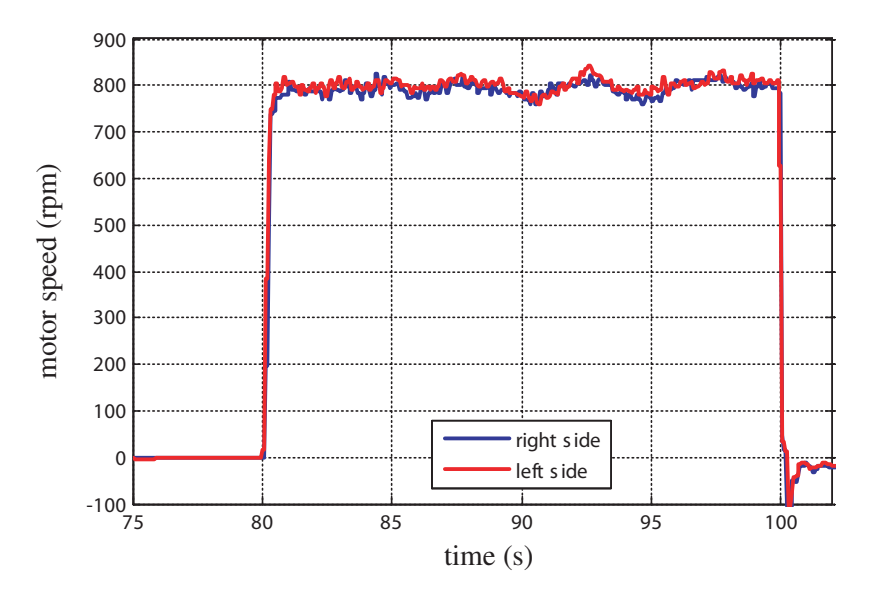


FIGURE 4.15. Measured motor speed over time during the drawbar pull test. Sampling frequency was 20 Hz.

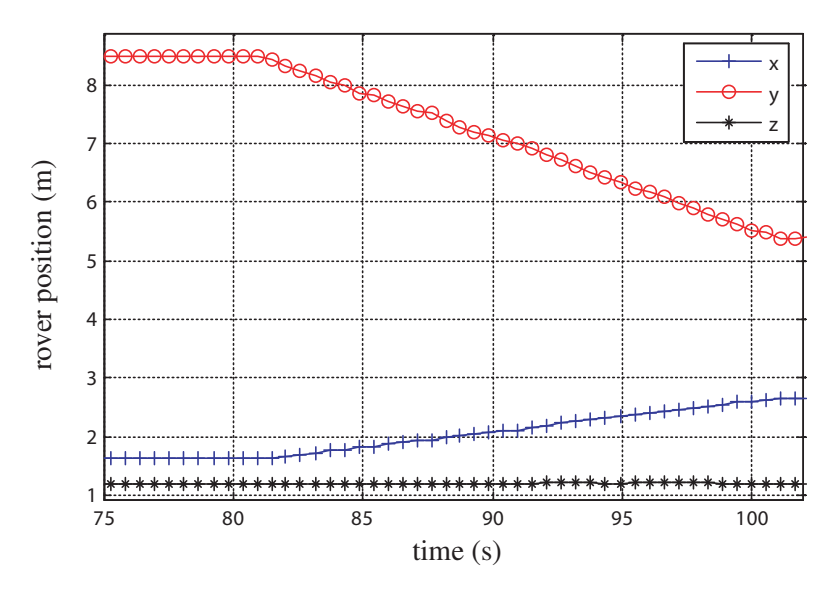


FIGURE 4.16. Measured rover position over time during the drawbar pull test. Sampling frequency of the total station was 2 Hz.

4.4.1 Comparison with a Semi-empirical Terramechanics Model

In order to conduct simulation runs, a setup similar to the drawbar pull experiments was created using *Vortex*. In this simulation setup, the terrain is represented by a height-field, as explained in Section 2.4.5. The terrain surface is initially flat and horizontal. In this setup, a resisting force, F_{DBP} , is applied to the rover chassis. This is the force applied by the rope to the rover in the experiment and is equal to the drawbar pull.

In each simulation run, the rover is commanded to move by setting a constant angular velocity to all wheels. As mentioned in Section 4.2, this is done by setting the proper angular velocities in the controllable joint coordinates of RJ1, RJ2, RJ3, and RJ4. In each simulation run, F_{DBP} is incrementally increased from zero to a desired drawbar pull value. By incrementally increasing the value of F_{DBP} , while the angular velocities of the wheels remain constant, the rover slippage increases gradually. After reaching the desired value for F_{DBP} , the rover moves under a steady-state condition with a constant slip ratio. The slip ratio, the final F_{DBP} , and the driving torque to each wheel are recorded from each simulation run.

TABLE 4.1. Parameters of the WRI model with multipass used in simulation runs with Juno II rover

φ (deg)	21
c (Pa)	2900
k'_{ϕ} (-)	300
k_c' (-)	0.69
n (-)	1.0
K_d (m)	0.004
<i>c</i> ₁ (-)	0.0
c ₂ (-)	0.45
λ (-)	0.2
$\gamma_s (\text{N/m}^3)$	1.2×10^4
$k_0 (\text{N/m}^3)$	0
$A_u (\text{N/m}^4)$	5.03×10^{8}

The framework developed and explained in Chapter 2 is implemented in *Vortex* and used for the simulation. The terramechanics relations are based on the WR model with

a non-zero exit angle, as suggested by Ishigami et al. (2007), which is referred to as WRI model in the thesis and was explained in Section 1.3. In addition, we employed the pressure-sinkage relation of Reece, expressed in Eq. (1.14), with this model. Furthermore, the multipass effect is considered in the simulation, as explained in detail in Section 2.4.5.

An important step in creating the simulation setup is the selection of soil parameters. These were selected and tuned based on the results of two experiments: (i) the experiment with no rope attached (no drawbar pull); and (ii) the experiment that corresponds to the maximum drawbar pull with the highest slip ratio³.

The tuned parameters of this model with the multipass effect are reported in Table 4.1. As explained in Section 2.4.5, k_0 and A_u are model parameters that define the elastic unloading/reloading behaviour. In addition, the soil is assumed to be initially uncompacted, in the model, as the terrain was prepared to be uncompacted before each experiment.

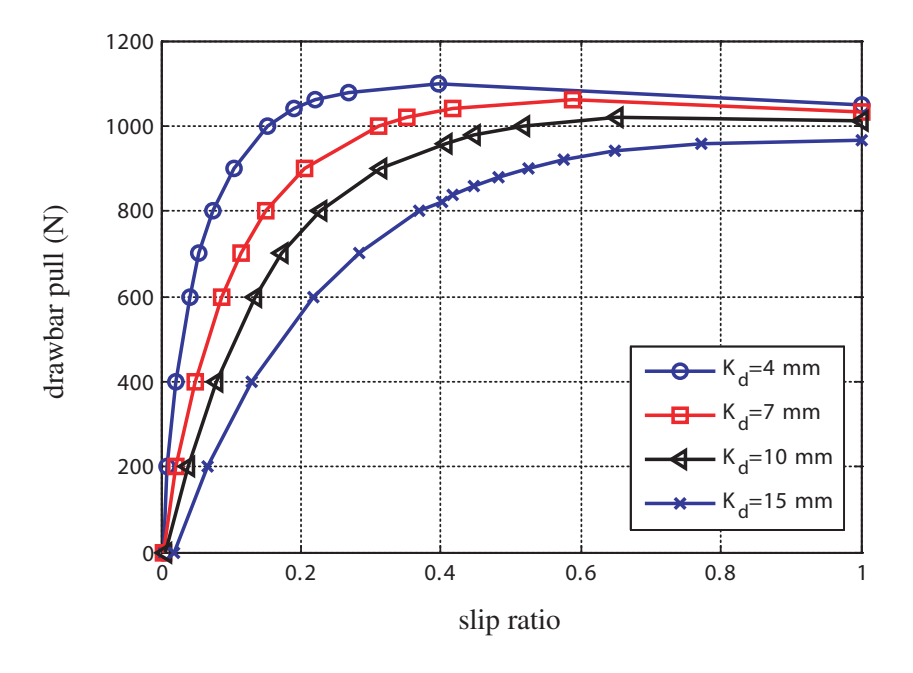


FIGURE 4.17. The drawbar pull versus slip ratio for different values of K_d .

³An alternative way in the selection of soil parameters for this model is via the plate-penetration and the shear tests using the bevameter. However, we did not have access to a bevameter during our experiments.

It should be mentioned that the critical soil parameters in this model are k'_{ϕ} , k'_{c} , ϕ , c, and K_{d} . k'_{ϕ} and k'_{c} determine the pressure-sinkage relation, Eq. (1.14), after selecting n and γ_{s} . As the wheel sinkage in the no-drawbar pull experiment is mainly dependent on the pressure-sinkage relation, k'_{ϕ} and k'_{c} are tuned such that the observed wheel sinkage of that experiment is close to the simulation results.

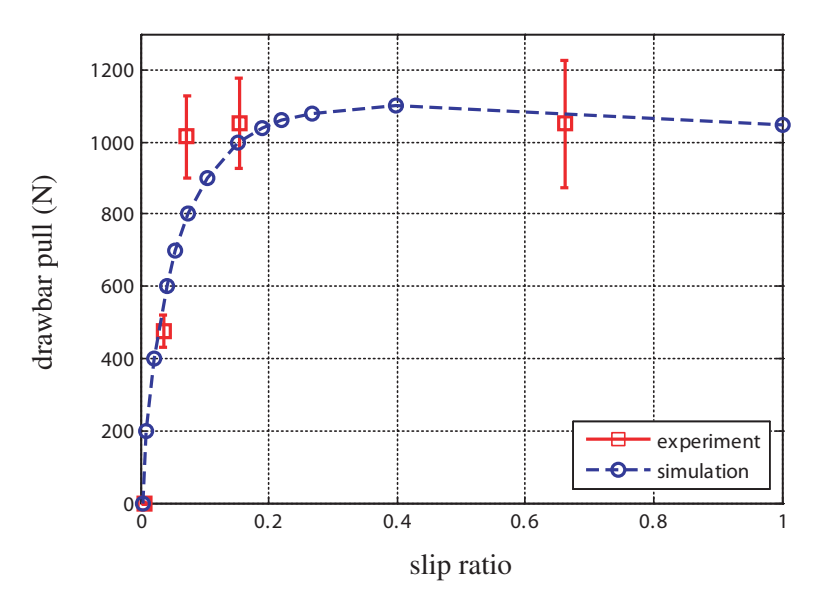


FIGURE 4.18. Comparing the drawbar pull obtained from experiments with the values obtained from simulation using the approach of Chapter 2 and the WRI model.

Moreover, as c and ϕ dictate the shear strength of soil according to Eq. (2.8), they are selected such that the maximum drawbar pull approaches the simulation outcome. The parameter K_d , which appears in Eq. (2.8), defines how the drawbar pull changes with slip ratio. The simulation results for different values of K_d are displayed in Fig. 4.17. In addition, according to Eq. (2.1), parameter λ defines the exit angle of the wheel. As the wheels of Juno II have non-negligible flexibility, a rather large value of λ is selected to compensate for the effect of wheel flexibility. Furthermore, k_0 and k_0 are selected based on the values reported by Wong (2010) for sand.

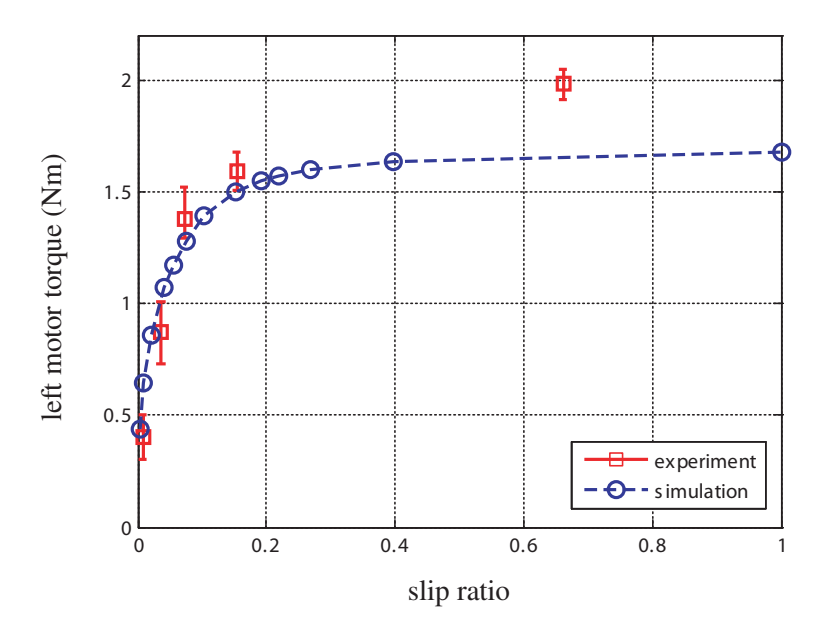


FIGURE 4.19. Comparing the driving torque of the left side motor obtained from experiments with the values obtained from simulation using the approach of Chapter 2 and the WRI model.

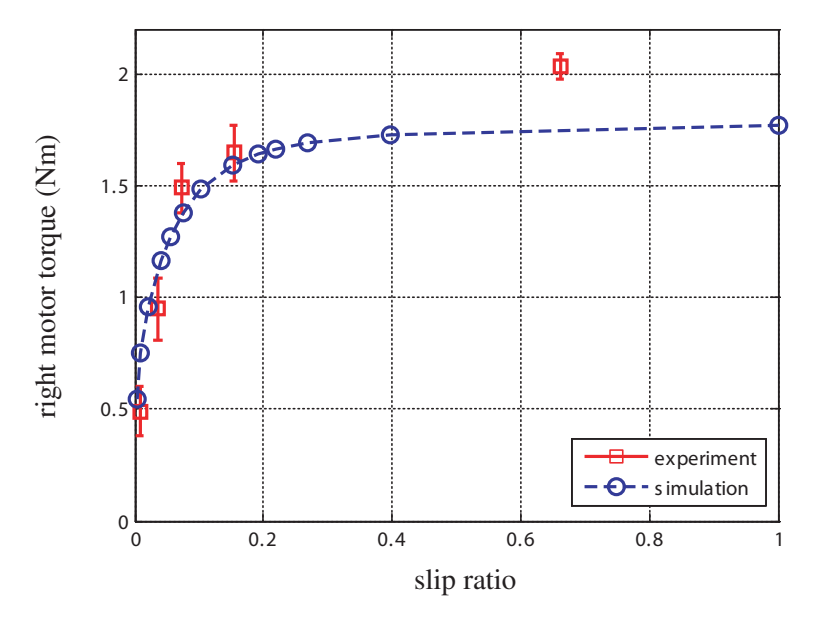


FIGURE 4.20. Comparing the driving torque of the right side motor obtained from experiments with the values obtained from simulation using the approach of Chapter 2 and the WRI model.

CHAPTER 4. EXPERIMENTAL INVESTIGATION AND ROVER SIMULATION

The comparison between the simulation and experiment for the drawbar pull and driving torque versus slip ratio are shown in Figs. 4.18–4.20. As can be seen from these figures, the simulation results can closely capture the experimental data. The experimental results for drawbar pull, Fig. 4.18, show that by slightly increasing the slip ratio, from around zero to around 8%, the drawbar pull almost reaches its maximum value. This suggests that the shear deformation modulus K_d for this soil should be very small, which results in selecting a very small value for K_d in our model, as reported in Table 4.1.

The results displayed in Figs. 4.19 and 4.20 also show an interesting behaviour for the driving torque requirement. As expected, in the no-drawbar pull test, which corresponds to a slip ratio of around zero, a non-negligible torque is required to drive the rover. This torque is needed to overcome the rolling resistance and the drive train friction. Overall, the results show that at low slip ratios, the simulation closely captures the experimental results, while at high slip ratios the model slightly under-estimates the torque requirements.

In addition, the drawbar pull experiments were repeated for the same rover, while its mass was increased by adding massive metallic disks to it. The rover with the added mass is shown in Fig. 4.21. The total added mass was 111.5 kg.



FIGURE 4.21. The rover with the added mass to its main frame.

The drawbar pull and the driving torque of this set of experiment were also compared with simulation results. In this case, the simulation setup was the same as the setup used

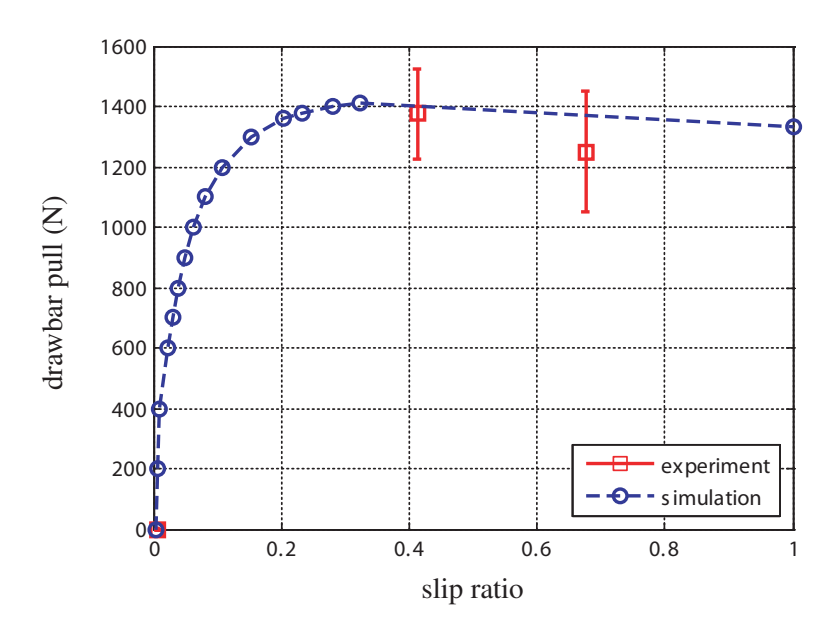


FIGURE 4.22. Comparing the drawbar pull obtained from experiments with the values obtained from simulation using the approach of Chapter 2 and the WRI model. The rover was heavier, as shown in Fig. 4.21.

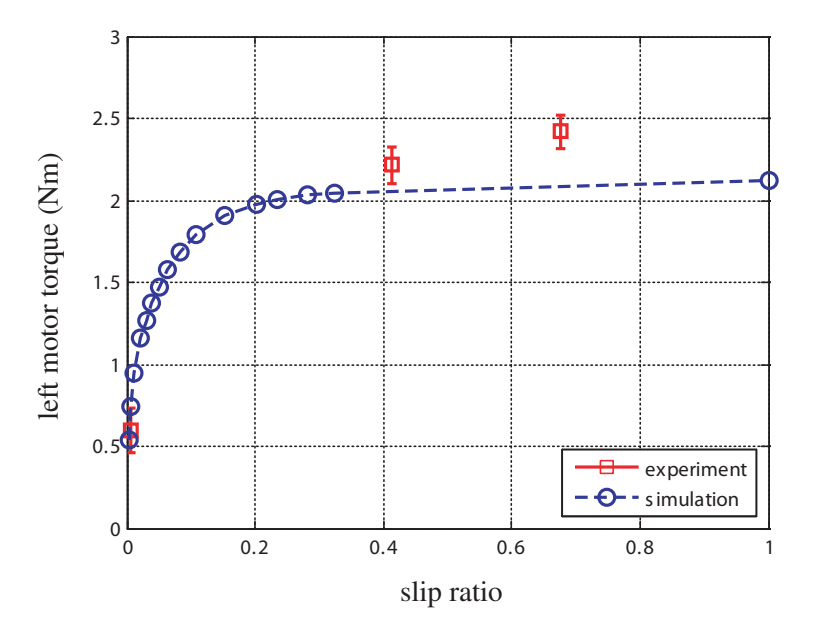


FIGURE 4.23. Comparing the driving torque of the left side motor obtained from experiments with the values obtained from simulation using the approach of Chapter 2 and the WRI model. The rover was heavier, as shown in Fig. 4.21.

for the previous test, except that the mass of the rover chassis was increased by 111.5 kg, and its other inertial properties were update accordingly.

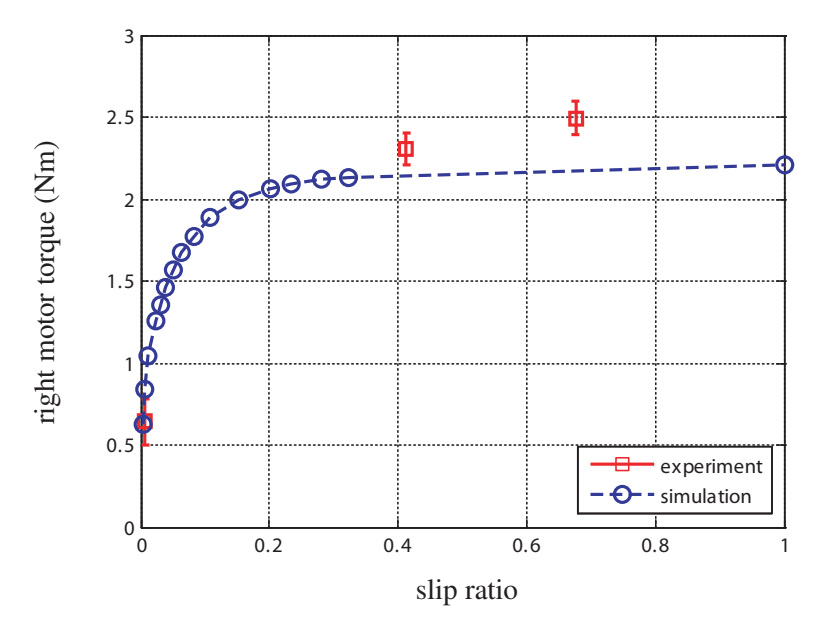


FIGURE 4.24. Comparing the driving torque of the right side motor obtained from experiments with the values obtained from simulation using the approach of Chapter 2 and the WRI model. The rover was heavier, as shown in Fig. 4.21.

The results are shown in Figs. 4.22–4.24. Apparently, the simulation results can closely represent the experimental data. This set of results is of particular interest, as it shows that the same model with the same parameters can appropriately represent the 35% heavier rover.

4.4.2 Comparison with the Elasto-plasticity Model

The model developed and described in Chapter 3 is used to simulate the interaction between the wheels of the rover and soil. The same sets of experiments were used to compare the simulation results against the experiments.

In order to use this model, both the Drucker-Prager soil parameters and α_1 , α_2 , and α_3 need to be determined. In this example, the parameters of the Drucker-Prager model were those used in Section 3.3, except for β , d, and Young's modulus. The α_i parameters

are also determined using the procedure explained in Section 3.3.4. The hardening data are those in Table 3.2, the rest of the parameters being displayed in Tables 4.2 and 4.3.

TABLE 4.2. Material properties for the elasto-plastic constitutive relation

Young's modulus, E (Pa)	8×10^5
Poisson's ratio, <i>v</i> (-)	0.32
Angle of friction, β (deg)	38
Material cohesion, d (Pa)	3161
Cap eccentricity, R_e (-)	0.15
Initial value for $\varepsilon_{\text{vol}}^p$ (-)	0.001
Transition surface parameter, α (-)	0.01

TABLE 4.3. Parameters of the proposed velocity field used in the elasto-plasticity model

$\alpha_1 (\mathrm{m}^{-1})$	α_2 (-)	$\alpha_3 (\mathrm{m}^{-1})$
3.5	0.045	100

The comparison between the simulation results and the experiments obtained with the Juno II without added mass are displayed in Figs. 4.25–4.27.

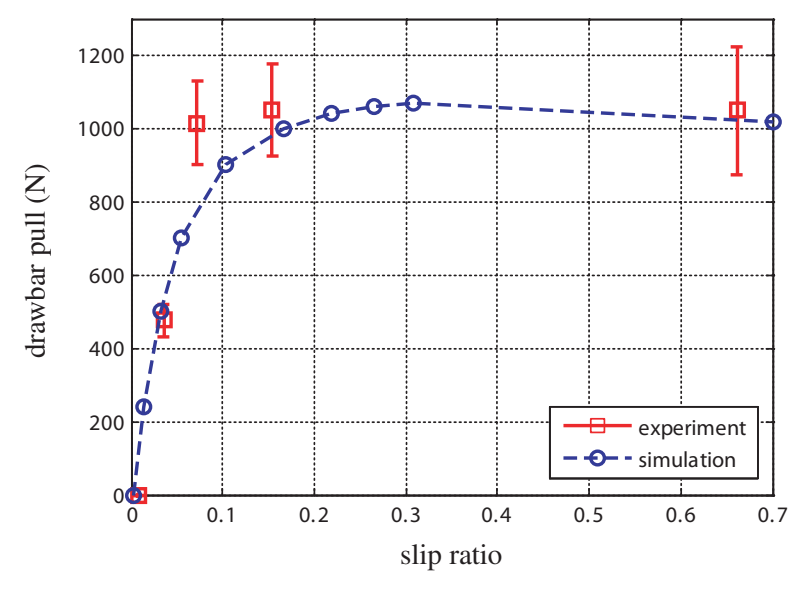


FIGURE 4.25. Comparing the drawbar pull obtained from experiments with the values obtained from simulation using the elasto-plasticity model.

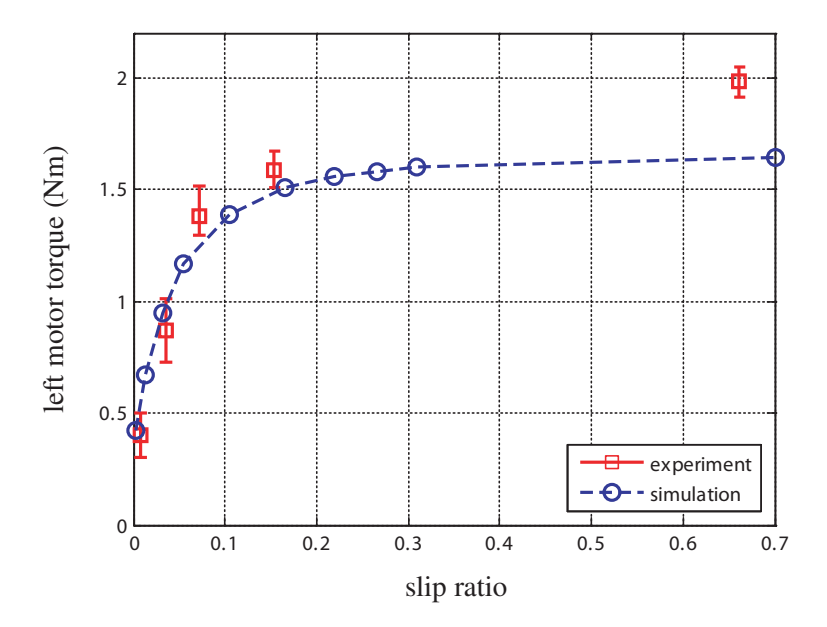


FIGURE 4.26. Comparing the driving torque of the left side motor obtained from experiments with the values obtained from simulation using the elasto-plasticity model.

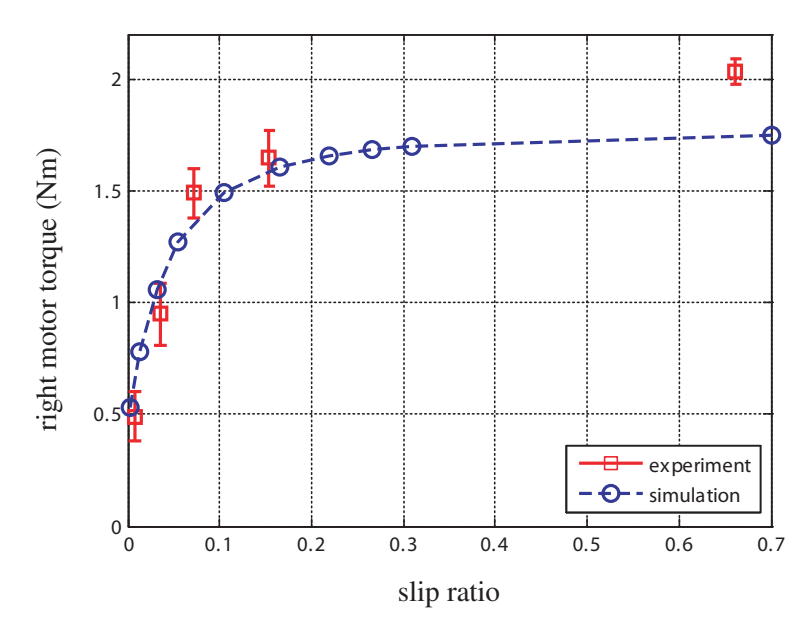


FIGURE 4.27. Comparing the driving torque of the right side motor obtained from experiments with the values obtained from simulation using the elasto-plasticity model.

As can be seen in Fig. 4.25, the drawbar pull determined using the model developed for Juno II with the elasto-plastic wheel-soil interaction model can closely capture the experimental results. According to the simulation results, the drawbar pull increases rapidly with the slip ratio from zero to 10% slip ratio. Then, the drawbar pull increases at a slower pace up to around 30% of slip ratio. After that, the drawbar pull decreases slightly upon increasing the slip ratio. The driving torque results displayed in Figs. 4.26 and 4.27 also show a good match between simulation and experiments.

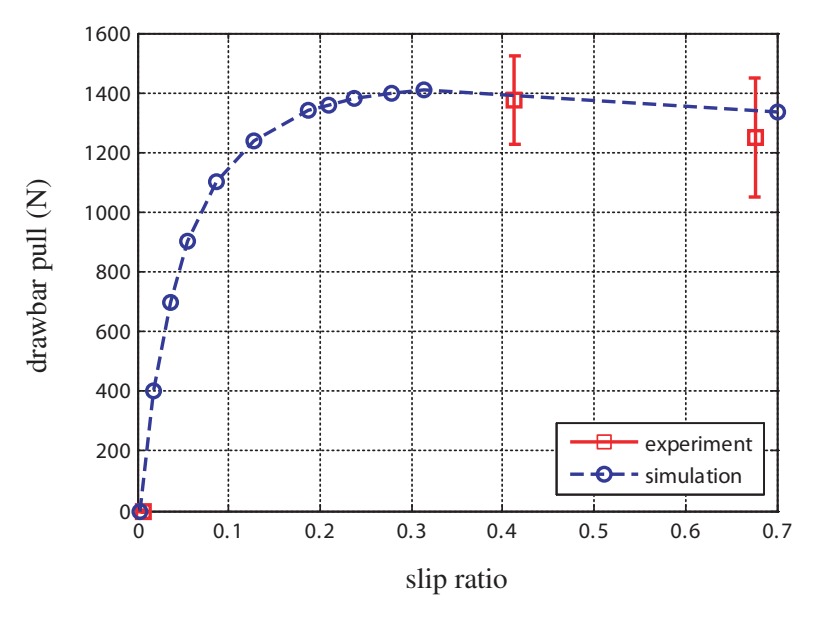


FIGURE 4.28. Comparing the drawbar pull obtained from experiments with the values obtained from simulation using the elasto-plasticity model. The rover was heavier, as shown in Fig. 4.21.

In addition, the experimental results obtained from a rover with the added mass are compared with the simulation results obtained from using the elasto-plasticity model; the results are displayed in Figs. 4.28–4.30.

As can be seen from Figs. 4.28–4.30, the simulation results closely capture the experimental data, which further validates the scalability of the elasto-plasticity-based model, with the 35% heavier rover. This was the behaviour expected from this model, as the experimental investigation explained in Section 3.4 represented this feature of the model.

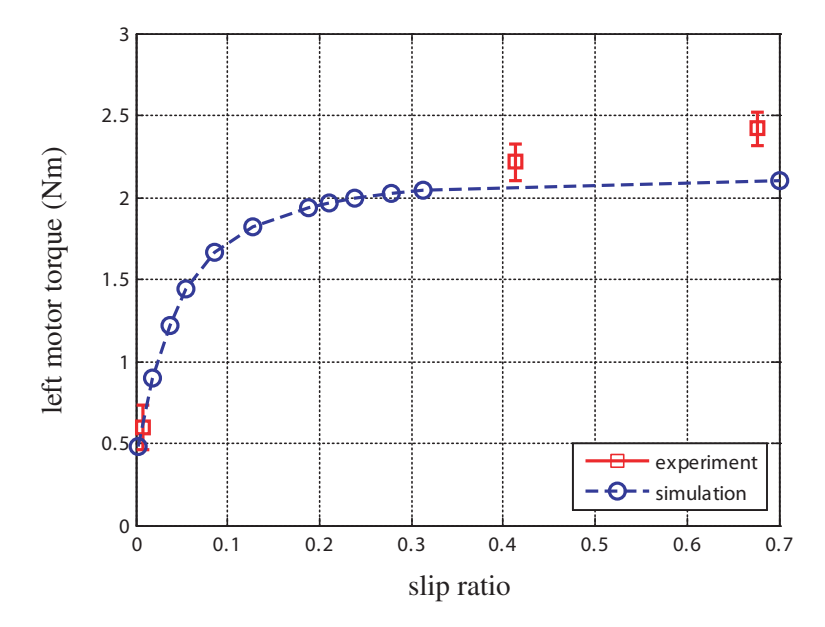


FIGURE 4.29. Comparing the driving torque of the left side motor obtained from experiments with the values obtained from simulation using the elasto-plasticity model. The rover was heavier, as shown in Fig. 4.21.

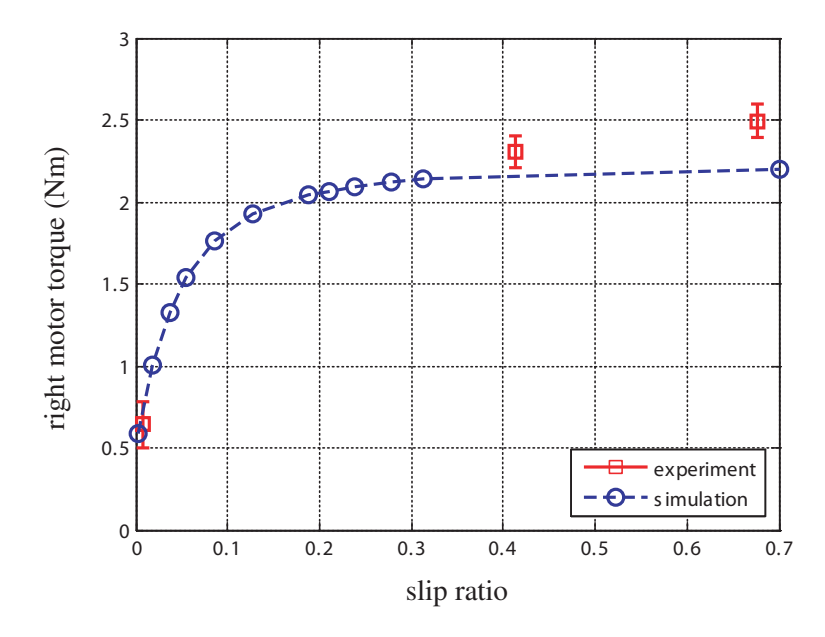


FIGURE 4.30. Comparing the driving torque of the right side motor obtained from experiments with the values obtained from simulation using the elasto-plasticity model. The rover was heavier, as shown in Fig. 4.21.

In addition, Fig. 4.28 shows that the drawbar pull decreases when the slip ratio increases from around 42% to around 68%. The simulation also shows a reduction in the drawbar pull when the slip ratio increases from around 32% to 70%. While the torque requirements have increased constantly with the slip ratio (Figs. 4.29 and 4.30), the drawbar pull does not show the same pattern, as mentioned above. This result can be explained by looking at the elasto-plasticity model, as discussed in detail in Chapter 3: increasing the slip ratio causes the slip-sinkage effect. Increasing the sinkage, in turn, could increase the rolling resistance R_c . Increasing the slip ratio will also increase the traction force. Therefore, depending on the type of soil and loading condition, when the slip ratio increases, one could see two phases in the drawbar pull behaviour. In the first phase, the drawbar pull increases and then may reach a constant value. In this phase, the increase in the traction force is higher than the increase in the resistance, which results in the positive gain in the drawbar pull. Then, by further increasing the slip ratio, in the second phase, the drawbar pull may show a decrease. This is because of excessive slip-sinkage happening at high slip ratios, which causes higher increase rate in the resistance than the traction force. However, during the entire range of slip ratio, the resistance torque increases with the slip ratio.

4.5 Motion on an Irregular Surface

In this experiment, the rover is operated on irregular terrain made of uncompacted soft soil. The developed multi-body model of the rover, explained in Sections 4.2 and 4.3, is used with the wheel-soil interaction models and frameworks, explained in Chapters 2 and 3, to simulate the rover motion associated with this experiment.

For this case, the terrain was scanned using a LIDAR system. The raw data from the LIDAR scan are displayed in Fig. 4.31. The LIDAR data are used to create the terrain profile compatible with the simulation setup, which is a height-field. This height-field uses a fixed 0.04 m grid size in this example.



FIGURE 4.31. LIDAR scan of the test area



FIGURE 4.32. Location of the rover on the terrain before starting the experiment.

The location of the rover before starting this experiment is shown in Figs. 4.32 and 4.33, which is different from its location shown in the LIDAR scan (Fig. 4.31). The reason is that the rover was moved to its initial location after taking the LIDAR scan of the test area, in order to have the proper information of the terrain surface used on the experiment. It is

noted that the terrain under the rover cannot be scanned, as the rover blocks the line of sight of the LIDAR scanner. The location of the rover and its heading direction, however, was approximately determined from the measurements and the pictures taken before starting the test.

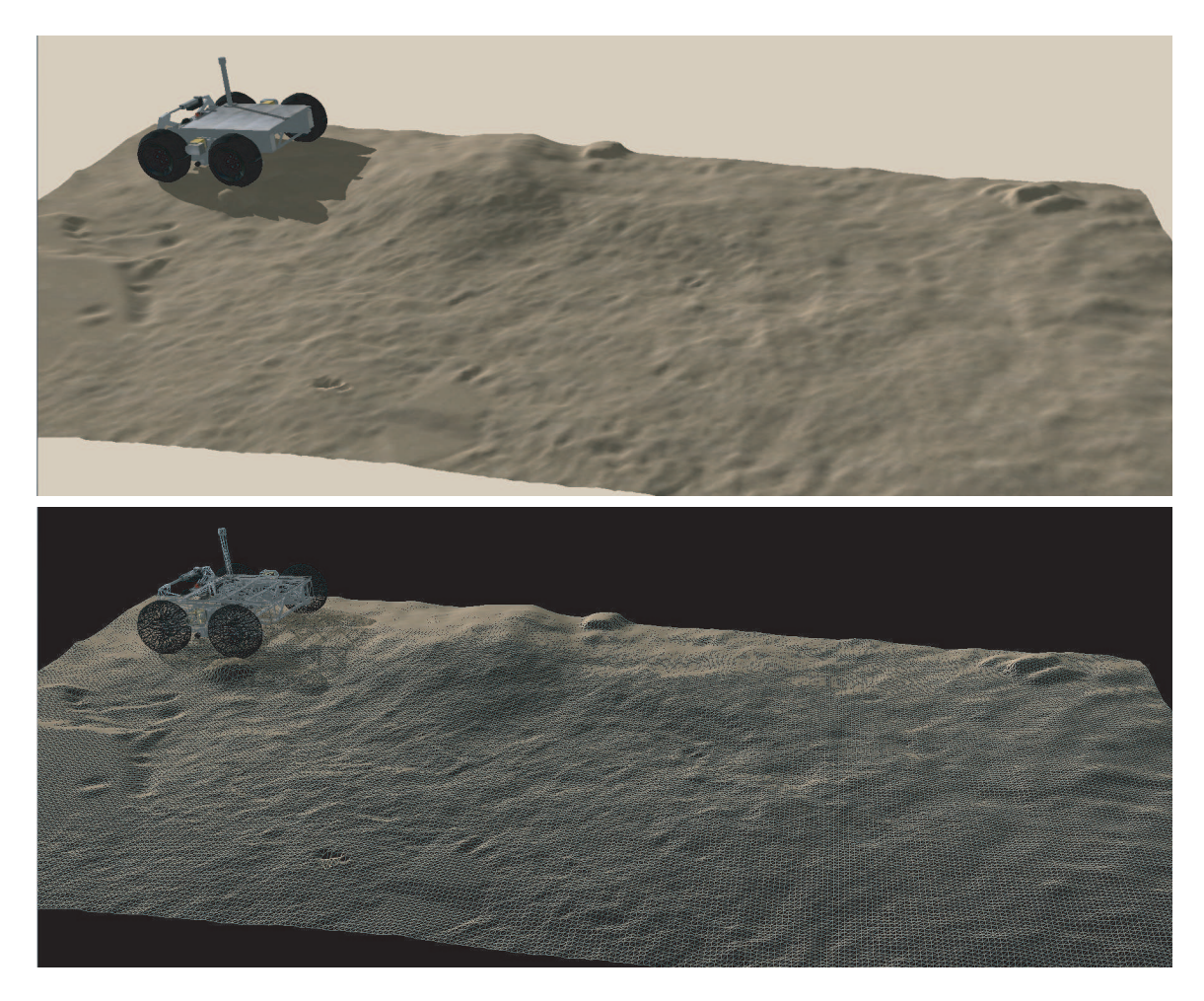


FIGURE 4.33. The height-field terrain prepared using the LIDAR scan data, with the initial location of the rover.

The terrain profile used in the simulation and the location of the rover before starting the simulation are displayed in Fig. 4.33. During simulation, the rover was commanded by the same angular velocity profile that was obtained from the experiments. However, the angular velocities obtained from the experiments were first filtered. The original angular velocities and the filtered data are shown in Figs. 4.34 and 4.35.

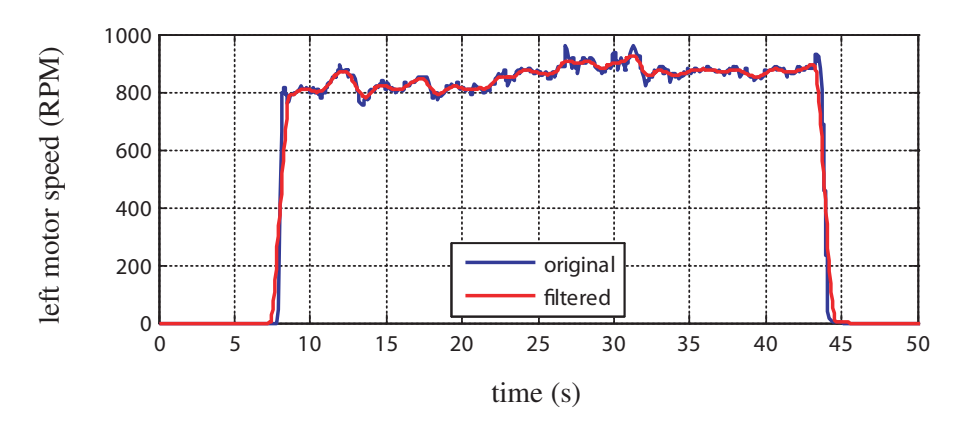


FIGURE 4.34. The angular velocity of the left motor obtained from the experiment and the filtered value used in the simulation.

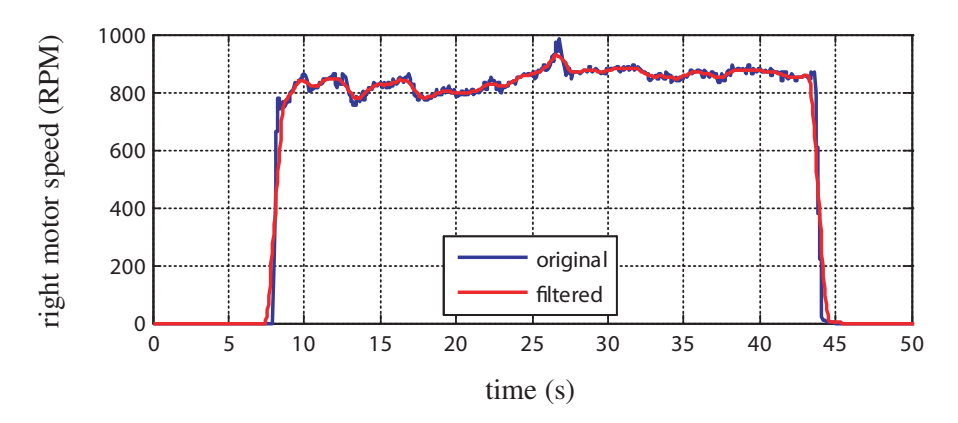


FIGURE 4.35. The angular velocity of the right motor obtained from the experiment and the filtered value used in the simulation.

The trajectory of the reflector prism, which was attached to the rover chassis, was recorded during the experiment. This trajectory is compared with that obtained from the simulation runs. In addition, the driving torque and the energy consumption are compared with the experiments.

Similar to the results of drawbar pull experiments discussed in Section 4.4, the experimental outcomes are first compared with the simulation results obtained when using the WRI model, which was implemented in *Vortex* based on the approach explained in Chapter 2. The results are displayed in Figs. 4.36–4.40.

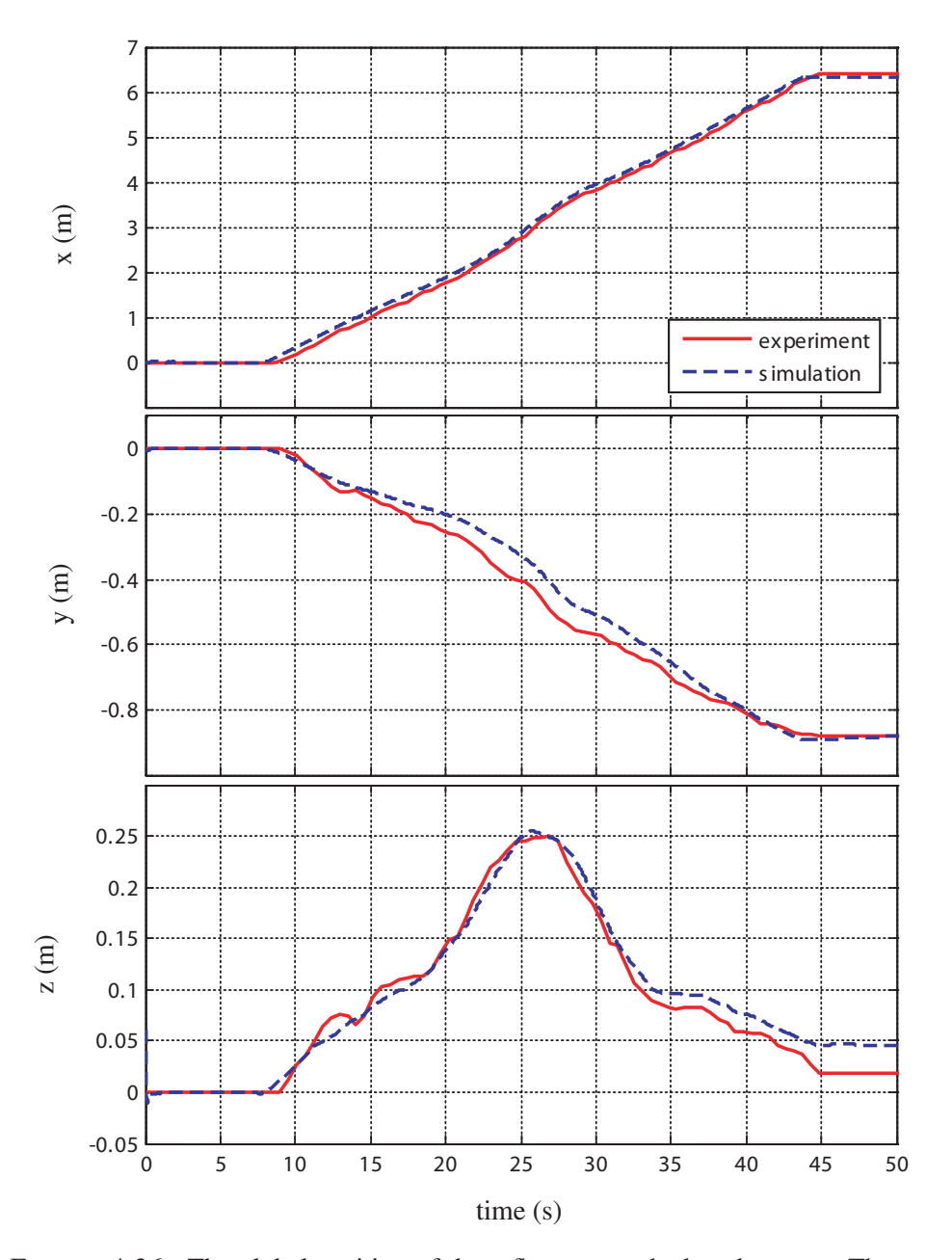


FIGURE 4.36. The global position of the reflector, attached to the rover. The experimental results are compared with the values obtained from simulation using the semi-empirical model.

As can be seen from Fig. 4.36, the rover trajectory, which was obtained by tracking the reflector prism attached to its chassis, is captured with very good accuracy. In the experiment, the rover has mainly moved along the *x*-axis. This motion is accurately represented in the simulation, as shown in Fig. 4.36. During the experiment, the rover climbs a small

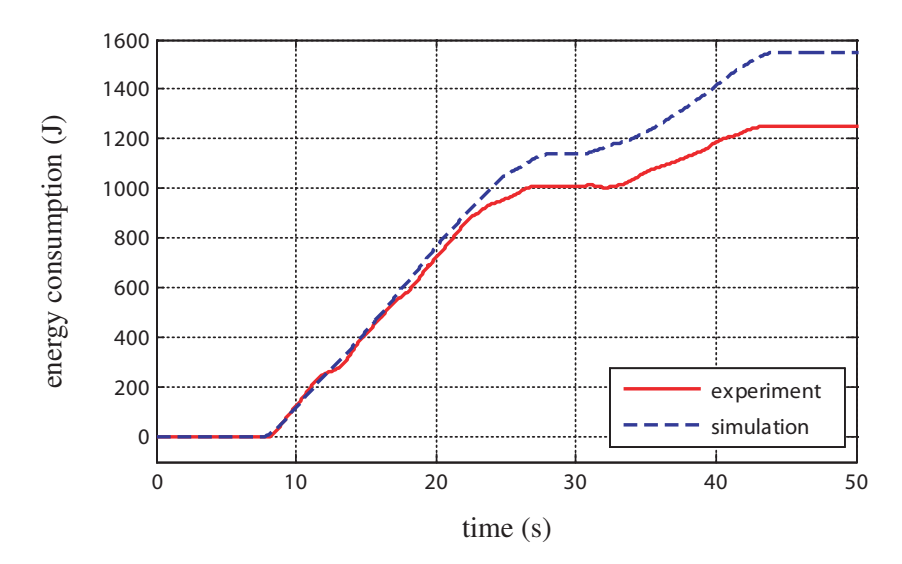


FIGURE 4.37. The energy expenditure of the left side motor. The experimental results are compared with the values obtained from simulation using the semi-empirical model.

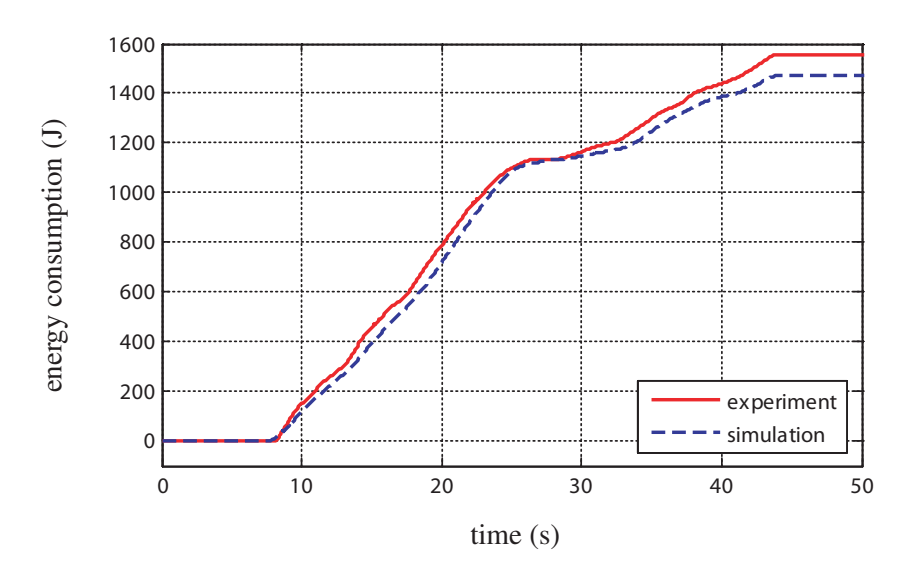


FIGURE 4.38. The energy expenditure of the right side motor. The experimental results are compared with the values obtained from simulation using the semi-empirical model.

dune, as shown in Fig. 4.33. The motion in the z-axis, shown in Fig. 4.36, represents the climbing of and then descending from the dune over time.

Furthermore, the energy expenditure is shown in Figs. 4.37 and 4.38. The energy expenditure is determined based on the power consumption of the motors. The latter is

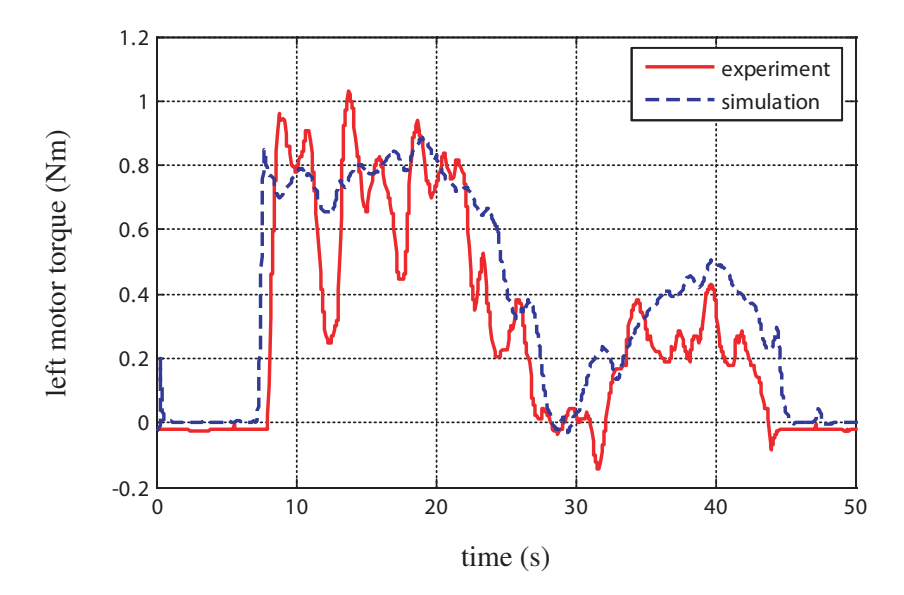


FIGURE 4.39. The driving torque of the left side motor. The experimental results are compared with the values obtained from simulation using the semi-empirical model.

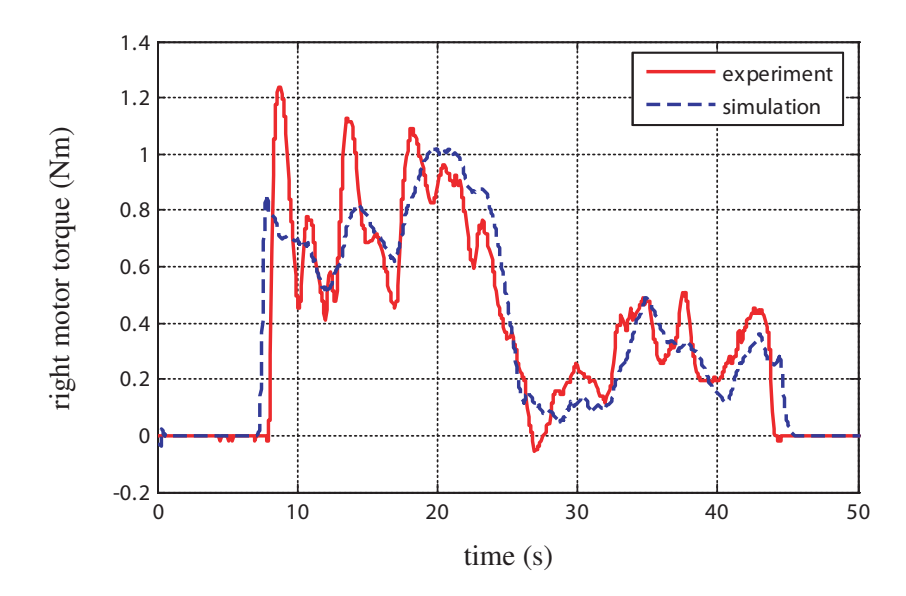


FIGURE 4.40. The driving torque of the right side motor. The experimental results are compared with the values obtained from simulation using the semi-empirical model.

determined from multiplying the motor torque by its angular velocity. Overall, the simulation results are acceptable with some drift observed in the results of the left motor. The reason for a lower accuracy in the result of the left wheel could be related to inaccuracy in

the scanned terrain data. As can be seen from Figs. 4.31 and 4.33, the LIDAR scanner is placed in the right side of the rover test area. This makes the scanner to be closer to the terrain areas that come in contact with the right-side wheels of the rover, and therefore, lead to a higher accuracy in the scanned surface.

Moreover, the driving torque obtained from simulation is compared with experiments, as shown in Figs. 4.39 and 4.40. In both figures, the experiments show more variation than the simulation. The rather small oscillations in the driving torques obtained from simulation are related to our implementation explained in Section 2.4.5. As explained there, the terrain under each wheel is approximated by a plane obtained using a least-squares approximation. This approach, basically, filters out some of the irregularities in the terrain.

The elasto-plasticity model explained in Chapter 3 with the model parameters shown in Tables 4.2 and 4.3 is also used to simulate this motion of the rover. The results are displayed in Figs.4.41–4.45.

As can be seen from Fig. 4.41, the trajectory of the rover was also captured with good accuracy with using this novel model. Furthermore, the comparison between the energy expenditure, as shown in Figs. 4.42 and 4.43, shows a similar pattern to what was observed in Figs. 4.37 and 4.38. Moreover, the simulation results regarding the driving torque of both motors versus time are compared with the experimental results, as shown in Figs. 4.44 and 4.45. The results in Figs. 4.44 and 4.45 show considerable oscillation in the torque requirement determined from the simulation. This behaviour can be explained by recalling Section 3.5: in the elasto-plasticity model implementation, the least-squares plane is only used to determine the normal direction of the plane locally under the wheel, but the active vertices used in Algorithm 2 are determined directly from the height-field vertices. That is, the terrain irregularities are not filtered, which, in turn, leads to a higher variation in the simulation results.

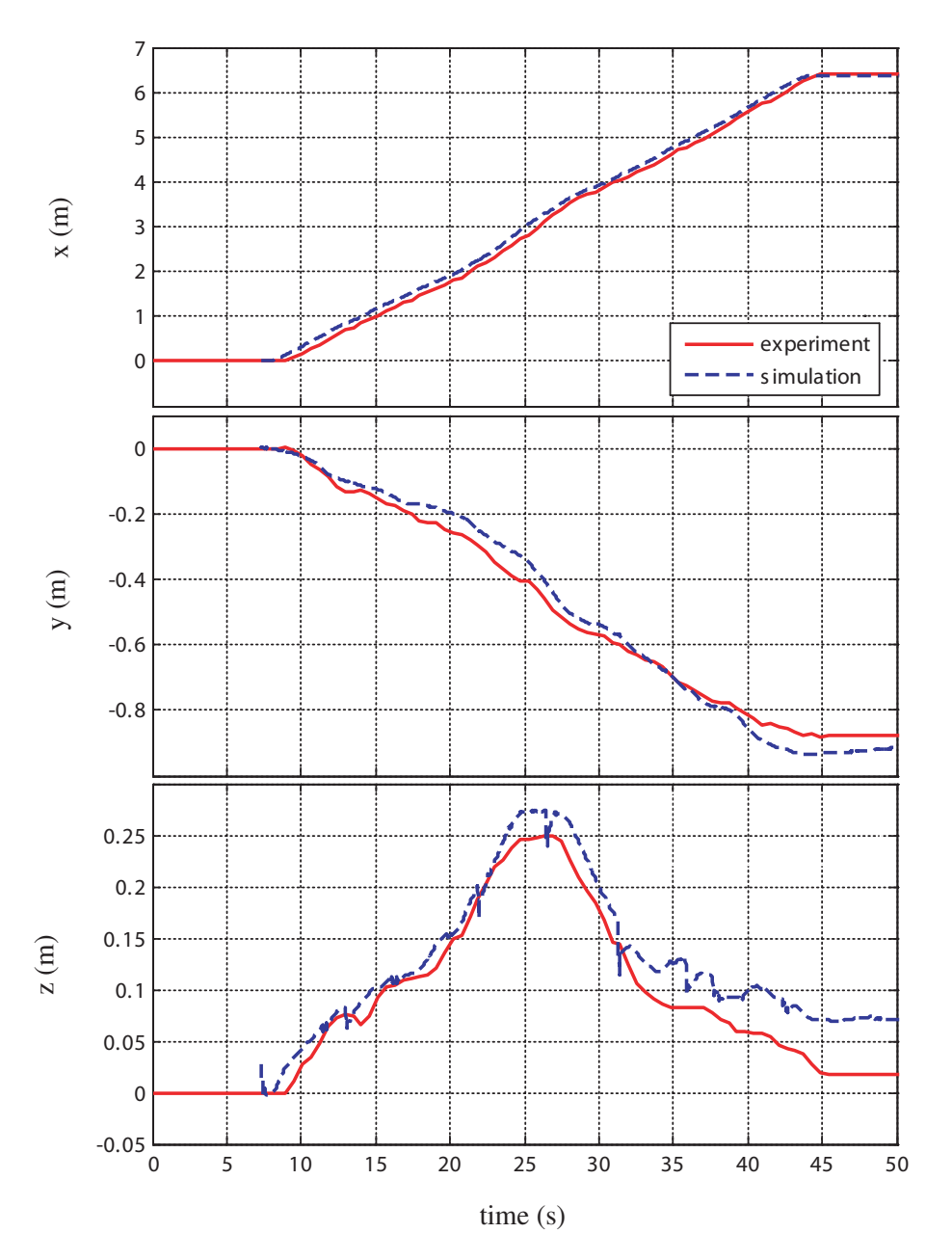


FIGURE 4.41. The global position of the reflector, attached to the rover. The experimental results are compared with the values obtained from simulation using the elasto-plasticity model.

It should be mentioned that the wheel slippage seen during motion was relatively small, and the slip ratio was below 10%. This could be the main reason for having a very good match between simulation and experiment in the total travelled distance. Had the rover

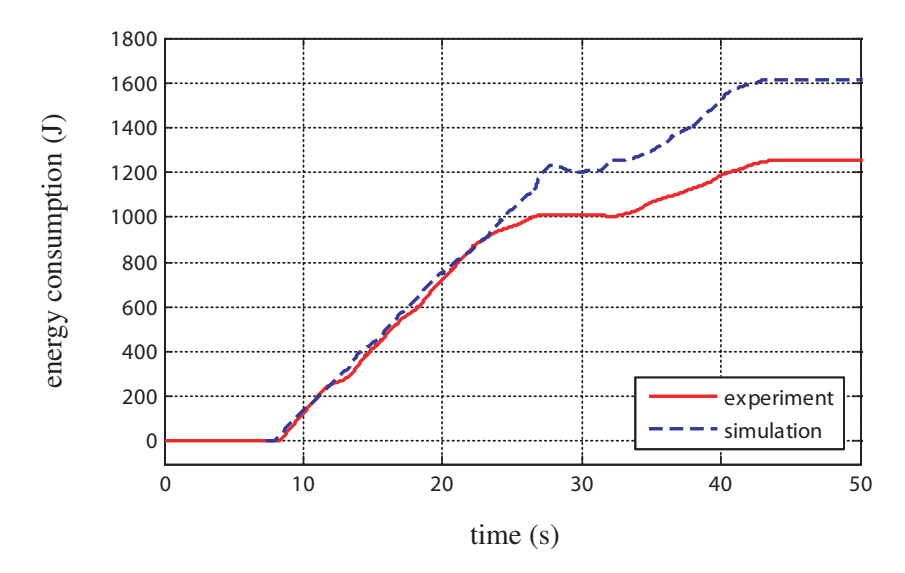


FIGURE 4.42. The energy expenditure of the left side motor. The experimental results are compared with the values obtained from simulation using the elastoplasticity model.

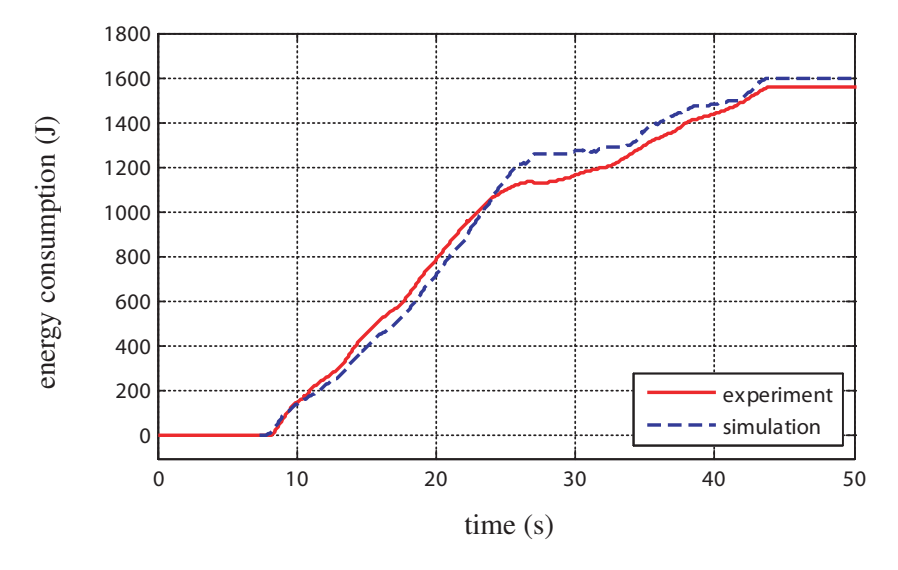


FIGURE 4.43. The energy expenditure of the right side motor. The experimental results are compared with the values obtained from simulation using the elastoplasticity model.

operated with higher slip, the results could have shown larger differences between experiment and simulation, in terms of the rover trajectory. The reason for this behaviour lies in that, in both experimental and simulation results, as shown in Figs. 4.18 and 4.25, when the

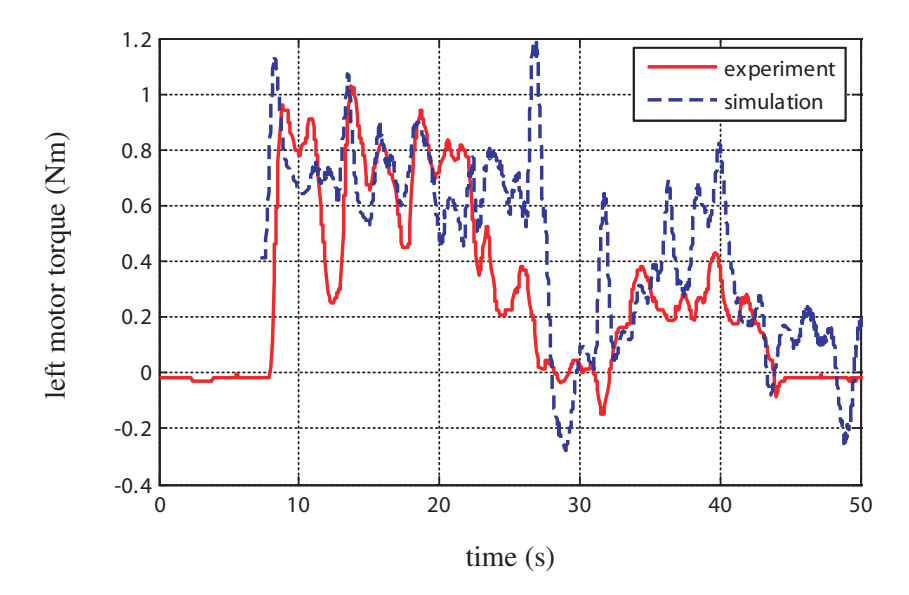


FIGURE 4.44. The driving torque of the left side motor. The experimental results are compared with the values obtained from simulation using the elasto-plasticity model.

slip ratio is around 20% and higher, the drawbar pull does not significantly change under significant changes in the slip ratio.

The energy expenditure determined from simulation runs using both models also shows a relatively good match compared to the experiments. As energy expenditure is an important aspect in mission planning of rovers, the simulations can be very helpful in this regard as well.

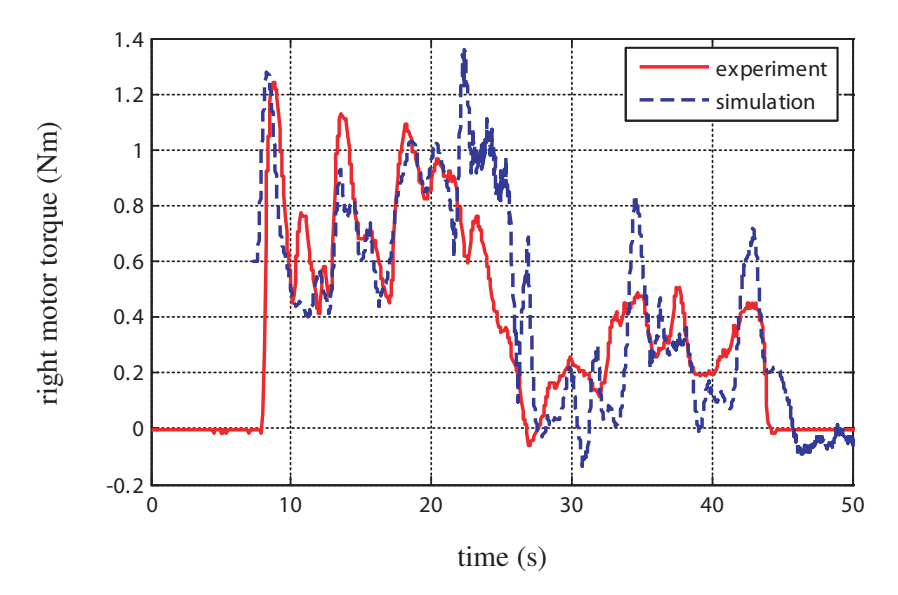


FIGURE 4.45. The driving torque of the right side motor. The experimental results are compared with the values obtained from simulation using the elasto-plasticity model.

CHAPTER 5

Conclusions and Recommendations for Future Work

5.1 Thesis Contributions

In this thesis two modelling approaches for wheel-soil interaction were introduced. The first approach, presented in Chapter 2, is based on widely used semi-empirical terramechanics models. In order to implement the semi-empirical terramechanics models in a multi-body dynamics simulation environment, a novel framework was developed. As shown in Chapter 2, using this framework, a multi-body dynamics model combined with semi-empirical terramechanics relations can be formulated as a mixed linear complementarity problem. With this formulation, fast and real-time simulation of rovers on irregular terrain was achieved. It was shown through simulation and experimental verification that this model is capable of producing realistic simulated behaviour even on non-planar, rough terrain. In this implementation, the terrain is represented as a high resolution height-field data structure, which deforms under wheel-induced soil compaction. To deal with motion on rough terrain, we developed an efficient scheme in approximating the contact area using a least-squares technique. The method captures wheel-induced soil deformation and hardening, which results in the multi-pass effect.

In Chapter 3, we introduced a novel approach in representing the interaction between wheel and soil that allows for efficient dynamics modelling, simulation and analysis of rovers, and provides a theoretical framework in wheel-soil interaction. In this approach, elasto-plasticity theory is employed in order to determine the stress field in the contact area. A velocity field is proposed for the motion of soil particles in the vicinity of the contact region. Using this velocity field and the Drucker-Prager constitutive relation for soil, the stress field in the contact area is determined incrementally using an explicit integration scheme explained in Algorithm 2. In this approach, the soil plastic deformation and energy loss due to this deformation are captured. In addition, elastic rebound of soil is determined using Algorithm 3. The proposed approach is modular in that it does not have to be used with the Drucker-Prager constitutive relation and the proposed velocity field. Any elasto-plastic constitutive relation and other possible velocity-field representations can be used in this framework, if needed, to more closely capture the behaviour of different soil types.

As discussed in detail in Chapter 3, the results are in good agreement with experimental data available in the literature and with results that can be obtained based on semi-empirical terramechanics models. The proposed model, however, goes beyond the semi-empirical terramechanics models and is compatible with multibody dynamics environments. Energy dissipation due to soil plastic deformation is directly represented in our model. In addition, the slip-sinkage phenomenon is captured by the model as a natural outcome. The processing time required for the computation of soil response using the proposed model is much shorter than that required by FEA, and its implementation is readily parallelizable. Therefore, the framework introduced here allows for fast and even real-time simulation of rovers on soft soil, while a high-fidelity elasto-plastic constitutive relation can be used for soil. In addition, the model has the capability of covering a broad range of motion possibilities that can happen under general motion conditions.

In Chapter 4, the models developed in the thesis are used to perform rover simulation. The simulation results are compared against an extensive set of experiments conducted with the Juno II rover. In this chapter, the multi-body model of the rover developed in *Vortex* was discussed in detail. Three sets of experiments were conducted and reported in this chapter. The first set was performed on horizontal, flat concrete floor and on a metallic incline, in order to determine rover properties. The second set of experiments was conducted on soft, uncompacted soil with a horizontal flat surface, in which the drawbar pull of the rover was measured at various ranges of wheel slippage. The experiments were repeated for the rover with added mass.

Operation on irregular terrain was the scope of the last set of experiments in Chapter 4. In this case, the terrain surface was scanned using a LIDAR scanner, before operating the rover on it. Using the LIDAR data, a height-field terrain was generated in *Vortex*. In the simulation, the wheels of the rover were commanded with the same angular velocities that were obtained based on measurements during experiments. The rover trajectory, motor torques, and the energy expenditure obtained from simulation were compared with experimental data.

5.2 Recommendations for Future Work

The model developed in Chapter 3, based on elasto-plasticity theory, provides a novel framework for studying wheel and soil interaction. We explained the model and all its essential components in the thesis. As with almost any new idea, a number of investigations can be conducted to assess its performance and achieve even further improvements.

The two main parts of the model that can be further investigated are the proposed velocity field and the elasto-plastic constitutive relation. The assumed velocity field was discussed in Subsection 3.3.4. Experimental observation of soil particle motion under a wheel can shed light on how the velocity field can be further developed, if needed, in order

to more closely capture any specific type of soil and wheel motion. This type of experiments has been recently reported by Senatore et al. (2012) at MIT. Similar experiments are also being conducted at Carnegie Mellon University (Skonieczny et al., 2012). It should be mentioned that one of the important issues that needs to be investigated is the effect of terrain slope on the velocity field.

Moreover, the use of alternative elasto-plastic soil models, depending on the type of soil, can be investigated. For example, the models proposed by Manzari and Dafalias (1997) and Taiebat and Dafalias (2008) can be good candidates for operations on sand. These models capture both hardening and softening behaviour in sand, their numerical implementations are relatively straightforward, and they are computationally efficient.

Regarding semi-empirical models, extra effort in modelling lateral forces is needed. In this regard, capturing the changes in soil surface induced from the soil bulldozed by the wheel sidewall can be an interesting direction for future investigation. In addition, as mentioned in the thesis, the recent findings of Ding et al. (2011b) suggest that in the case of a large angle ρ_w between wheel-sidewall and soil surface, the approximation of the failure pattern using two wedges leads to more acceptable results, when compared with the single-wedge model of McKyes (1985). This finding is worth further investigation. Moreover, additional experimental investigation on inclined soil surfaces can be beneficial. In this regard, inclined single-wheel testbeds can be employed.

BIBLIOGRAPHY

- V. Acary and B. Brogliato. *Numerical Methods for Nonsmooth Dynamical Systems. Applications in Mechanics and Electronics*, volume 35 of *Lecture notes in applied and computational mechanics*. Springer, 2008.
- AESCO. Matlab/Simulink Module AS²TM User's Guide, 2005.
- M. Anitescu and F. A. Potra. Formulating dynamic multi-rigid-body contact problems with friction as solvable linear complementarity problems. *Nonlinear Dynamics*, 14:231–247, 1997.
- A. Azimi, M. Hirschkorn, B. Ghotbi, J. Kövecses, J. Angeles, P. Radziszewski, M. Teichmann, M. Courchesne, and Y. Gonthier. Simulation-based rover performance evaluation and effects of terrain modelling. In *15th CASI Astronautics Conference ASTRO*, 2010.
- A. Azimi, M. Hirschkorn, B. Ghotbi, J. Kövecses, J. Angeles, P. Radziszewski, M. Teichmann, M. Courchesne, and Y. Gonthier. Terrain modelling in simulation-based performance evaluation of rovers. *Canadian Aeronautics and Space Journal*, 57:24–33, 2011a.
- A. Azimi, J. Kövecses, and J. Angeles. Wheel-soil interaction modelling for dynamics simulation of rovers. In *CCToMM Symposium on Mechanisms, Machines, and Mechatronics*, 2011b. (Extended abstract only).
- A. Azimi, J. Kövecses, and J. Angeles. Wheel-soil interaction model for rover simulation based on plasticity theory. In *IEEE/RSJ Int. Conf. Intelligent Robots and Systems (IROS)*,

- pages 280-285, San Francisco, USA, September 2011c.
- A. Azimi, D. Holz, J. Kövecses, J. Angeles, and M. Teichmann. Efficient dynamics modeling for rover simulation on soft terrain. In *50th AIAA Aerospace Sciences Meeting*, pages 1–9, Nashville, USA, January 2012.
- A. Azimi, D. Holz, J. Kövecses, J. Angeles, and M. Teichmann. Wheel-terrain interaction modelling for dynamics simulation and analysis of wheeled mobile robots. In *CCToMM Symposium on Mechanisms, Machines, and Mechatronics*, 2013a. (Extended abstract only).
- A. Azimi, J. Kövecses, and J. Angeles. Wheel-soil interaction model for rover simulation and analysis using elasto-plasticity theory. *IEEE Transactions on Robotics*, 29(5):1271–1288, 2013b.
- R. Bauer, W. Leung, and T. Barfoot. Development of a dynamic simulation tool for the exomars rover. In *Proc. 8th Int. Symp. on Artificial Intelligence, Robotics and Automation in Space, iSAIRAS*, Munich, Germany, Aug. 2005.
- R. Bauer, T. Barfoot, W. Leung, and G. Ravindran. Dynamic simulation tool development for planetary rovers. *Int. J. Advanced Robotic Systems*, 5(3):311–314, 2008.
- M. G. Bekker. *Theory of Land Locomotion*. Ann Arbor, The University of Michigan Press, 1956.
- M. G. Bekker. *Introduction to Terrain-Vehicle Systems*. Ann Arbor, The University of Michigan Press, 1969.
- R. C. Chiroux, W. A. Foster, C. E. Johnson, S. A. Shoop, and R. L. Raper. Three-dimensional finite element analysis of soil interaction with a rigid wheel. *Applied Mathematics and Computation*, 162:707–722, 2005.
- E. A. de Souza Neto, D. Perić, and D. R. J. Owen. *Computational Methods for Plasticity: Theory and Applications*. John Wiley & Sons, 2008.
- L. Ding, H. Gao, Z. Deng, and J. Tao. Wheel slip-sinkage and its prediction model of lunar rover. *Journal of Central South University of Technology*, 17:129–135, 2010a.

- L. Ding, K. Nagatani, K. Sato, A. Mora, K. Yoshida, H. Gao, and Z. Deng. Terramechanics-based high-fidelity dynamics simulation for wheeled mobile robot on deformable rough terrain. In *IEEE International Conference on Robotics and Automation*, 2010b.
- L. Ding, H. Gao, Z. Deng, K. Nagatani, and K. Yoshida. Experimental study and analysis on driving wheels' performance for planetary exploration rovers moving in deformable soil. *J. Terramechanics*, 48:27–45, 2011a.
- Y. Ding, N. Gravish, and D. I. Goldman. Drag induced lift in granular media. *Phys. Rev. Lett.*, 106(2):028001, Jan 2011b.
- C. W. Fervers. Improved FEM simulation model for tire-soil interaction. *J. Terramechanics*, 41:87–100, 2004.
- K. Fukami, M. Ueno, K. Hashiguchi, and T. Okayasu. Mathematical models for soil displacement under a rigid wheel. *J. Terramechanics*, 43:287–301, 2006.
- D. Gee-Clough. The bekker theory of rolling resistance amended to take account of skid and deep sinkage. *J. Terramechanics*, 13(2):87–105, 1976.
- J. P. Hambleton and A. Drescher. Modeling wheel-induced rutting in soils: Indentation. *J. Terramechanics*, 45(6):201–211, 2008.
- J. P. Hambleton and A. Drescher. Modeling wheel-induced rutting in soils: Rolling. *J. Terramechanics*, 46(2):35–47, 2009.
- E. Hegedus. A simplified method for the determination of bulldozing resistance. Technical report, Land Locomotion Research Laboratory, Army Tank Automotive Command, 1960. Technical Report, no. 61.
- S. Helwany. Applied soil mechanics: with ABAQUS applications. Wiley, 2007.
- K. Hunt and F. Crossley. Coefficient of restitution interpreted as damping in vibroimpact. *Applied Mechanics*, 42:440–445, 1975.
- S. Hutangkabodee, Y. Zweiri, L. Seneviratne, and K. Althoefer. Soil parameter identification and driving force prediction for wheel-terrain interaction. *Int. J. Advanced Robotic Systems*, 5(4):425–432, 2008.

- K. Iagnemma and S. Dubowsky. Traction control of wheeled robotic vehicles in rough terrain with application to planetary rovers. *The Int. J. Robotics Research*, 23(10-11): 1029–1040, October-November 2004.
- K. Iagnemma, S. Kang, H. Shibly, and S. Dubowsky. Online terrain parameter estimation for wheeled mobile robots with application to planetary rovers. *IEEE Transactions on Robotics*, 20(5):921–927, October 2004.
- K. D. Iagnemma. *Rough-Terrain Mobile Robot Planning and Control with Application to Planetary Exploration*. PhD thesis, Massachusetts Institute of Technology, 2001.
- G. Ishigami, A. Miwa, K. Nagatani, and K. Yoshida. Terramechanics-based model for steering maneuver of planetary exploration rovers on loose soil. *J. Field Robotics*, 24(3): 233–250, 2007.
- G. Ishigami, G. Kewlani, and K. Iagnemma. Predictable mobility a statistical approach for planetary surface exploration rovers in uncertain terrain. *IEEE Robotics & Automation Magazine*, 16(4):61–70, 2009. ISSN 1070-9932.
- Z. Janosi and B. Hanamoto. Analytical determination of drawbar pull as a function of slip for tracked vehicles in deformable soils. In *First Int. Conf. on Terrain-Vehicle Systems*, Turin, Italy, 1961.
- B. Jeremić, Z. Yang, Z. Cheng, G. Jie, K. Sett, M. Taiebat, M. Preisig, N. Tafazzoli, and P. Tasiopoulou. Lecture Notes on Computational Geomechanics: Inelastic Finite Elements for Pressure Sensitive Materials. Computational Geomechanics Group, University of California Davis, November 2010.
- Z. Jia, W. Smith, and H. Peng. Fast analytical models of wheeled locomotion in deformable terrain for mobile robots. *Robotica*, pages 1–19, 2012. doi: http://dx.doi.org/10.1017/S0263574712000069.
- L. L. Karafiath. Plasticity theory and the stress distribution beneath wheels. *J. Terrame-chanics*, 8(2):49–60, 1971.

- L. L. Karafiath and E. A. Nowatzki. *Soil Mechanics for Off-Road Vehicle Engineering*. Trans Tech Publications, 1978.
- A. S. Khan and S. Huang. Continuum Theory of Plasticity. John Wiley and Sons, 1995.
- C. H. Liu and J. Y. Wong. Numerical simulations of tire-soil interaction based on critical state soil mechanics. *J. Terramechanics*, 33(5):209–221, 1996.
- C. H. Liu, J. Y. Wong, and H. A. Mang. Large strain finite element analysis of sand: model, algorithm and application to numerical simulation of tire-sand interaction. *Computers and Structures*, 74:253–265, 2000.
- J. Maciejewski and A. Jarzebowski. Experimental analysis of soil deformation below a rolling rigid cylinder. *J. Terramechanics*, 41:223–241, 2004.
- M. T. Manzari and Y. F. Dafalias. A critical state two-surface plasticity model for sands. *Geotechnique*, 47(2):255–272, 1997. ISSN 00168505.
- E. McKyes. Soil cutting and tillage. Elsevier, 1985.
- G. Meirion-Griffith. Advances in Vehicle-terrain interaction modeling for small, rigid-wheeled vehicles operating on deformable terrain. PhD thesis, Mechanical and Aerospace Engineering, Illinois Institute of Technology, 2012.
- L. Ojeda, D. Cruz, G. Reina, and J. Borenstein. Current-based slippage detection and odometry correction for mobile robots and planetary rovers. *IEEE Transactions on Robotics*, 22(2):366–378, April 2006.
- O. Onafeko and A. R. Reece. Soil stresses and deformations beneath rigid wheels. *J. Terramechanics*, 4(1):59–80, 1967.
- J.V. Perumpral, J.B. Liljedahl, and W.H. Perloff. A numerical method for predicting the stress distribution and soil deformation under a tractor wheel. *J. Terramechanics*, 8(1): 9–22, 1971.
- W. Petersen. *A Volumetric Contact Model for Planetary Rover Wheel/Soil Interaction*. PhD thesis, University of Waterloo, 2012.

- F. Pfeiffer. Deregularization of a smooth system example hydraulics. *Nonlinear Dynamics*, 47(1–3):219–233, 2007.
- F. Pfeiffer and Ch. Glocker. *Multibody Dynamics with Unilateral Contacts*. Wiley Series in Nonlinear Science. John Wiley & Sons Inc., 1996.
- L. E. Ray. Estimation of terrain forces and parameters for rigid-wheeled vehicles. *IEEE Transactions on Robotics*, 25(3):717–726, June 2009. ISSN 1552-3098. doi: 10.1109/TRO.2009.2018971.
- A. R. Reece. The fundamental equation of earth-moving mechanics. *Proceedings of the Institution of Mechanical Engineers*, 179:16–22, 1964.
- B. Schäfer, A. Gibbesch, R. Krenn, and B. Rebele. Planetary rover mobility simulation on soft and uneven terrain. *Vehicle System Dynamics: International Journal of Vehicle Mechanics and Mobility*, 48(1):149–169, 2010.
- I. C. Schmid. Interaction of vehicle and terrain results from 10 years research at ikk. *J. Terramechanics*, 32(1):3–26, 1995.
- H. Schwanghart. Lateral forces on steered tyres in loose soil. *J. Terramechanics*, 5(1): 9–29, 1968.
- C. Senatore and K. D. Iagnemma. Direct shear behaviour of dry, granular soils for low normal stress with application to lightweight robotic vehicle modelling. In *Proceedings of the 17th International Symposium of the International Society of Terrain-Vehicle Systems*, pages 1–11, Blacksburg, VA, USA, 18–22 November 2011.
- C. Senatore and C. Sandu. Off-road tire modeling and the multi-pass effect for vehicle dynamics simulation. *J. Terramechanics*, 48:265–276, 2011.
- C. Senatore, M. Wulfmeier, P. Jayakumar, J. Maclennan, and K. Iagnemma. Investigation of stress and failure in granular soils for lightweight robotic vehicle applications. In *Ground Vehicle Systems Engineering and Technology Symposium*, Michigan, August 14–16 2012.

- H. Shibly, K. Iagnemma, and S. Dubowsky. An equivalent soil mechanics formulation for rigid wheels in deformable terrain, with application to planetary exploration rovers. *J. Terramechanics*, 42:1–13, 2005.
- T. Shikanai, K. Hashiguchi, Y. Nohse, M. Ueno, and T. Okayasu. Precise measurement of soil deformation and fluctuation in drawbar pull for steel and rubber-coated rigid wheels. *J. Terramechanics*, 37:21–39, 2000.
- S. A. Shoop. Finite element modeling of tire–terrain interaction. Technical report, US Army Corps of Engineers, Engineer Research and Development Center, 2001.
- SIMULIA. *Abaqus Theory Manual, Version 6.10-EF*. Dassault Systèmes Simulia Corp., 2010.
- K. Skonieczny, S. J. Moreland, C. Creager, and D. Wettergreen. Novel experimental technique for visualizing and analyzing robot-soil interactions. In *Earth and Space Conference*, pages 1–10, April 2012.
- G. Sohl and A. Jain. Wheel-terrain contact modelling in the ROAMS planetary rover simulation. *Proceedings of IDETC*, pages 1–9, September 2005.
- D. E. Stewart. Rigid-body dynamics with friction and impact. *SIAM Review*, 42(1):3–39, 2000. doi: 10.1137/S0036144599360110.
- M. Taiebat and Y. F. Dafalias. Sanisand: Simple anisotropic sand plasticity model. *Int. J. Numer. Anal. Meth. Geomech.*, 32:915–948, 2008.
- B. Trease, R. Arvidson, R. Lindemann, K. Bennett, F. Zhou, K. Iagnemma, C. Senatore, and L. Van Dyke. Dynamic modeling and soil mechanics for path planning of the mars exploration rovers. In *ASME International Design Engineering Technical Conference & Computers and Information in Engineering Conference IDETC/CIE*, 2011.
- P. Visscher and E. Reid. Continued development of juno rover. In *50th AIAA Aerospace Sciences Meeting*, pages 1–13, Nashville, USA, January 2012.

- S. Wanjii, T. Hiroma, Y. Ota, and T. Kataoka. Prediction of wheel performance by analysis of normal and tengential stress distributions under the wheel-soil interface. *J. Terrame-chanics*, 34(3):165–186, 1997.
- J. Y. Wong. Behaviour of soils beneath rigid wheels. *J. Agric. Engng. Res.*, 12(4):257–269, 1967.
- J. Y. Wong. *Theory of Ground Vehicles*. John Wiley and Sons, New Jersey, fourth edition, 2008.
- J. Y. Wong. Terramechanics and Off-Road Vehicle Engineering: Terrain Behaviour, Off-Road Vehicle Performance and Design. Elsevier, second edition, 2010.
- J. Y. Wong and V. M. Asnani. Study of the correlation between the performances of lunar vehicle wheels predicted by the Nepean wheeled vehicle performance model and test data. *Proceedings of the Institution of Mechanical Engineers, Part D (Journal of Automobile Engineering)*, 222(D11):1939–54, 2008. ISSN 0954-4070.
- J. Y. Wong and A. R. Reece. Prediction of rigid wheel performance based on the analysis of soil-wheel stresses part I: Performance of driven rigid wheels. *J. Terramechanics*, 4 (1):81–98, 1967a.
- J. Y. Wong and A. R. Reece. Prediction of rigid wheel performance based on the analysis of soil-wheel stresses part II: Performance of towed rigid wheels. *J. Terramechanics*, 4 (2):7–25, 1967b.
- D. M. Wood. *Soil Behaviour and Critical State Soil Mechanics*. Cambridge University Press, first edition, 1990.
- K. Xia. Finite element modeling of tire/terrain interaction: Application to predicting soil compaction and tire mobility. *J. Terramechanics*, 48:113–123, 2011.
- R. N. Yong and E. A. Fattah. Prediction of wheel-soil interaction and performance using the finite element method. *J. Terramechanics*, 13(4):227–240, 1976.
- R. N. Yong, E. A. Fattah, and P. Boonsinsuk. Analysis and prediction of tyre-soil interaction and performance using finite elements. *J. Terramechanics*, 15(1):43–63, 1978.

K. Yoshida and G. Ishigami. Steering characteristics of a rigid wheel for exploration on loose soil. In *IEEE/RSJ Int. Conf. Intelligent Robots and Systems (IROS)*, pages 3995–4000, Sept. 2004.

APPENDIX A

Drucker-Prager Model with Cap Hardening

The Drucker-Prager with cap hardening plasticity model is used in this thesis to represent the plastic response of soil. In order to explain this model, some basic concepts regarding elasto-plasticity theory are briefly recalled.

A.1 Basic Elements of an Elasto-plastic Model

The concept of an elasto-plastic model can be explained with a simple test: uniaxial tension of ductile metals. The common mathematical model used to capture the behaviour of ductile metals in uniaxial tests can be illustrated in Fig. A.1, which is a 1D elasto-plastic constitutive model.

In this model, if the total strain in the material is such that the tensile stress σ remains below the yield stress σ_y , the deformation is purely elastic. The total elastic strain that corresponds to σ_y is ε_y . It is noted that for ductile metals, a linear relation has been experimentally observed between stress and strain in the elastic domain.

If the total strain exceeds ε_y , the material will show permanent or plastic deformation. According to this model, when loading to $\sigma_1 > \sigma_y$, as shown in Fig. A.1, and then fully unloading, a plastic strain ε_1^p will remain. Now, if loading is applied again, such that the total strain ε_2 is below ε_1 , the material will show only elastic deformation, i.e., by removing

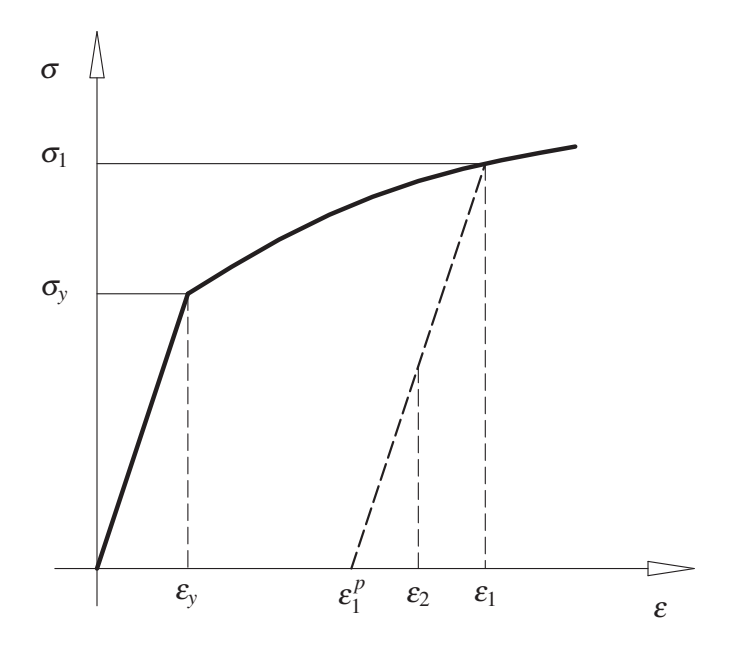


FIGURE A.1. Mathematical model for the uniaxial tension experiment (adapted with modification from (de Souza Neto et al., 2008))

the load, the strain will become ε_1^p . The stress in this case can be obtained from:

$$\sigma_2 = E(\varepsilon_2 - \varepsilon_1^p) \tag{A.1}$$

where a linear elastic model is used to relate the elastic strain to the stress, and E is the Young modulus of the material. In general, the total stress can be expressed based on the total elastic strain as:

$$\sigma = E\varepsilon^e \tag{A.2}$$

which means that the elastic strain is obtained from below in this model of the uniaxial experiment:

$$\varepsilon^e = \varepsilon - \varepsilon^p \tag{A.3}$$

That is, the additive decomposition of the strain tensor holds for this model.

Another observation from the uniaxial test and its mathematical model is that after the material has experienced plastic deformation, its yield stress increases. From Fig. A.1, when loading to σ_1 and start unloading, the new yield stress is $\sigma_{y1} = \sigma_1$, which is larger than the yield stress σ_y before plastic deformation. This evolution of the yield stress caused by the plastic strain is known as *hardening* (de Souza Neto et al., 2008).

According to de Souza Neto et al. (2008), a general elasto-plastic constitutive model contains the elements listed below:

- A rule for elasto-plastic strain decomposition and an elastic law
- A yield criterion, that is expressed with a yield surface
- A plastic flow rule and a hardening law.

Each of these elements is discussed below for the assumed elasto-plastic constitutive model (Drucker-Prager with cap hardening).

A.2 Elasto-plastic Strain Decomposition and the Elastic Law

In this thesis, the additive decomposition of the strain tensor is adopted, which is expressed in incremental form as ¹:

$$\Delta \boldsymbol{\varepsilon} = \Delta \boldsymbol{\varepsilon}^e + \Delta \boldsymbol{\varepsilon}^p \tag{A.4}$$

In addition, a linear elastic law is assumed for the elastic behaviour of soil. This law can be expressed as:

$$\mathbf{\sigma} = \mathbf{C} : \mathbf{\varepsilon}^e \tag{A.5}$$

where C is the fourth-rank elastic stiffness tensor and symbol ":" denotes double contraction, as needed between a fourth-rank tensor C and a second-rank tensor ε^e (de Souza Neto et al., 2008), to produce a second-rank stress tensor. In addition, it is noted that the stress tensor is obtained from the total elastic strain tensor.

¹It is noted that in finite deformation, the decomposition of elastic and plastic parts are multiplicative (Khan and Huang, 1995); however, as mentioned in (SIMULIA, 2010), the additive decomposition still holds when elastic strain is infinitesimal and the strain rate is measured as the rate of deformation.

A.3 Yield Criterion and Yield Surface

In elasto-plastic materials, the principle of yield and plastic flow can be expressed by means of a yield surface.

The yield surface, described by a scalar yield function F, is defined in terms of the stress invariants p and q, for the Drucker-Prager with cap hardening plasticity model. p is related to the first moment of the stress tensor

$$p = -\frac{1}{3} \operatorname{tr}(\boldsymbol{\sigma}), \tag{A.6}$$

while q, the von Mises equivalent stress, is proportional to the square root of the second moment of S:

$$q = \sqrt{\frac{3}{2} \text{tr}(\mathbf{S}^2)} \tag{A.7}$$

where S is the stress deviator, defined as:

$$\mathbf{S} = \mathbf{\sigma} + p\mathbf{I} \tag{A.8}$$

and I is the identity tensor.

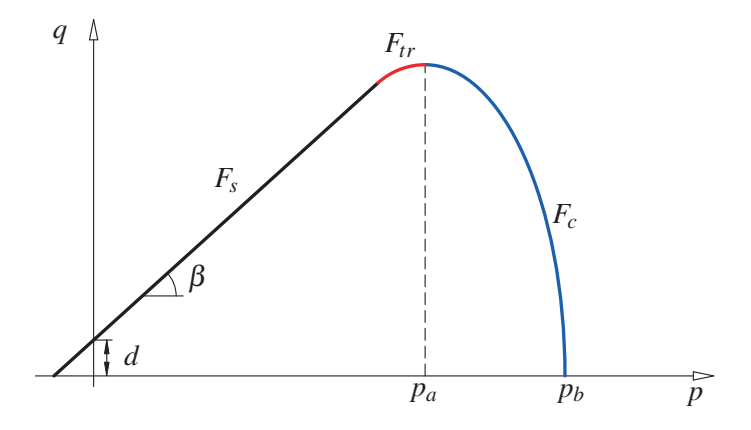


FIGURE A.2. Yield surface in the *p-q* plane (adapted from (SIMULIA, 2010))

The yield surface as depicted in Fig. A.2, consists of three parts in the p-q plane: the failure surface F_s ; the transition surface F_{tr} ; and the cap surface F_c . They obey the relations below (SIMULIA, 2010):

$$F_s = q - p \tan \beta - d = 0 \tag{A.9}$$

$$F_c = \sqrt{(p - p_a)^2 + \left(\frac{R_e q}{1 + \alpha - \alpha/\cos\beta}\right)^2} - R_e (d + p_a \tan\beta) = 0$$
 (A.10)

$$F_{tr} = \sqrt{(p - p_a)^2 + \left[q - \left(1 - \frac{\alpha}{\cos \beta}\right)(d + p_a \tan \beta)\right]^2} - \alpha(d + p_a \tan \beta) = 0 \quad (A.11)$$

where β and d are related to the angle of friction and cohesion of the material, respectively. As mentioned in (SIMULIA, 2010), R_e is a material parameter referred to as the cap eccentricity, while α , typically between 0.01 and 0.05, is used to define the size of F_{tr} . p_a is obtained from the evolution variable p_b as (SIMULIA, 2010):

$$p_a = \frac{p_b - R_e d}{1 + R_e \tan \beta} \tag{A.12}$$

As will be explained in Section A.4, p_b defines the hardening or softening behaviour.

Based on Eqs.(A.9)–(A.12), the yield function can be expressed as $F(\boldsymbol{\sigma}, p_b)$ for the above-mentioned Drucker-Prager model. According to elasto-plasticity theory, (Khan and Huang, 1995; de Souza Neto et al., 2008), when $F(\boldsymbol{\sigma}, p_b) < 0$, the material is in an elastic state. Therefore, the entire elastic domain can be expressed by the following set (de Souza Neto et al., 2008):

$$\mathscr{E} = \{ \boldsymbol{\sigma} \mid F(\boldsymbol{\sigma}, p_b) < 0 \} \tag{A.13}$$

It is noted that in the elastic domain, plastic yielding is not possible. Furthermore, when the yield function is zero, i.e., $F(\boldsymbol{\sigma}, p_b) = 0$, plastic yielding and plastic flow can

occur. The set of stresses at every given p_b that satisfy the plastic yielding condition form a surface, which is referred to as the *yield surface* and is defined as:

$$\mathscr{Y} = \{ \boldsymbol{\sigma} \mid F(\boldsymbol{\sigma}, p_b) = 0 \} \tag{A.14}$$

This yield surface forms the boundary of the elastic domain. It should also be mentioned that any state of stress that leads to a positive yield function is not plastically admissible (Khan and Huang, 1995; de Souza Neto et al., 2008).

A.4 Plastic Flow Rule and the Hardening Law

In order to have a complete plasticity model, we need to define the plastic flow rule and a law for the evolution of hardening-related variables. In this regard, it is convenient to define the flow rule in terms of a scalar *flow potential* function (de Souza Neto et al., 2008). In the Drucker-Prager with cap hardening model, the flow potential G is a scalar that consists of two parts in the p-q plane; plastic flow on the cap region G_c , and plastic flow on the failure and transition regions G_s (SIMULIA, 2010):

$$G_c = \sqrt{(p - p_a)^2 + \left(\frac{R_e q}{1 + \alpha - \alpha/\cos\beta}\right)^2}$$
(A.15)

$$G_s = \sqrt{[(p_a - p)\tan\beta]^2 + \left(\frac{q}{1 + \alpha - \alpha/\cos\beta}\right)^2}$$
 (A.16)

The two elliptical portions, G_c and G_s , form a C^1 -continuous potential surface. It should be mentioned that in this elasto-plastic model, plastic flow on the cap region G_c causes hardening, while the plastic flow on G_s leads to softening.

As mentioned earlier for the uniaxial test, the yield surface evolves with the plastic strain. In the Drucker-Prager elasto-plstic model with cap hardening, the hydrostatic compression yield stress p_b , shown in Fig. A.2, varies with the volumetric plastic strain $\varepsilon_{\text{vol}}^p$ according to a piecewise linear function, as schematically shown in Fig. A.3. As shown in Fig. A.4, upon increasing p_b , the yield surface expands, which causes material hardening. Furthermore, decreasing p_b causes the yield surface to become smaller, which is known as softening.

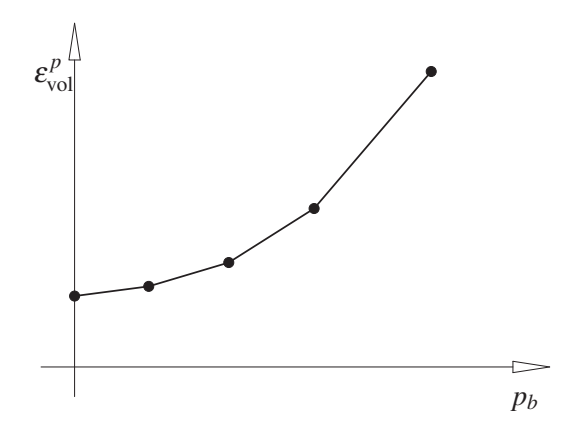


FIGURE A.3. A typical hardening relation between $\varepsilon_{\text{vol}}^p$ and p_b (adopted with modification from (SIMULIA, 2010))

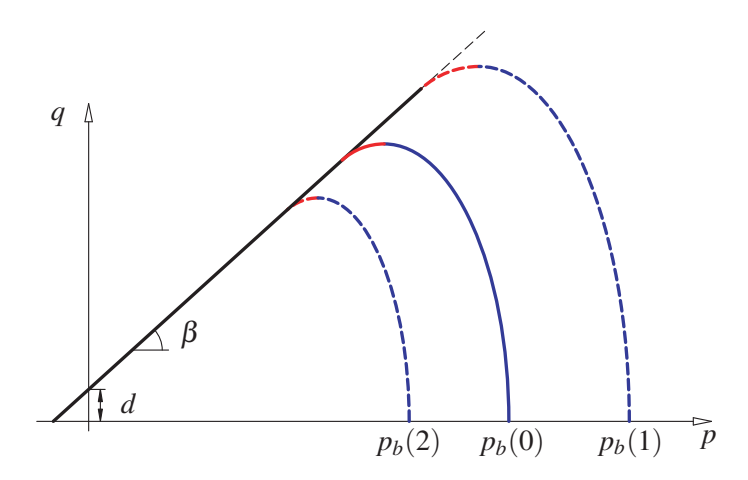


FIGURE A.4. Evolution of the yield surface in the p-q plane with changes in p_b . Increasing p_b results in expansion in the yield surface, and hence, hardening, while reduction in p_b leads to a smaller yield surface and soil softening.

APPENDIX B

Computation of the Elastic and Plastic Parts of the Strain-increment Tensor

The calculation of $\Delta \boldsymbol{\varepsilon}^e$ and $\Delta \boldsymbol{\varepsilon}^p$ is explained briefly here, based on the total strain increment $\Delta \boldsymbol{\varepsilon}$.

Following an approach explained by de Souza Neto et al. (2008), the elastic and plastic parts of the strain increment tensor can be decomposed by finding a single scalar, known as *plastic multiplier*, from a nonlinear algebraic equation. This procedure is summarized below.

Using plastic potential theory, a classical plasticity theory (Khan and Huang, 1995), the increment in the plastic strain can be obtained as

$$\Delta \boldsymbol{\varepsilon}^p = \lambda_1 \frac{\partial G}{\partial \boldsymbol{\sigma}} \tag{B.1}$$

where λ_1 is the plastic multiplier and G is the flow potential surface defined in Eqs. (A.15) and (A.16) for the Drucker-Prager constitutive relation.

In the algorithm described below, it is required to find the evolution of p_b , the hardening variable in the Drucker-Prager constitutive relation, based on λ_1 . As explained in Section A.2, p_b depends only on the volumetric plastic strain $\varepsilon_{\text{vol}}^p$. Therefore, the relation below for the evolution of p_b is derived using Eq. (B.1):

$$\Delta p_b = \lambda_1 \frac{\partial p_b}{\partial \varepsilon_{\text{vol}}^p} \text{tr} \left(\frac{\partial G}{\partial \boldsymbol{\sigma}} \right)$$
 (B.2)

In obtaining Eq. (B.2), the relation for the volumetric plastic strain, namely,

$$\varepsilon_{\text{vol}}^p = \text{tr}(\boldsymbol{\varepsilon}^p) \tag{B.3}$$

is used.

For determining λ_1 , what is called the *loading/unloading conditions* of the elastoplastic model must be satisfied (de Souza Neto et al., 2008). These conditions can be expressed in terms of the Karush-Kuhn-Tucker criteria stated by Jeremić et al. (2010):

$$F(\boldsymbol{\sigma}, p_b) \le 0; \quad \lambda_1 \ge 0; \quad F \cdot \lambda_1 = 0$$
 (B.4)

where F is the yield surface that is defined for the Drucker-Prager constitutive relation in Eqs. (A.9–A.11). Based on these criteria, a positive λ_1 exists when there is a plastic deformation; λ_1 is zero if the deformation is only elastic. Using the condition stated in Eq. (B.4), an elastic predictor/plastic corrector algorithm is normally used to compute λ_1 . With λ_1 known, the plastic strain increment is readily determined from Eq. (B.1). In addition, from Eq. (A.4), the elastic strain increment tensor $\Delta \boldsymbol{\varepsilon}^e$ is obtained. From this $\Delta \boldsymbol{\varepsilon}^e$, the increment in the stress tensor caused by $\Delta \boldsymbol{\varepsilon}$ is readily determined. This algorithm involves the steps below, following the procedure explained in Box 7.1 of (de Souza Neto et al., 2008):

ALGORITHM 4.

Given the current stress tensor $\sigma(0)$, strain tensors $\boldsymbol{\varepsilon}^{e}(0)$ and $\boldsymbol{\varepsilon}^{p}(0)$, and the total strain increment $\Delta \boldsymbol{\varepsilon}$, find λ_{1} .

(a) Elastic predictor step (adapted from (de Souza Neto et al., 2008)):

(i) Set $\lambda_1 = 0$, i.e., assume that the strain increment is fully elastic. Then calculate the elastic trial states as:

$$\boldsymbol{\varepsilon}_{trial}^{e} = \boldsymbol{\varepsilon}^{e}(0) + \Delta \boldsymbol{\varepsilon} \tag{B.5a}$$

$$p_b^{trial} = p_b(0) \tag{B.5b}$$

$$\boldsymbol{\sigma}^{trial} = \mathbf{C} : \boldsymbol{\varepsilon}_{trial}^{e} \tag{B.5c}$$

It should be noted that p_b changes with ε_{vol}^p . Therefore, if $\varepsilon^p(0)$ is known, so is $p_b(0)$.

- (ii) Verify the plastic admissibility condition: $F(\boldsymbol{\sigma}^{trial}, p_b^{trial}) \leq 0$. If the test fails, we go to step (b); otherwise, λ_1 is reported as zero, i.e., only elastic deformation occurs.
- (b) Plastic corrector step or Return-Mapping Algorithm, in which the system of equations below is solved for $\boldsymbol{\varepsilon}^e$, p_b , and λ_1 (adapted from (de Souza Neto et al., 2008)):

$$\boldsymbol{\varepsilon}^{e} - \boldsymbol{\varepsilon}_{trial}^{e} + \lambda_{1} \frac{\partial G}{\partial \boldsymbol{\sigma}} = \mathbf{0}$$
 (B.6a)

$$p_b - p_b^{trial} - \lambda_1 \frac{\partial p_b}{\partial \varepsilon_{vol}^p} \operatorname{tr} \left(\frac{\partial G}{\partial \boldsymbol{\sigma}} \right) = 0$$
 (B.6b)

$$F(\boldsymbol{\sigma}, p_b) = 0 \tag{B.6c}$$

with $\boldsymbol{\sigma} = \mathbf{C} : \boldsymbol{\varepsilon}^e$.

It is noted that Eq. (B.6a) is derived from the additive decomposition of the strain increment tensor. In addition, Eq. (B.6b) is obtained from Eq. (B.2), which is the evolution of the hardening parameter. Moreover, Eq. (B.6c) stems from the plastic admissibility condition, according to which, when plastic deformation exists, the yield function is zero.

Details on the numerical solution of Eqs. (B.6a)–(B.6c) can be found in (Jeremić et al., 2010).